High-strength fully porous biomaterials for bone replacement and their application to a total hip replacement

Burnett Johnston

Department of Mechanical Engineering

McGill University

Montréal Canada

April 2016

A thesis submitted to McGill University in partial fulfillment of the requirements for the degree of Master of Engineering.

Abstract

High-strength fully porous biomaterials built with additive manufacturing provide an exciting opportunity for load-bearing orthopedic applications. The first portion of this work presents two high-strength stretch-dominated topologies, the Tetrahedron and the Octet truss, as well as an intuitive visualization method to understand the relationship of cell topology, pore size, porosity while constrained by bone ingrowth requirements, and additive manufacturing limitations. 40 samples of selected porosities are fabricated using Selective Laser Melting (SLM), and their morphological deviations resulting from SLM are assessed via micro-CT. Mechanical compression testing is used to obtain stiffness and strength properties. The results show that the mechanical strength is almost 5 times stronger than that of tantalum foam, an existing fully porous biomaterial used in orthopedics.

In the second portion of this work, the developed fully porous biomaterial is applied to a total hip replacement to reduce bone loss secondary to stress shielding. Current stems used in total hip arthroplasty are made from fully solid materials and are much stiffer than the natural bone. The drastic difference in stiffness leads to reduced stress on the surrounding bone which manifests as a reduction in bone quality surrounding the implant. The reduction in bone stock can lead to serious complications such as periprosthetic fracture, and increased risk during a revision surgery. A hip replacement implant made with a fully porous tuned microarchitecture allows for a reduction in stress shielding while respecting bone ingrowth and manufacturing limitations. An in-vitro experiment is conducted on six composite femurs that are divided and implanted with either an optimal porous implants or a fully solid control stem, both with equivalent implant macro geometry. Both the intact and implanted femurs are loaded in a quasi-physiological loading state. The surface strain on the medial calcar is recorded using Digital Image Correlation (DIC). The change of strain between intact and implanted femur is used as a proxy for stress shielding. Femurs implanted with a fully porous stem showed a significant reduction of 60% of the medial calcar in Gruen zone 6 susceptible to resorption. This serves as the first experimental demonstration that a tuned fully porous hip replacement has the possibility to reduce stress shielding and the associated clinical complications.

Abrégé

Les biomatériaux entièrement poreux à haute résistance construits avec la fabrication additive fournissent une excellente occasion pour des applications orthopédiques structurales. La première partie de cet ouvrage présente deux topologies à haute résistance étirement dominé, le tétraèdre et le *Octet truss*, ainsi qu'une méthode de visualisation intuitive afin de comprendre la relation de la topologie de la cellule, la taille des pores et la porosité, tout en limitant les exigences de croissance osseuse et les limitations de fabrication d'additifs. Quarente échantillons de porosités sélectionnés sont fabriqués en utilisant la fusion sélective par laser (SLM), et leurs écarts morphologiques résultant du procédé SLM sont évalués par microtomographie. L'essai de compression mécanique est utilisé pour obtenir des propriétés de raideur et de résistance. Les résultats démontrent que la résistance mécanique est presque cinq fois plus forte que celle de la mousse de tantale, un biomatériau entièrement poreux actuellement utilisé en orthopédie.

Dans la deuxième partie de ce travail, le biomatériau entièrement poreux développé est appliqué à un remplacement de la hanche afin de réduire la perte osseuse secondaire du au « stress shielding ». Les tiges actuellement utilisé dans l'arthroplastie totale de la hanche sont fabriquées à partir de matériaux entièrement solides et sont beaucoup plus raideur que l'os naturel. La différence radicale de la raideur mène à une réduction du stress sur l'os entourant qui se manifeste par une réduction de la qualité de l'os entourant l'implant appelé « stress shielding ». La réduction de la masse osseuse peut entraîner des complications graves comme une fracture périprosthétique, et augmente considérablement le risque d'une chirurgie de révision. Lorsque c'est appliqué à un implant de arthroplastie de la hanche, le les biomatériaux entièrement poreux à haute résistance avec microarchitecture réglée permettent une réduction du « stress shielding » en respectant les exigences de croissance osseuse et de fabrication. Afin d'évaluer les réclamations de réduction du « stress shielding », une expérience est menée sur six fémurs composites qui sont divisés et implantés avec soit un implant poreux optimal ou une tige entièrement solide comme contrôle, avec la géométrie macro implant équivalent. Les deux fémurs intactes et implantés sont chargés dans un état quasi-physiologique. La déformation de surface sur la calcar médial est enregistrée en utilisant la corrélation d'images numériques. Le changement de déformation entre le fémur intact et implanté est utilisé comme proxy pour le « stress shielding ». Les fémurs implantés avec une tige entièrement poreux ont montré une réduction significative de 60% dans la zone Gruen 6. Cela sert comme la première démonstration expérimentale que le remplacement totalement poreuse réglé de la hanche totalement poreuse a la possibilité de réduire le « stress shielding » et les complications cliniques associées.

Acknowledgements

I would like to sincerely thank my supervisor Professor Damiano Pasini. Your continued guidance, mentorship, and support have been invaluable. It has been an absolute privilege to work under your guidance. I cannot thank you enough for allowing me to have the opportunity to be part of your team. The experiences that I have gained both professionally and personally will stay with me not only for the rest of my career, but the rest of my life.

I would like to recognize and thank Dr. Sajad Arabnejad and Dr. Baljinder Singh for all of their support and mentorship. I cannot express how lucky I am to have met them both. They are not only phenomenal teachers, leaders, and scientists, but also all I could ever ask for in a friend. Your support never wavered, and I am truly grateful.

I particularly wish to thank Dr. Michael Tanzer for his visionary clinical input. Dr. Tanzer not only lent his expertise for distilling the, at times overwhelming, clinical fund of knowledge pertaining to implant performance, but also for the literal blood, sweat, and mouthfuls of dust required to implant the composite femurs for the in-vitro investigation.

The following work would not be possible if not for the contributions of Renishaw LLC in lending their considerable manufacturing expertise in a collaborative manner. In particular I thank Mark Kirby for his dedication in working to improve the manufacturability of the lattice samples that are at the boundary of manufacturing limits using SLM, while always available to teach me more about additive manufacturing using SLM.

I also thank my family, friends, and colleagues for your unwavering support. You make every day an exciting new adventure to live, learn, and love. I dedicate this thesis to my parents: I owe everything to you.

Contributions

Dr. Baljinder Singh developed the script for generating the design charts as well as the original parametric models that were subsequently modified for the lattice samples in chapter 3. Dr. Michael Tanzer and Jenny Ann Pura performed the in-vivo evaluation of bone ingrowth into tetrahedron and octet truss transcortical implants in a canine animal model that provided the biological context for the discussion of mechano-biologic performance in section 3.8 relative to Tantalum foam. Dr. Sajad Arabnejad performed the optimization that determined the optimum material distribution for the fully porous implant analyzed in chapter 4, as well as working collaboratively with the author to create the detailed tetrahedral architecture. The micro CT of the fully porous implant was acquired at the Conseil national de recherches du Canada by Stephanie Grenier. The femurs where surgically prepared and implanted by Dr. Michael Tanzer due to his considerable operative experience which include an adult hip reconstructive fellowship. All samples where manufactured by Renishaw LLC under the direction of Mark Kirby. All of the other work that is not exclusively mentioned above and presented herein is that of the author.

Table of Contents

List of Tables

List of Figures

Chapter 1: Introduction

Our bones provide the most basic form of support within our lives. Unfortunately, as we age, our bones become susceptible to trauma and age related changes such as osteoarthritis. These changes can lead to crippling pain and immobility, or severe fractures that immediately and painfully interrupt usual routines. The summation of these traumas, minor and major, natural or imposed, can compromise our wellbeing. Fortunately, for many of these severe pathologies that compromise function, surgical intervention can be employed to stabilize or improve our body's mobility and its ability to support itself.

An essential tool in the arsenal of an orthopedic surgeon, and pivotal to a patient's care, are bone interfacing implants. These devices can either provide temporary support while the body heals itself, or completely replace a given function within the musculoskeletal system and allow a return to support and motion. Despite the drastic improvements that these devices can provide, there is a growing need to improve the performance of the implants. Factors such as increasing life expectancy, the younger age at which patients receive implants, and ballooning health care costs, mandate a need for longer component service life. The increased activity levels of patients, even as they age, require more robust technologies that can withstand the wear and tear imposed by daily activities. Furthermore, basic issues such as mechanical incompatibility between stiff metals and compliant bones needs to be addressed to achieve improved performance.

This work examines the use of a microarchitectured biomaterial for bone interfacing orthopedic applications to provide next generation performance to these devices. This work provides the framework for developing mechanically compatible devices that can be seamlessly tuned to the natural bone to increase the service life, improve recovery time, and reduce the risk of revision surgeries.

1.1 Thesis Structure

The first chapter of the thesis serves to introduce the scope of the work and to provide an overview of the organizational structure.

The second chapter provides a background, encapsulating the function of the musculoskeletal system, which is critical to understand, before a discussion of possible intervention routes can be undertaken. Bone interfacing implants are introduced, along with their general specifications and what is required for bone ingrowth. Due to the use of porous cellular materials for bone ingrowth, a brief overview of the concepts behind cellular materials is explored. Based on this improved understanding of cellular materials, porous cellular materials for bone ingrowth are discussed, with particular attention paid to tantalum foam along with its strengths and limitations. A popular subset of bone interfacing implants, joint arthroplasties (also known as replacements), are introduced, with an explanation of their fixation methods using porous materials along with an important drawback of current implants: stress shielding and the bone resorption secondary to stress shielding. Finally, a description of microarchitecture materials produced with additive manufacturing is introduced to provide an outlook for the next generation of porous materials for bone replacement.

The third chapter of the thesis examines fully porous materials from a material perspective, and directly contrasts the microarchitectured material to tantalum foam. A strategy for understanding the complex relationships between morphology, mechanical properties, biological performance, and manufacturing limitations for fully porous biomaterials is provided, a critical step to apply them in a realistic clinical setting. This process is achieved through selection of a unit cell and the development of a geometric domain for the unit cell that visualizes the morphological parameters of the unit cell for a given pore topology. The manufacturing limitations and bone ingrowth can be superimposed to create a defined design domain that satisfies the bone ingrowth requirements and manufacturing limitations. This novel visualization method can be used to understand the interplay between the relevant parameters that impact the mechano-biological performance of porous biomaterials for orthopedics. The manufacturability and mechanical properties of the porous material are assessed experimentally for selected points within the domain. The implications of the experimental results are discussed. In particular elaborating how variable mechanical properties can be obtained, based on a detailed selection of the unit cell, and the strength and stiffness of selected cell topologies can be compared in a glance in one chart. The morphological results show how manufacturing deviation influences resulting morphology, and possible methods to decrease the discrepancy between as designed and manufactured porous biomaterials. The developed design charts also provide the framework for a generalized methodology that uses response surfaces to superimpose mechanical and biological performance onto the morphological (geometry) predictions in order to develop a robust understanding of the performance of porous biomaterials.

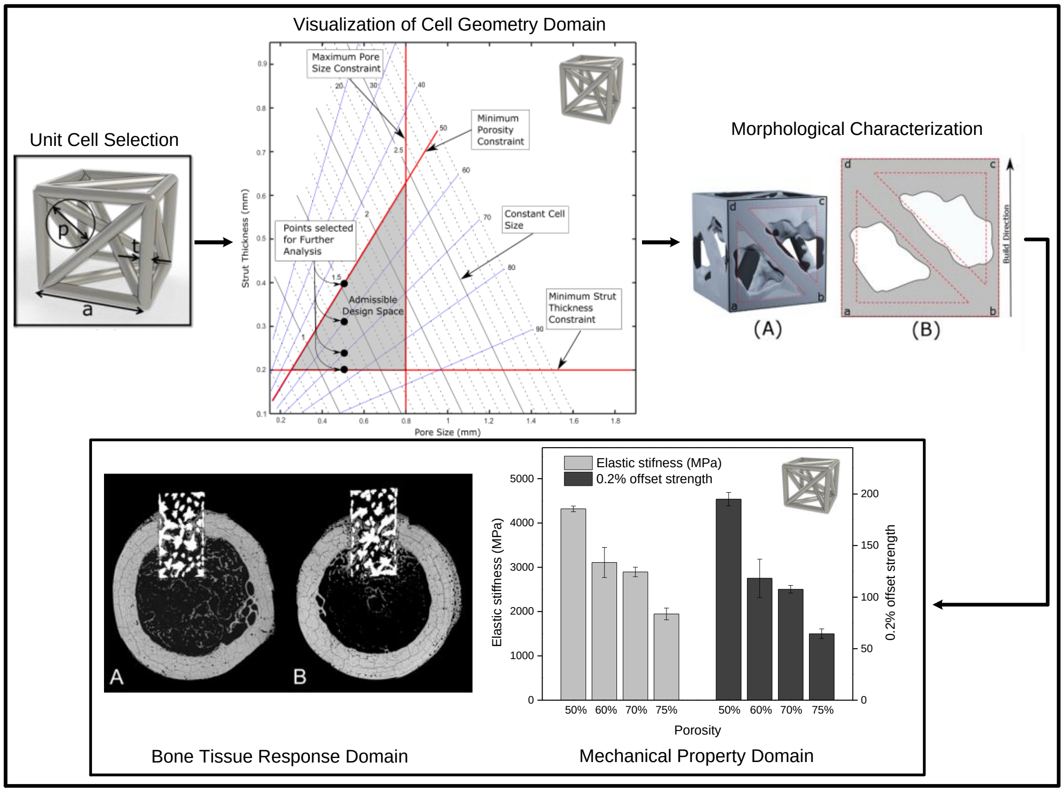

Figure 1: The interplay between cell morphology, mechanical properties, bone ingrowth, and manufacturing constraints.

The fourth chapter explores the functional application of fully porous biomaterials. It examines how fully porous biomaterials can be tuned for a specific application. In this case, the tetrahedron topology is used to develop a graded total hip replacement to minimize stress shielding, while concurrently respecting bone ingrowth limitations at the bone implant interface, and the manufacturing limitations of SLM. The performance is experimentally observed through means of a biomechanical model and compared to that of a solid hip replacement stem available in the market so as to highlight the potential of the porous material.

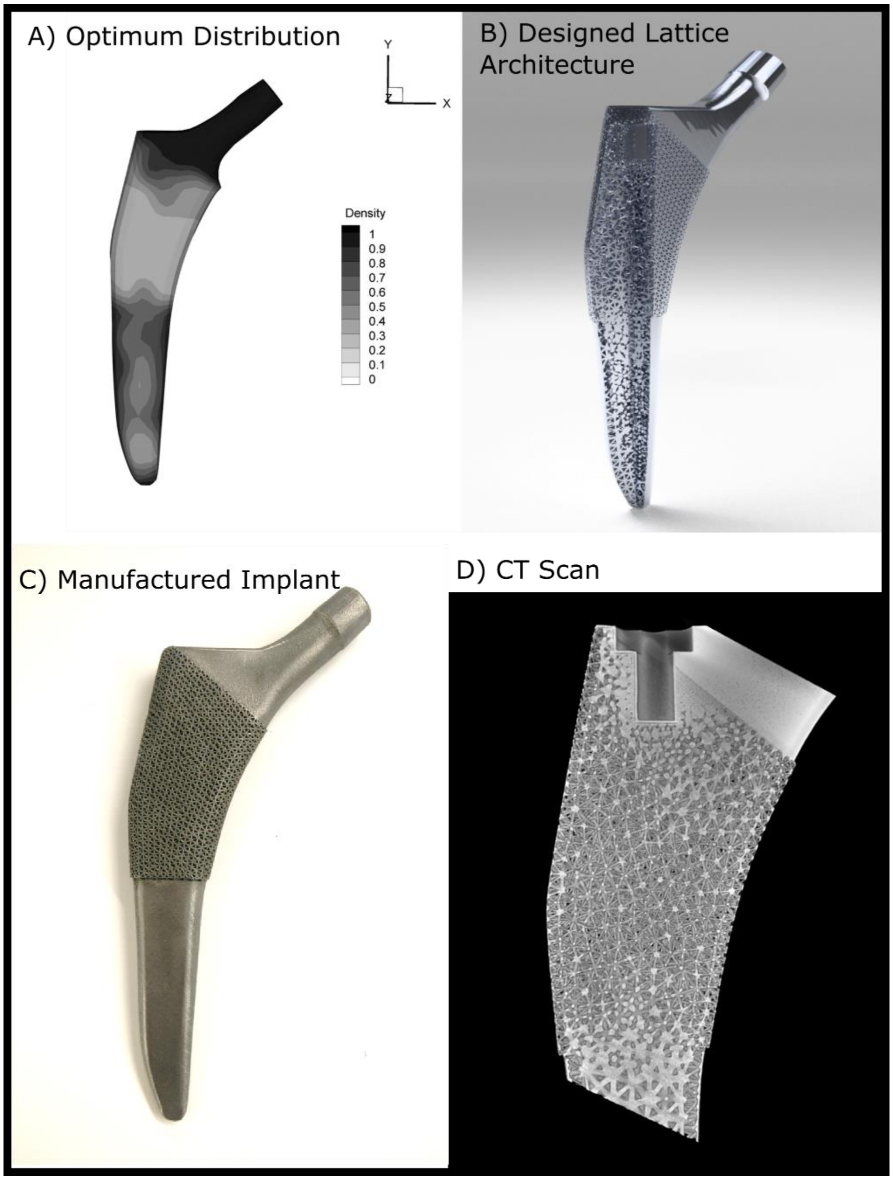

Figure 2: Application of a high strength fully porous biomaterial to a total hip replacement. A) Optimum density distribution. B) Implant with tessellated tetrahedron microarchitecture. C) Implant manufactured with SLM. D) Micro CT of manufactured implant.

The fifth chapter provides a conclusion with indications of future extensions of this work, from the twin vantages of material perspective, and clinically viable solutions to improve patients' lives.

Chapter 2: Background

This chapter provides an overview of bone interfacing implants. It provides a basic foundation for understanding the factors that govern their performance. Subsequent chapters provided a more targeted literature review with a scope focused on the relevance to the section: porous materials made with additive manufacturing in chapter three, and total hip replacements and stress shielding in chapter four.

2.1 Bone Interfacing Implants

Bone interfacing implants are engineered systems that are designed and surgically implanted directly apposing bone tissue, to restore a specific function to the human musculoskeletal skeletal (MSK) system. The human MSK system is primarily responsible for structural support, stability, and movement of the body. Additionally, it is responsible for a number of other critical functions, such as calcium and phosphorous storage, hematopoiesis, and protecting vital organs. The system is comprised of bones, muscle and connective tissue, and cartilage. From a biomechanical perspective the bones that comprise the skeletal system provide structural support and framework, muscles and connective tissue provide force actuation for both static stability and dynamic movement, and cartilage enables smooth low friction translation at joints. The MSK system involves the entire human body, and although the core functions outlined above are shared throughout the system, the specific function and anatomical form varies drastically between different segments of the system.

Since the MSK system is so broad, damage can have a profound effect not only on the affected individual, but as also on society at large, due to the severe debilitation that results[1]. Among the broad spectrum of MSK injuries and disorders is a subset of damage to both the skeletal system and the cartilage, which enables smooth movement between adjacent bones within the more general MSK system. This damage can be the result of abnormal development, disease or trauma. This damage includes traumatic fracture of bones which leads to structural incompetency , along with pathological degradation of cartilage, such as osteoarthritis that can lead to limited mobility and extreme pain [2]. If conservative treatment fails, bone interfacing implants can be surgically inserted to either stabilize the injured bone to allow for healing of the injured bone, or completely replace the damaged tissue and restore function. Bone interfacing implants include, but are not limited to: fracture fixation plates that provide support and immobilization for fractured bones while healing takes place, hemi or total joint arthroplasties that can effectively recover movement of joints, and bone augments, among many others, all with applications spanning the entire human body.

A major use of bone interfacing implants is for joint replacement, also known as arthroplasty. A joint replacement involves replacing the natural joint with a mechanical analog that restores joint motion, and relieves pain. It is frequently used when conservative management of osteoarthritis is no longer possible, or due to other factors such as trauma [3]. Joint replacements can either be partial (hemi) or total replacements. In a partial joint replacement, only one side of the articulation is replaced with a mechanical analog. Within the domain of arthroplasty procedures, total hip and total knee replacements (THR, and TKR, respectively) comprise over 93,000 operations per year in Canada, and 600,000 operations in the United States, with the number of operations projected to rise dramatically with the increasing lifespan of patients and the younger age for primary arthroplasties [4, 5]. In total hip replacements, the acetabulum is reamed and replaced with a socket component, while the femoral head is resected, and a stem is inserted into the femoral canal. On the stem, a femoral head is impacted, and it serves to re-create the ball and socket articulation of the joint.

Hip replacements, along with other joint replacements, can be generally divided into cemented and cementless implants. Cemented implants are fixed to the surrounding bone through means of a cement mantle. The cement, made from poly methyl methacrylate polymer (PMMA), is polymerized intraoperatively, and hardens around the implant, rigidly fixing it to the host bone. This method provides nearly instantaneous fixation between the implant and the host bone. Cementless biologic fixation relies on natural bone ingrowth to provide stability of the joint construct. Instead of a cement layer that bonds the implant and bone, the implant is directly in contact with the bone, and the implant has a porous coating that allows for bone ingrowth to provide rigid and long-term fixation. A press fit and high coefficient of friction provides primary stability immediately postoperatively while secondary bone ingrowth provides long term biologic fixation. Cementless fixation is generally preferred for patients who have higher functional demands and younger patients, since it is thought to improve long term outcomes [6, 7].

Because of the diverse functional purpose of the various components of the MSK system, the scope of applicability for bone interfacing implants is expansive. As such, the specific requirements for a bone interfacing implant vary based on its targeted application. Yet, there are certain requirements that all bone interfacing implants should possess. The primary requirement is that a bone interfacing implant should not be toxic to the surrounding tissue. Additionally, the implanted structure should possess sufficient structural strength, and allow for both primary fixation post-implantation along with long term fixation for continued success.

Non-toxicity to surrounding tissue falls within the scope of material biocompatibility. Biocompatibility is a term that captures the behavior of a biomaterial within a given application context, and is dependent upon the context and function of the implanted system, not only the material being used. For bone-interfacing implants, this means that there are no unintended deleterious effects to the surrounding tissue from the implanted system. Adverse reactions can results in inflammation, fibrosis, coagulation, infection, and require a revision of the implant [8]. Another concern is how fragmented portions of the material used interact with the body. For example, although Ultrahigh Molecular Weight Polyethylene (UHWMPE) shows little to no adverse tissue effect when in bulk form, it has been shown that small particulates formed from wear lead to a macrophage mediated response that can result in severe osteolysis [9]. Similar concerns exist for systemic metal toxicity that result from metal particulates released in the volumetric wear of Metal on Metal (MOM) bearing surfaces[10].

All bone interfacing implants will support some degree of loading due to the nature of the MSK system, although some components are subjected to higher loading. Arthroplasty implants are subjected to particularly high loads within the MSK system due to the eccentric muscle actuations. In the case of a hip replacement implant, the peak forces during movement can range from 2.8 to 11 times those of the bodyweight depending on the activity [11-13]. These loads, higher than body weight, are not only a feature of joints involved in ambulatory motion, but also others such as shoulder and elbow joints. This is a result of the muscle contractions that are required to maintain both static and dynamic stability [14, 15]. Furthermore, especially for replacements within joints used for locomotion, the implants are subjected to repetitive loading during gait. The estimated average loading for a moderately active patient can account for over 1 million loading cycles a year, and can be higher for younger, active patients [16, 17]. As such, the structural integrity of bone interfacing components, especially under repetitive fatigue loading, remains an important concern [18].

Fixation denotes how the implant is bonded to the host bone. Whereas cemented fixation occurs within minutes of polymerization, cementless fixation relies on bone ingrowth to provide long term implant stability.

A requisite for bone ingrowth is primary stability, which is achieved through press fit, friction at the bone implant interface, along with mechanical stability of the implant. The primary stability must be sufficient to limit micromotion below 30 microns [19, 20]. Interface micromotion greater than the 150 microns leads to the formation of fibrous tissue between the implant surface and the host bone, which can lead to severe thigh pain. If the conditions for primary stability are satisfied, bone ingrowth will occur directly via the contact of the implant structure with the porous network, thereby leading to a strong biological bond, often termed as secondary stability or biological fixation. The rate of bone ingrowth is dependent upon a multitude of factors, including pore size and porosity, as discussed in the subsequent sections.

2.1.1 Factors Affecting Bone Ingrowth

Bone ingrowth in cementless implants is required to achieve successful biological fixation. Bone ingrowth into an implanted structure is a highly complex phenomenon that involves a multitude of factors encompassing a cascade of cellular and extracellular biological events [21]. These factors include endogenous patient related factors, exogenous implant factors and interaction of the bone host-implant system [22].

Within the scope of this thesis, the work will focus on the exogenous implant factors, meaning that they are dependent only on the biomaterial and the implant. These exogenous factors include: pore topology, porosity, pore size, pore interconnectivity, pore permeability, diffusivity, surface finish (micro and nano-roughness), and the monolithic material [23-26]. The overall success of an implant and bone regeneration depends upon the careful selection of these factors. However, given the complex nature of bone ingrowth, the relationship between the factors is not straightforward, and there exist significant debate within the literature [26, 27]. This is compounded by the relation between many of the factors which makes systematic and reliable comparisons difficult. A consensus in the literature is that porosity between 50-80 percent and pore sizes ranging from 50-800 microns are desirable for good bone ingrowth, although what is required for optimal bone ingrowth is not currently fully understood [28, 29].

Additional factors that contribute to the complexity of bone ingrowth include the interaction of the host-implant system. These include mechanical stability and loading conditions. These are influenced by the macroscopic design of the implant, its stiffness and interface stress, the interface friction and the bone implant gap size [30-32]. These factors are very specific to the targeted application within the MSK system, and considering them in depth is beyond the scope of the current work.

2.2 Cellular Materials

This section provides a brief overview of cellular materials and their core concepts in order to better understand the development of high strength fully porous biomaterials for orthopedics. Cellular materials are classified as a combination of two phases of a material to form a network of connected cells, with the most common being a dispersion of gas through a solid phase. This allows for unique material properties, such as high strength and stiffness normalized by weight, which opened the door to a class of ultralight materials, including the world's lightest material [33]. Due to their mechanical efficiency, they are frequently seen in nature. Common examples of cellular materials in nature include wood, honey bee honeycombs, and the trabecular (spongy) bone, found below the compact cortical surfaces of bones. An important component of cellular materials is the degree of solid material relative to the total enclosed volume, termed relative density, and its complement porosity. Classical definitions from a mechanical perspective term a material with relative density below 30% (porosity above 70%) a cellular material, and those with density above 30% (Porosity below 70%) a porous material [34]. However, it is important to note that in orthopedic applications the term porous materials is used for all ranges of density and porosity, and within the scope of this thesis no differentiation will be made between the two.

Cellular materials can be either open or closed cell. Open celled foams have a high degree of interconnected pores that allow for movement of the mobile phase throughout the porous structure, whereas for materials with closed cells the mobile phase remains trapped in the individual cell. This leads to a concept known as interconnected porosity, which can be quantified as the percentage of the porous volume that can be reached from the bounding surface, and can range from fully closed (0% interconnected) , to fully porous (100% interconnected). Since pores must be accessible for bone ingrowth, as well as for the hypothesized possibility of improved cell signaling throughout the porous network, the degree of open porosity is most commonly used in any work pertaining porous materials for bone interfacing applications [35].

At the base of a cellular material is the unit cell, which is the basic building block that can tessellate a domain. Each edge of one unit cell forms the edge of an adjacent cell. The connectivity of struts, edges and faces, and the way the struts are arranged determines the unit cell topology, and greatly influences the behavior of the material.

A critical paradigm in cellular materials is the separation of length scale between the cell size and the structure size. This separation enables the understanding of cellular materials as a material as opposed to a structure. This separation in length scale between the unit cell scale, and the characteristic macroscopic geometry of the final part should be large, at least 10 times that of the unit cell [36, 37]. This is especially critical for modelling purposes, since a cellular material can be represented as a continuum, avoiding the need to model the detailed micro structure, a step that can be extremely computationally expensive.

The arrangement and distribution of unit cells within a given domain can be further divided into stochastic or non-stochastic organization based on the tessellation of the unit cell. Stochastic cellular materials exhibit variation in morphology, such as pore size, shape and even topology throughout the structure. A periodic cellular material has a regular and repeating unit cell that can be captured through translation along a periodic tessellation, whereas an aperiodic lattice the unit cell cannot be captured through translation. Foam illustrates the concept of an aperiodic lattice, where the unit cells are to rhombic dodecahedrons or tetrakaidecahedrons, however adjacent cells are not all the same size or shape [25, 34].

Porous materials are widely used in orthopedic applications due to bones’ ability to form within the porous network in order to provide a strong bond between the implant and the host bone.

2.3 Porous Materials for Bone Interfacing Implants

The interconnected porous network that allows for bone ingrowth is critical for the success of cementless bone interfacing implants. For load-bearing applications, porous metallic scaffolds are predominantly used in bone surgeries because of the severe mechanical strength requirements to support the aforementioned loads during both static and dynamic activities. Even with its improved mechanical strength, a metallic porous network, namely a scaffold, is predominately used as a coating on a solid metal substrate. A variety of methods have been developed to produce porous metallic scaffolds with a homogeneous pore size distribution that provides a high degree of interconnected porosity. For bone ingrowth applications, the processes used to build porous materials include powder metallurgy [35], chemical vapor deposition coating of carbon scaffolds [38, 39], plasma spraying [40], space holder methods [41, 42], and self-propagating high-temperature synthesis [43]. Additionally methods, such as sintered beads [44], fiber mesh [45] and thermal spray processes [46], have been also used to create a porous coating on bone interfacing implant surfaces to enable bone ingrowth. These coating processes retain intrinsic limitations. For instance, the resulting cellular architecture displays an almost uniform distribution of pore size with homogenous porosity. Porous structures with a defined pore shape and size and with a specified porosity distribution, a gradient, or a pattern is very difficult to achieve [47]. In addition, the spatial distribution of the pores is mostly random, and control of the final pore geometry is generally very challenging. Porous coatings can also suffer from lack of adherence to the substrate and non-uniformity of the layer thickness. The thickness of porous coatings might also be insufficient to facilitate effective bone tissue ingrowth [48, 49]. Detachment from the substrate, crack formation under fatigue, and granulation are other problems to which such coatings are prone to [48, 50].

2.3.1 Tantalum: Fully Porous Material

Among the porous materials currently used in orthopedics for bone ingrowth, Tantalum foam is particularly interesting because, in addition to its exceptional performance as a coating, it has also been used for fully porous implants that require some (limited) degree of load bearing[39]. Tantalum foam is created through deposition of Tantalum onto a reticulated vitreous carbon skeleton through means of chemical vapor infiltration. This results in a fully porous material with almost dodecahedron cells. The resulting porous material is 99% Tantalum, and 1% Carbon, with porosity ranging from75% to 85% and pore size from 400-650 microns[25]. The stiffness of Tantalum foam is very similar to bone with stiffness ranging from 2.5-3.9 GPa and mechanical strength of 35-51 MPA in quasi static compression [51, 52].

Additionally, Tantalum shows excellent bone ingrowth, with bone ingrowth up to 80%, with Haversian remodeling apparent within the porous Tantalum [25]. Compared to other sintered bead coatings, the increased amount and rate of bone ingrowth of tantalum is thought to contribute to its excellent interface strength. Tantalum foam is commonly used as a porous coating on total hip and knee replacements; however, since it is not limited to a coating, it can also be used as a fully porous construct. Fully porous Tantalum has been employed as bone augments, acetabular cups, osteonecrosis implants, and also in conjunction with bone grafts for vertebral fusion [39, 53]. However all applications of fully porous tantalum implants are released from the need to satisfy severe requirements of structural support.

In addition to its excellent bone ingrowth, Tantalum foam is fully porous, and has improved load bearing properties compared to other porous materials used in orthopedics. Nevertheless, Tantalum foam retains several limitations. A major limitation is that the structure exhibits uniform porosity, with homogenous pore size and shape distribution throughout the domain. In addition, although it possess favorable stiffness comparable to that of bone and better strength compared to other porous materials for bone ingrowth, it still leaves room for improvement to extend fully porous implants beyond fusion cages and screws to other load bearing applications with more sever loading conditions, such as fully porous arthroplasty stems.

2.4 Microarchitecture Materials

Although stochastic cellular materials, such as Tantalum, are widely used in orthopedics, they cannot be easily tailored to provide a range of required properties such as high porosity for ingrowth at bone interfaces, and lower porosity internally for improved strength. Recent advances in additive manufacturing (AM) allow for free form fabrication of complex, precisely engineered structures in a variety of materials at smaller and smaller microstructural length scales. This in turn has greatly increased the accessibility of microarchitecture lattice materials. Using AM the unit cell can be conscientiously designed to achieve a specific outcome, and furthermore can easily be controlled throughout the structure. These materials can have tightly controlled morphology to precisely tailor their mechanical and biological response. Additive manufacturing can employ a variety of materials including polymers, ceramics, metals, and even direct printing of biological materials or combinations of different material types [54, 55].

Additionally, materials can be selected in such a way that the materials will degrade over time, as it is replaced by natural tissue. Although the possibility of resorbable or biological implants to restore function are very exciting, there are some notable technical and regulatory hurdles, such as ensuring and maintaining sufficient strength while growth occurs for load bearing applications, as well as regulatory classification [56, 57].

Within the scope of this thesis, the focus is on AM fabrication of microarchitecture lattice materials made with Ti6AL4V through a selective laser melting (SLM) process due to their superior mechanical strength and their excellent bio-inertness [58]. This research work provides a methodology for understanding the interplay between factors that govern mechano-biologic response, while simultaneously satisfying bone ingrowth and manufacturing limitations. Selected points are examined to assess their morphological parameters after manufacturing. The stiffness and strength along with the extent of bone ingrowth is experimentally determined to provide a reference to existing fully porous biomaterials such as tantalum. To demonstrate the potential of a fully porous material, a fully porous hip replacement is fabricated and experimentally tested to show how the material can be tailored to reduce a functional aim: stress shielding in a total hip replacement.

2.5 Thesis Objective

The overarching objective of this thesis is to examine high strength fully porous biomaterials for use in bone interfacing implants in orthopedics. This is achieved through a twofold approach employing both a general material perspective and a functional application perspective. This combined approach serves to highlight the general features of high strength fully porous biomaterials, as well as to demonstrate how porous biomaterials can be tailored to achieve specific functional requirements.

From the perspective of the porous material characterization, the objectives are as follows:

- Present a methodology to systematically examine and visualize how fully porous microarchitecture materials can be successfully designed and manufactured while respecting bone ingrowth requirements and additive manufacturing limitations.
- Examine the manufacturability of lattice samples fabricated with SLM within bone ingrowth constraints by comparing the manufactured morphological parameters of porosity, pore size, and strut thickness relative to the nominal designed values.
- Examine the experimental mechanical compressive properties of high strength fully porous biomaterials, including stiffness, 0.2% offset yield strength, and first maximum yield strength.
- To relate the structural efficiency of the lattice microarchitecture to the reported performance of existing porous biomaterials, namely Tantalum foam.

These objectives serve to form a framework for understanding the complex relationships governing morphological, biological, and mechanical performance that guide the embodiment of what for a specific application within the MSK system.

From a functional perspective, the objective is to assess functionality of fully porous biomaterials for use in a total hip replacement. In particular, the following two research questions are addressed:

- Can an optimized fully porous hip replacement implant be manufactured using SLM?

- Does a fully porous implant show a reduction in strain shielding in an experimental in-vitro evaluation in composite femurs?

This functional application serves to show how the generalized material understanding can be tuned to achieve a specific functionality to improve clinical outcomes through the use of fully porous biomaterials.

This thesis shows for the first time, to the author’s knowledge, bone resorption secondary to stress shielding can be reduced through the use of a tailored fully porous material for total hip replacement through in-vitro experiments. This represents a dramatic breakthrough in bone interfacing implants, and clearly demonstrates the utility of high strength porous biomaterials.

Chapter 3: Material Perspective

This chapter examines two stretch dominant high strength fully porous biomaterials, and compares their strength and potential for bone ingrowth to tantalum foam. The section provides an overview for the advances in additive manufacturing for developing bone interfacing implants, along with a review of design methods for creating bone interfacing implants. A visualization method is presented to understand the interaction of morphological parameters of the unit cell, while respecting bone ingrowth requirements and manufacturing limitations. Within the admissible design space, four samples are selected across the design space. The fully porous biomaterials are morphologically characterized through micro CT, and mechanically tested in quasi-static compression to determine their yield strength and effective stiffness. The results of bone ingrowth from a biological study conducted by collaborators are incorporated to provide an overarching comparison in both mechanical properties and bone ingrowth relative to tantalum foam.

3.1 Porous Materials Fabricated Using Additive Manufacturing

Recent advances in Additive Manufacturing (AM), such as Electron-Beam Melting (EBM), Selective Laser Melting (SLM), Stereo Lithography Apparatus (SLA), enable the precise manufacturing of complex three-dimensional structures with controlled architecture that can be used as biomaterials [29, 59]. AM methods enable scaffold fabrication with controlled cell topology, porosity, pore shape and size, interconnectivity, and mechanical properties, all of which greatly influence osseointegration. AM processes can also build porous structures with defined pore size and porosity gradients [47]. A porous biomaterial with an optimum microstructure can be designed and manufactured to achieve a desirable mechanical response and functional environment for bone ingrowth based on its specific functional application.

Shape optimization, topology optimization, and the selection of a unit cell from a library of implantable microstructures are common approaches used to design a porous biomaterial using AM techniques [59-63]. In shape optimization the cell topology cannot be changed, rather the shape of the pore is optimized to achieve the required effective stiffness and mass transport properties. Topology optimization can be used as a more general approach to obtain optimal material distribution, and may obtain dissimilar pore shapes to meet specified design requirements [62]. While used in porous material design, topology optimization has certain deficiencies. A major one is the complexity in implementing a scheme that concurrently takes into account all relevant mechanical, biological, and manufacturing factors. In previous implementations of topology optimization, there has been almost no control on the size and shape of the pores, factors that may have a significant impact on the implant performance due to osteoblast response [64]. Moreover, in hierarchical topology optimization, where different microstructures are designed at each location of the implant to meet specific mechanical and perfusion properties, there is often a lack of interconnectivity between dissimilar cell topologies [65]. This can cause stress concentration at the interface, resulting in interface fracture and low mechanical integrity.

An alternative approach is to select a lattice material from a library of unit cells [49, 59, 66]. The microarchitecture of the unit cell can be tailored to provide sufficient mechanical properties for the porous biomaterial to support physiological loadings. Moreover, three-dimensional structures with controlled porosity, pore shape, and pore size gradients can be designed to provide an optimum biological environment for bone ingrowth [47, 64, 67]. The unit cell interface can also be designed to enable a complete load transfer between adjacent blocks [68].

Many studies have shown the use of several AM processes to manufacture unit cells and to evaluate the effect of cell morphology on mechano-biological properties, either *in vitro* or *in vivo* for tissue affinity [69, 70]. While significant, these studies do not address an important problem, the relation of pore topology, pore size, porosity and strut thickness, with the mechano-biological response of a porous material. Rather, the authors generally select a cell topology, and with no systematic approach iteratively change only two of the morphological properties of the unit cell (e.g. cell size, strut thickness, pore size, and porosity) to obtain a manufacturable design. This process, however, does not give a full perspective of the feasible design space and the inherent trade-offs. It often leads to the design of porous architectures with pore size larger than 800 microns, which can inhibit the rate of ingrowth thereby increasing the patient’s time to recovery [67, 71]. Moreover, this procedure does not provide any insight into how the morphological properties of the unit cell, such as unit cell size, pore size, porosity, and strut thickness, are interrelated, and how the change of one parameter can influence the others. Furthermore, to the best of the authors' knowledge, there is also no study that shows how manufacturing and bone ingrowth requirements can affect the admissible design range of a given cell topology for bone ingrowth applications.

This chapter also presents a systematic methodology for understanding the interplay between the morphological parameters and the relationships that govern the mechano-biological properties of structural porous biomaterials. The method enables the generation of design maps where morphological attributes of a given cell topology, such as pore size, porosity, cell size, and strut thickness, are conveniently visualized along with both manufacturing constraints and bone ingrowth requirements. The insight that can be gained from these charts eases the design and additive manufacture of a porous structural biomaterial. The methodology is applied and demonstrated in this chapter with two high-strength topologies: the Tetrahedron and the Octet truss. The cells belong to the class of high-strength and stiffness topologies which are stretch dominated, i.e. their struts axially deform under load [72-74], hence their suitability for load-bearing orthopedic applications. Their morphological parameters are expressed through a parametric model, which is used to obtain the admissible cell topology domain, bounded by manufacturing and bone ingrowth requirements. Ti-6AL-4V representative samples are manufactured via Selective Laser Melting (SLM), and micro-CT analyzed to assess their morphological characteristics with respect to the nominal designed values. Uniaxial compression testing is performed to obtain the effective elastic modulus and yield strength of the manufactured samples. Finally, results from *in vivo* clinical experiments using a canine model conducted by our research collaborators are given to assess bone ingrowth after 4 and 8 weeks and to evaluate the potential use of structurally efficient topologies in bone replacement implants.

3.2 Unit Cell Selection

The Tetrahedron cell and the Octet truss cell are selected as architype topologies (Figure 3). Both topologies satisfy the Maxwell's criterion for static determinacy, implying that they are stretch dominated for all loading states. Based upon the topology of the unit cell, lattice materials are generally classified into two main groups, namely bend dominated and stretch dominated [72]. The cells belonging to the former collapse by the local bending of the cell struts at the nodes thereby, leading to lower mechanical properties. Cells falling in the latter group, on the other hand, collapse by the stretching of their struts, a failure mechanism that provides a higher stiffness and strength per unit mass as compared to bend dominated topologies. For load bearing orthopedic applications, a fully porous biomaterial should have sufficient mechanical strength to withstand a combination of physiological loadings. Hence why stretch dominated cell topologies are here selected to create a porous biomaterial with sufficient mechanical properties and higher porosity for bone ingrowth.

3.3 Development of Cell Topology Domains

The mechanical and biological properties of a unit cell for a fully porous biomaterial are governed mainly by the pore topology, nodal connectivity, porosity, pore size, and the monolithic material from which they are made [34, 61]. The way these morphological parameters are correlated is not necessarily intuitive; neither is how each of them can control mechanical properties and biological response. For this reason, we develop a parametric model to describe the geometry of a unit cell, and subsequently use it to visualize its morphological properties on a design chart. This allows to visually inspect what porosity and pore size combinations exist and are feasible to manufacture. Given that porosity is strongly related to mechanical properties, it also allows for an estimation of the mechanical properties for a given cell design.

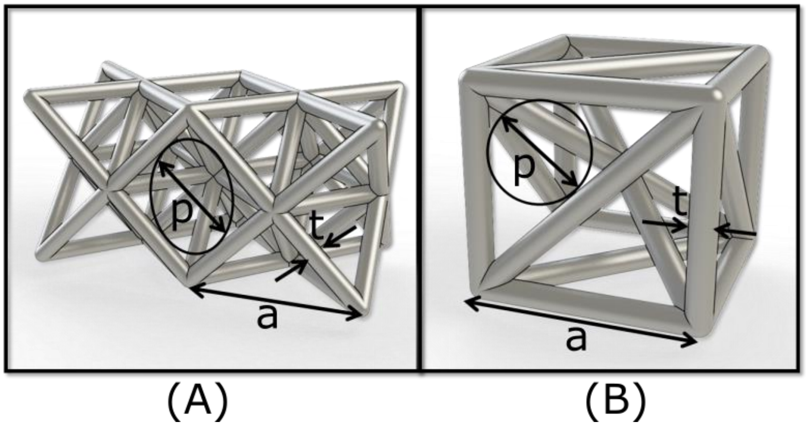

Figure 3: Morphological parameters of A) Octet truss and B) Tetrahedron topology.

To develop a parametric model for each of the unit cells shown in Fig. 1, we observe that the overall cell geometry can be controlled by two parameters, strut thickness ‘t’ and unit cell size ‘a’, provided the cross-section of all the struts is circular and untapered along their length. With these assumptions, each unit cell can be scaled to any desired size. The pore size ‘p’ in this study is measured at the bone-implant interface and is defined by the diameter of the largest circle that can be inscribed within either a polygon face of a unit cell, or a polygon formed by two adjacent unit cells (Figure 3). Porosity is also measured from the percentage of void in a fully solid cell as: $Porosity\ (\%) = \left(1 - \frac{V_p}{V_s}\right) \times 100\ (eq. 1)$. Where V_p is the volume of the porous unit cell and V_s is the volume of the fully solid unit cell.

For each cell topology, by varying systematically the strut thickness and cell size within given ranges, the resultant pore size and porosity in contour maps with strut size on the y axis and pore size on the x axis are generated. The values of porosity and cell size are illustrated as isometric lines, which describe how pore size and wall thickness change with porosity and cell size. The chart can ease the visual understanding of the relation between the morphological parameters of a unit cell. To find the feasible design domain for a unit cell topology, other constraints and requirements need to be identified and visualized, two of which are:

1. Bone ingrowth requirements- For bone ingrowth, pore size and porosity of the lattice should be between a suitable range; with pore size between 50 microns to 800 microns, and the porosity higher than 50% [28, 75]. These values form an upper and lower bound

for pore size and porosity which are included as red lines in the design chart (Figure 4 and 5).

2. Manufacturing constraints- Most of the current AM technologies, such as SLM and EBM, used to build cellular materials are limited to produce a nominal wall thickness (strut thickness) of 200 microns, although this limit is process-dependent [49, 76] and can be lower [76, 77]. This limit is thus included in the design chart with a horizontal red line.

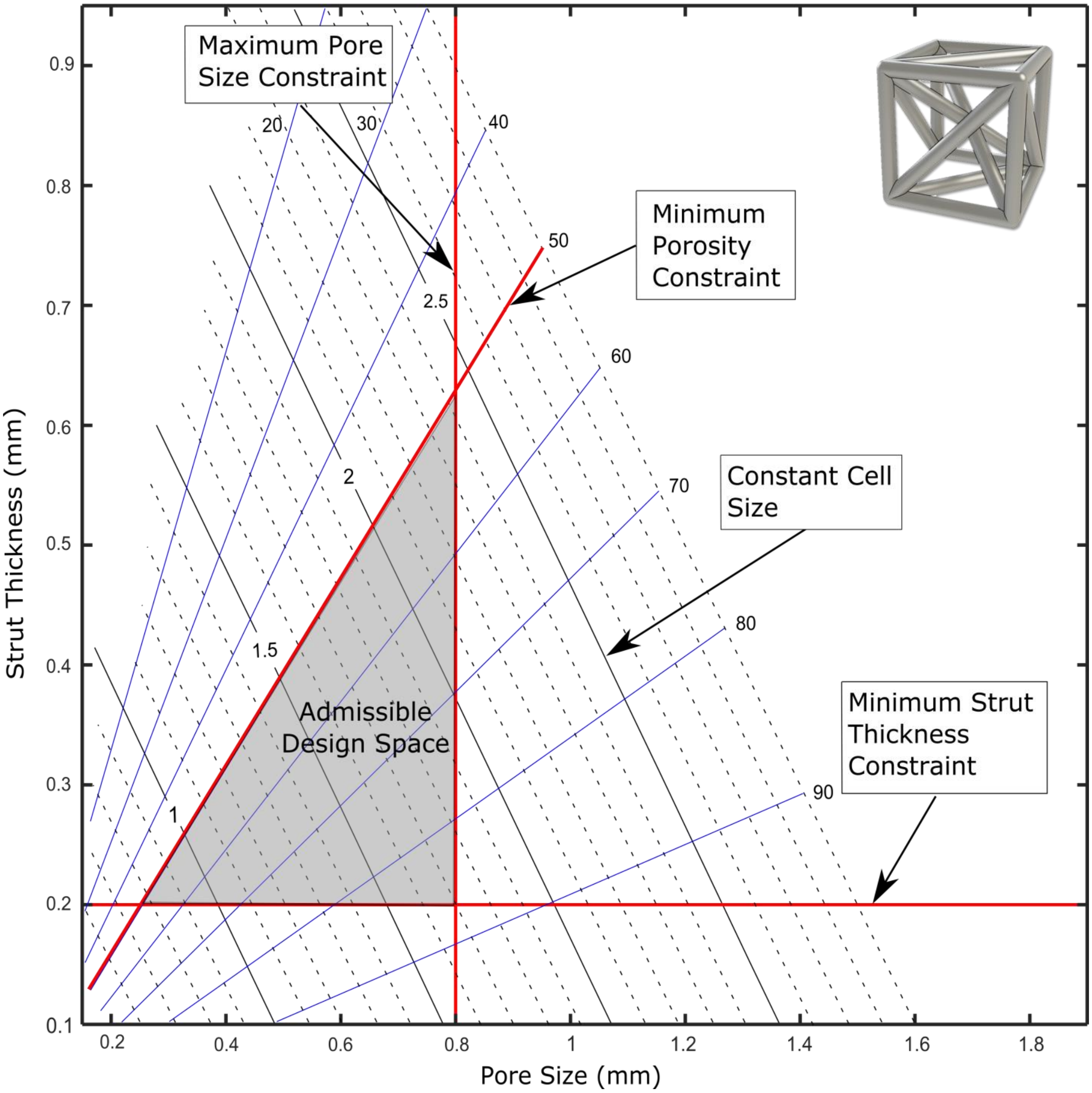

Figure 4: Tetrahedron admissible design space.

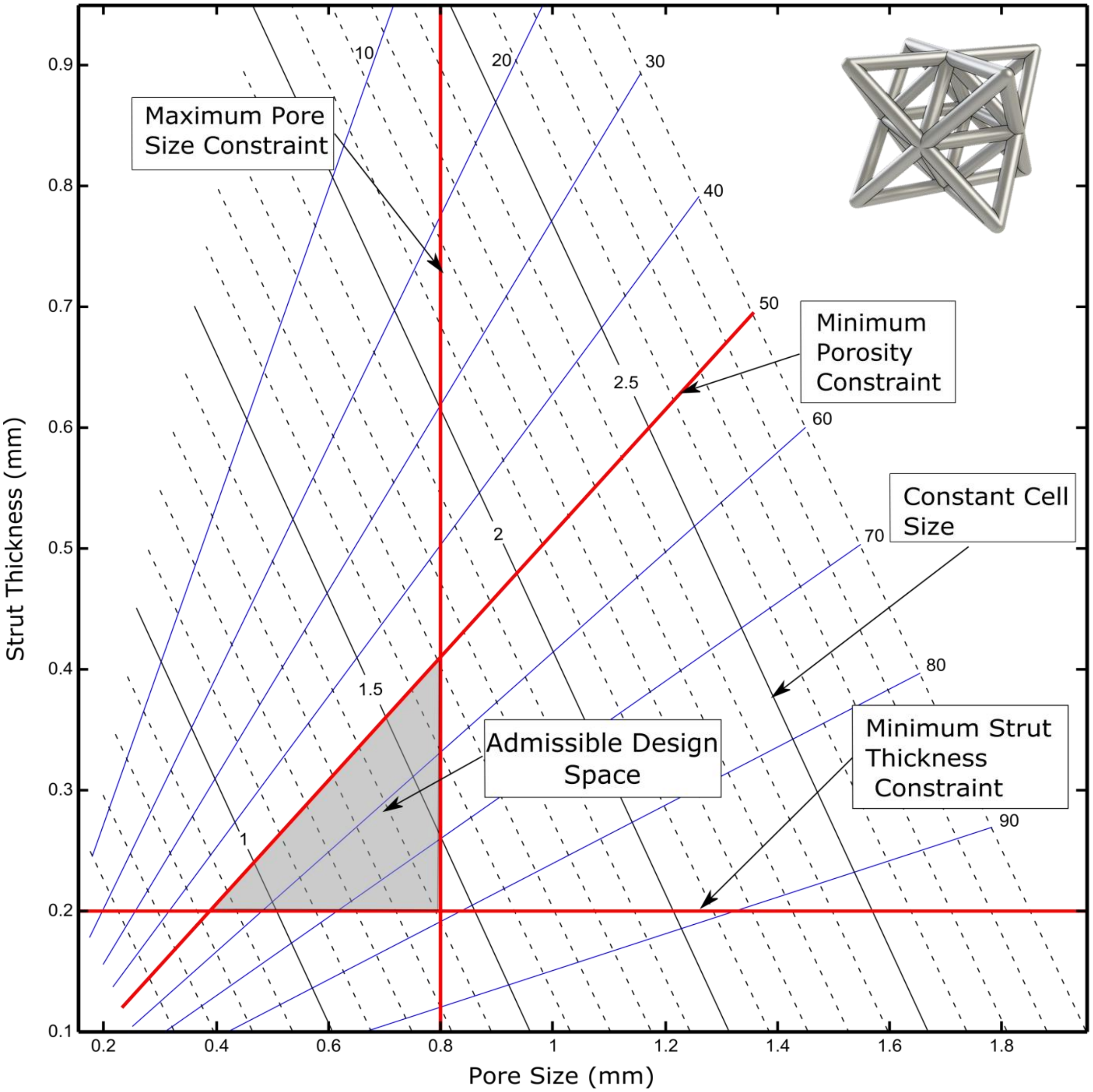

Figure 5: Octet truss admissible design space.

Within the bounds and constraints defined above, the feasible design domain (or space) for each given topology are inscribed, as shown in Figures 4 and 5. All the designs falling within this domain are acceptable solutions that meet the criteria defined above. Each unit cell topology is characterized by its own design space. For example, the solution space for the Octet truss unit cell (Figure 5) is smaller than the solution space of the Tetrahedron-based unit cell (Figure 4). For a given cell size and strut thickness, the Octet truss unit cell is denser than the Tetrahedron-based topology. In addition, the size of the pores at the Octet truss surface is also larger than the

Tetrahedron-based topology. From an alternate perspective, due to the minimum strut thickness constrained by the machine and build parameters used for fabrication, a tetrahedron topology can be fabricated with higher porosity as compared to an Octet truss. Examination of the charts in figure 4 and 5, reveals the highest possible porosity sample at the intersection of the minimum manufacturable thickness and the maximum allowable pore size. The maximal attainable porosity of the tetrahedron within the given constraints is over 85%, whereas the octet truss is limited to below 80%. To understand how morphological parameters of the unit cells govern the mechano-biological properties of structural porous biomaterials, representative solutions are selected from the design chart and manufactured to perform mechanical and biological testing, as described in the following sections.

3.4 Selection and Design of Representative Samples

To experimentally validate the feasibility of a cell topology domain, representative samples are selected and manufactured with SLM. The morphological properties of these samples, including pore size, porosity, wall thickness and cell size, are measured and compared with their nominal design values. The samples are also mechanically tested under a uniaxial compression test to obtain the effective uniaxial Young's modulus, 0.2% offset yield strength, and first maximum compressive strength. The following criteria are used to select the points from the design domains shown in Figures 6 and 7 for the Tetrahedron and Octet truss respectively:

- Four design solutions at 50%, 60%, 70% and 75% values of porosity are chosen for each topology to cover the entire porosity range of each cell topology domain. The porosity of the Octet truss and Tetrahedron are kept as close as possible to these nominal values while respecting the aforementioned constraints. The pore size is also kept constant throughout the relative density range within each topology that corresponds to the pore size used in the canine model study that provides the amount of bone ingrowth.
- The strut thickness of each cell topology is kept constant for each value of porosity. This choice limits the variability that may arise from manufacturing deviations, e.g. thickness variation measured from the manufactured struts that may emerge from AM process limitations.

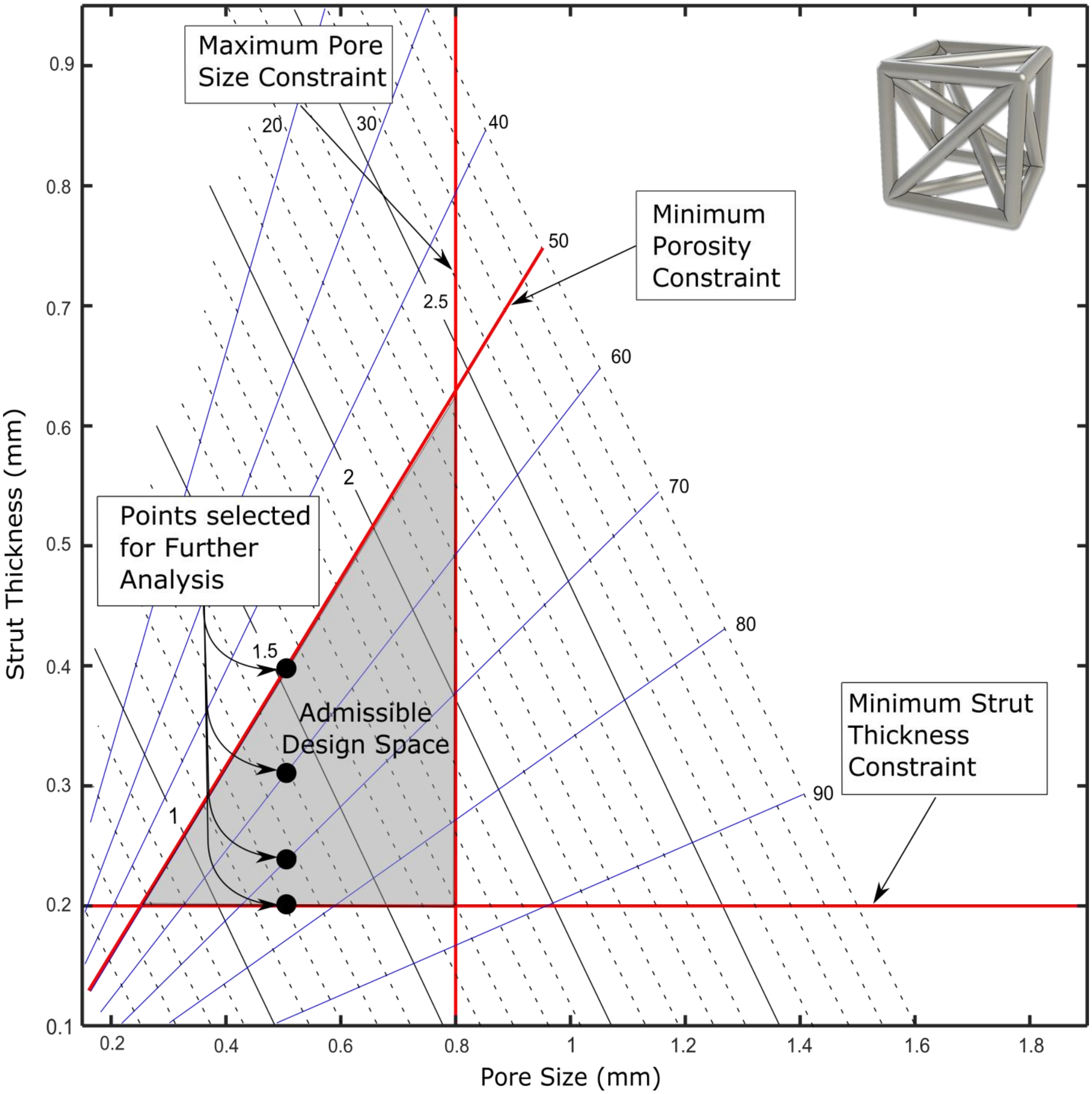

Figure 6: Representative Tetrahedron samples selected for further analysis.

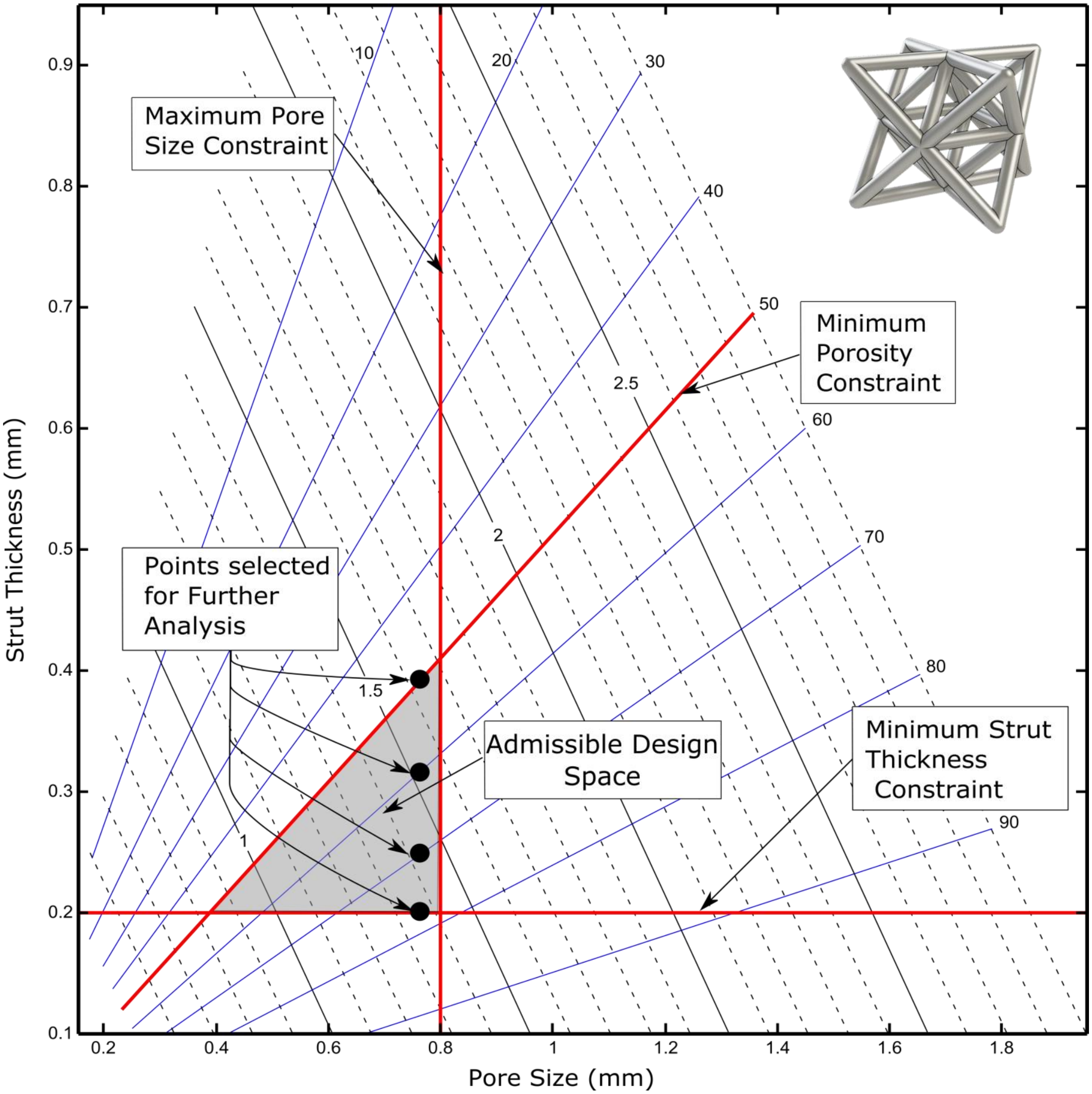

Figure 7: Octet truss samples selected for further analysis.

With respect to mechanical testing, five replicates for each cell topology are prepared according to the ISO 13314:2011 [78]. Table 1 lists the parameter values for the domain points of each topology. The solutions closely match the desired values of the porosities, and the strut thicknesses of both topologies are identical at the corresponding porosity. In addition, for each unit cell, the pore size is prescribed. In particular, 500 microns for the Tetrahedron-based unit cell and 770 microns for the Octet truss unit cell. Table 1 reports the geometric details of the specimens that are mechanically tested. The specimens have a prismatic geometry, and their spatial dimensions, i.e. height, width and depth, are at least 10 times the average pore size, as per the ISO 13314:2011 standards. . Moreover, the specimen length to edge length ratio is between 1 and 2.

To perform biological testing, transcortical implants for a canine model study that measures the amount of bone ingrowth in periods of 4 and 8 weeks where designed. Six Tetrahedron and four Octet truss transcortical implants with a cylindrical shape and an outer diameter of 5mm and a height of 10mm were manufactured using SLM process. The manufactured Tetrahedron topology had an average porosity of 55.51% and pore size of 438 microns. The manufactured Octet truss had an average porosity of 69.88% and pore size of 772 microns. The values of porosity and pore size fall within their admissible design space that accounts for bone ingrowth constraints, and they correlate well with the design points in the design charts of Figures 5 and 6.

Table 1: Geometric details of the test samples

Unit cell	#	Porosity	Strut Thickness (mm)	Unit Cell Size (mm)	Pore Size (mm)	Height (mm)	Width (mm)	Depth (mm)
Tetrahedron	1	49.8%	0.39	1.52	0.5	20.15	12.55	12.55
	2	59.16%	0.31	1.385	0.5	18.31	11.39	11.39
	3	68.85%	0.24	1.27	0.5	16.75	10.4	10.4
	4	74.74%	0.2	1.2	0.5	15.8	9.8	9.8
Octet truss	1	50.03%	0.4	1.66	0.77	21.98	13.68	13.68
	2	59.8%	0.32	1.54	0.77	20.34	12.64	12.64
	3	69.7%	0.25	1.44	0.77	18.97	11.77	11.77
	4	77.28%	0.2	1.37	0.77	18.01	11.16	11.16

3.5 Manufacturing

The samples were produced using the SLM process by the Renishaw AM250 with building direction as shown in Figure 7. The AM250 uses an Nd:YAG laser in Q-switched mode with a maximum power of 200 W and a laser spot diameter of 70 µm. Ti_6VA_{l4} powder (grade II according to ASTM F67, SLM Solutions) is used. The powder size is between 15-55 µm, and 95% of particles have a powder size smaller than 50 µm. The powder layer thickness was 30 µm. After fabrication, the samples were cleaned from adhering powder particles by compressed air, and post processing heat treatment at 720 C^0 under Argon for 2 hours.

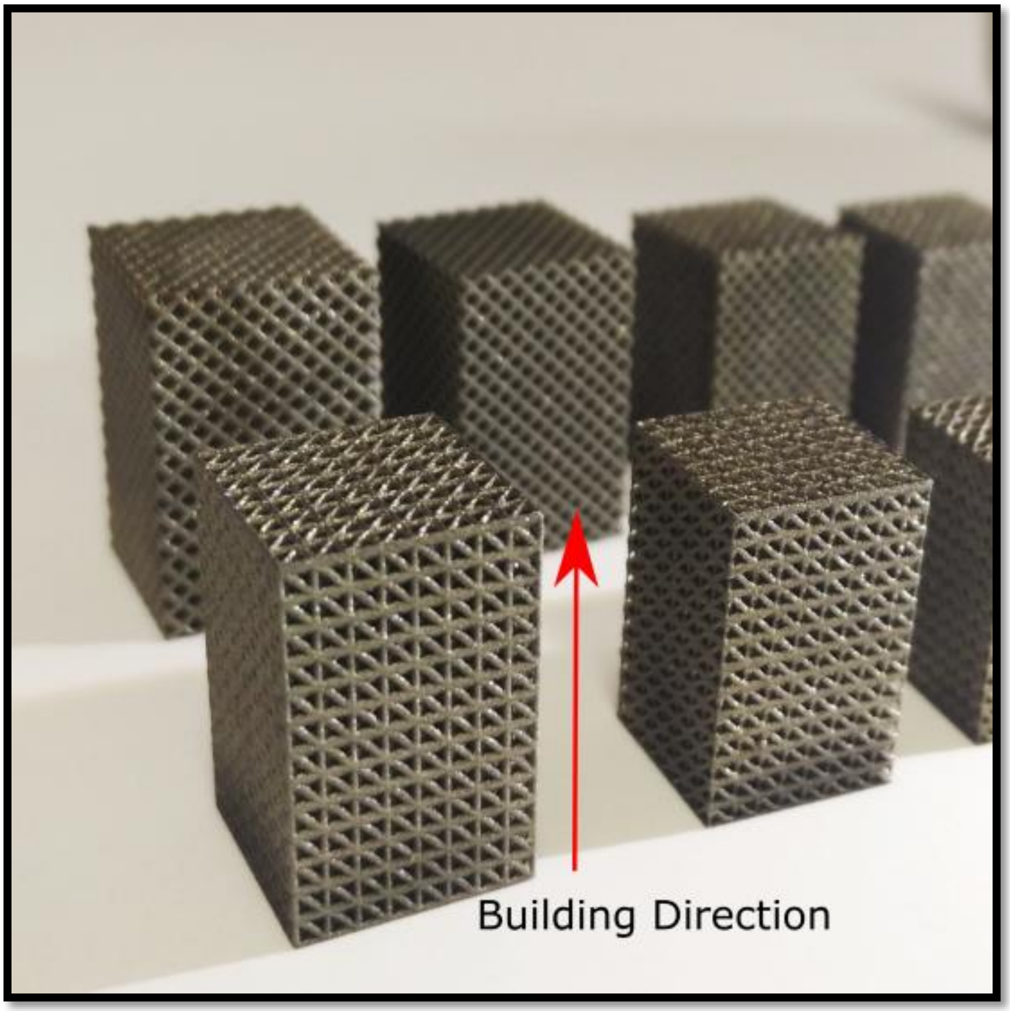

Figure 8: Vector showing the build direction.

3.6 Morphological Evaluation

3.6.1 Methods

From each design point in the design space (Table 1), one sample was randomly selected and scanned using a SkyScan 1172 (high-resolution micro-CT). During the acquisition, each sample was rotated over 360° in steps of 0.5°, using 103 KV energy and 96 μA intensity. After each rotation step, 5 images were acquired and the average radiograph recorded. The images were then reconstructed into cross-sectional images with a commercial software package (NRecon, Skyscan N.V., Kontich, Belgium). The reconstructed micro-CT dataset had an isotropic voxel size of (17.6 µm). Using this dataset, a series of image slices were taken from within the build plane and orthogonal to the build plane. Based on the image slices, the strut thickness and pore size were measured with the ImageJ software package (National Institutes of Health, Bethesda, MD) to correspond with the values defined in Figure 3. Additionally, strut thickness measurements taken orthogonal to the build plane were divided based on the designed strut angle to capture manufacturing discrepancies outside of the build plane. To measure the porosity of the remaining 5 replicates, the samples were weighed and normalized by their bounding dimension volume.

3.6.2 Results: Cell Morphology: Designed vs. Manufactured

Using micro-CT analyses, the key morphological parameters, including porosity, pore size, and strut thickness, of the samples were measured and compared with the nominal designed values. Figure 8 shows the comparison between designed and measured values for the Tetrahedron and Octet truss lattices. The error between designed and manufactured porosity increases with the increase of the designed porosity. For the Tetrahedron lattice, the difference reaches up to 15% at the highest porosity of 75%. The porosity determined by the samples that underwent micro-CT is in agreement with the mass to volume calculations, thereby indicating that the automatic thresh-hold level used in the reconstruction software is appropriate. Furthermore, there is consistency among the porosity values measured for each sample, another factor indicating that no major discrepancies exist between the replicates.

Figures 9c and 9d show the comparison between the designed value of strut thickness and the average value measured on the manufactured samples. From micro-CT analyses, we observed that strut thickness variation is dependent on the strut angle. Therefore, struts are measured based on their orientation with respect to the building plane and compared with the designed values. For Tetrahedron lattice, struts are measured at 0, 45, 90 degree with respect to the building plane and also in the building plane. However for Octet truss, struts are measured at 0 and 45 degree and in building plane as Octet truss does not possess a strut normal to the building plane. Figure 9c and 9d clearly show that struts measured at 0 degree with respect to the building plane are significantly thicker (255 ±60 microns) than their designed values due to over melting of struts. For struts that are normal to the building plane, the manufactured thickness is slightly lower than that of the designed sample (-90 ±37 microns). The struts aligned at ±45 degrees had a significantly smaller error than the struts at zero degrees, and more than the struts aligned in the build direction (61 ±52 Microns). In the building plane, the thickness of the manufactured struts is in very good agreement with the designed values (35 ±37 Microns). Measured pore sizes are all lower than the designed values, with deviation between designed and manufactured pore size increasing as the porosity increases. Figures 9e shows that the average pore size deviation for the Tetrahedron lattice increases from 15% to 32% for designed porosity of 50% to 75%. For Octet truss, we can see in Figure 9f this deviation increases from 21% to 50% for designed porosity of 50% to 75%.

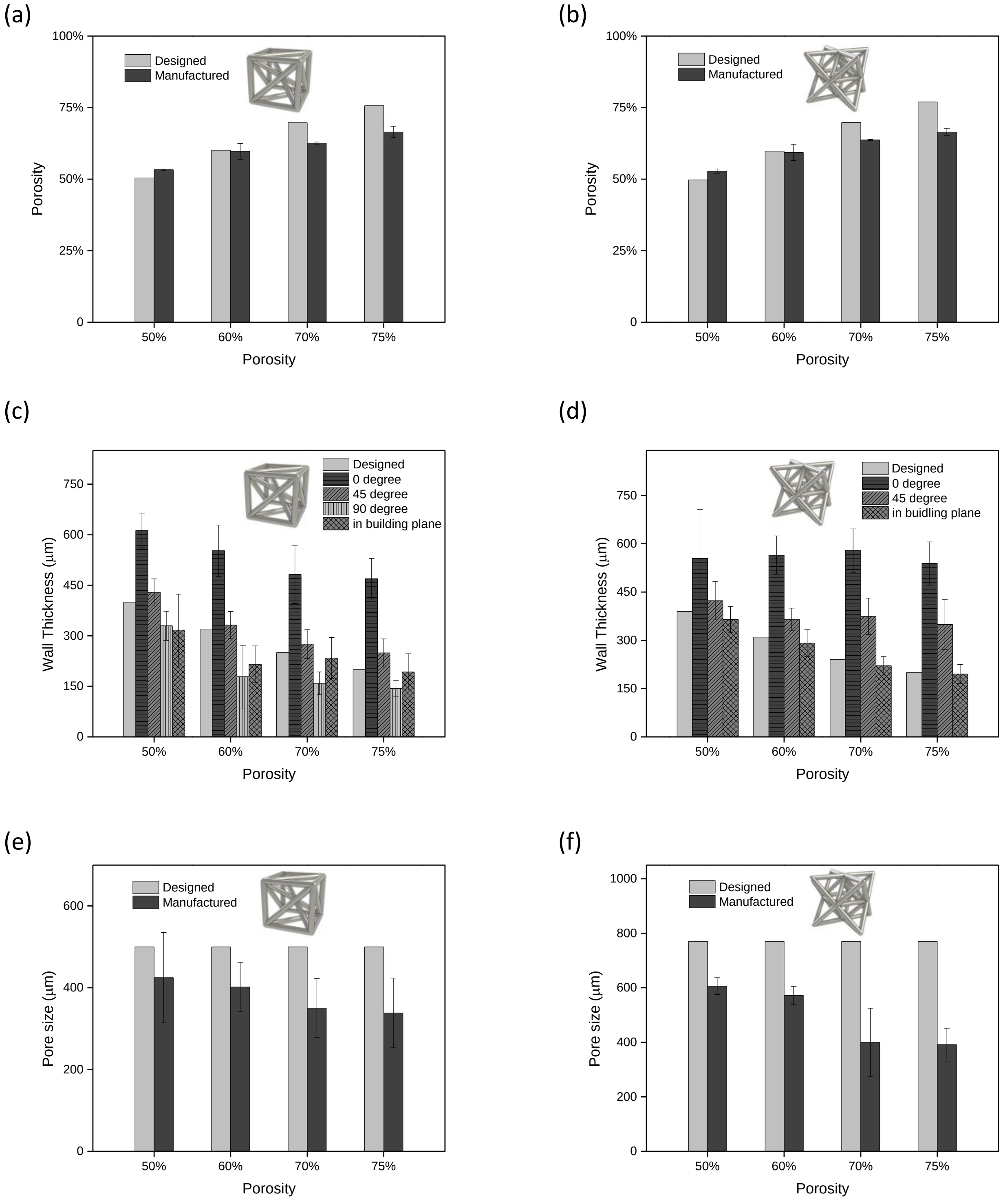

Figure 9: A) and B) Average porosity. C) And D) strut thickness. E and F) Pore size of Tetrahedron and Octet truss lattices. All of the morphological parameters are obtained via micro-CT image analysis and compared to the respective designed geometries.

3.6.3 Discussion: Discrepancy between Manufactured and Designed Samples

The design charts do not exactly predict the measured porosity and pore size of the manufactured samples. The reason can be attributed to deviations between a designed sample and its manufactured counterpart. A key factor is the deviation observed in the strut thickness and strut cross section between manufactured and designed samples. The former shows a deviation in the strut thickness with higher values than the designed ones. In addition, the measured error was dependent on the angle a strut forms with respect to the building plane; this error was most apparent in overhanging horizontal struts. Due to the over melting out of the build plane, the strut cross section is no longer circular and it changes for each strut orientation within a given cell topology. The over melting observed in the manufactured samples leads to a geometry change, from circular to elliptical, of the cross section for each strut that is not vertical. Errors in cross section geometry along the struts incur a deviation from the design charts, where each unit cell strut is modeled with a constant thickness and cross sectional area. Variations of strut thickness as a function of the angle with respect to the building plane is well documented in the literature, and can be attributed to the staircase effect for angled struts and the difference in heat transfer properties between solid struts and surrounding powder [79, 80]. The increase of strut thickness leads to a decreased porosity and pore size in the manufactured samples.

To clearly illustrate the increase of manufactured strut thickness due to semi-melted powder agglomerations, a representative unit cell from manufactured samples was reconstructed and overlaid with the designed unit cell. Figure 9 shows a 3D reconstruction of the Tetrahedron cell at a design porosity of 75%, overlaid with its designed counterpart. The figure shows that the strut thickness of manufactured samples is significantly higher than the designed strut thickness. At the corners, we also note material agglomeration, leading to a fillet-like feature. A decrease in pore size and porosity can decrease the structure permeability, thereby potentially inhibiting the biological performance of the porous materials [81, 82]. Comparing to Figures 9e and 9f, it is observed that the discrepancy of manufactured porosity and pore size increases with the porosity. This trend can be partially attributed to the absolute error of the strut thickness, which is constant for all the designed strut thicknesses. The error normalized by the designed strut thickness is larger for smaller struts, and it reaches nearly 200% for samples with the highest designed porosity and the smallest strut thickness. The relation between the increase in strut thickness and decrease in porosity can be intuitively understood by examining the design charts. If the wall thickness is increased for a given cell size, it reaches regions with a lower porosity and pore size. The design chart allows for an intuitive visualization of how manufacturing errors can affect the resulting morphological parameters for any given topology. From these domains, the impact of the manufacturing errors, e.g. strut thickness, on the resultant porosity and pore size, can be assessed as the cell size decreases.

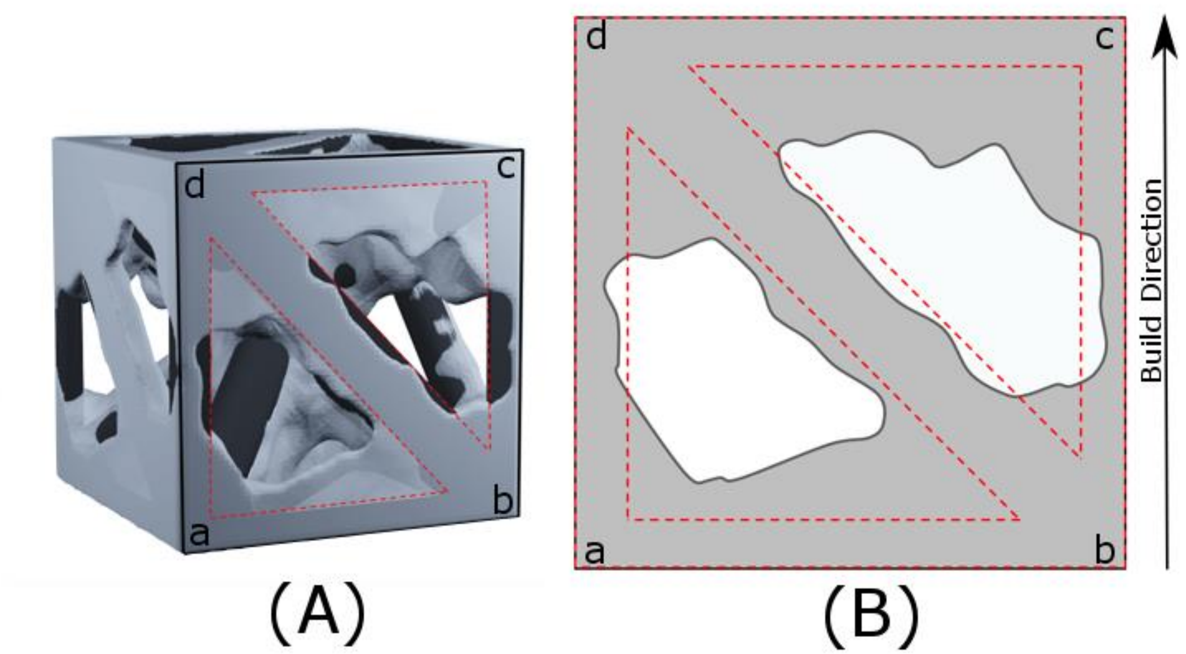

Figure 10: A) Reconstructed Tetrahedron cell at 75 % porosity from CT (translucent grey) overlaid with designed unit cell (black). B) Front view (abcd) of the cell with the designed geometry outlined in red dashed lines.

3.6.4 Minimizing the Discrepancy between Predicted and Manufactured Morphology

To minimize the difference between the predicted properties, as visualized in the design charts, and the manufacturing outcomes, two methods can be pursued. The first, obvious, although non-trivial, is to reduce the manufacturing strut thickness error. This procedure can potentially be implemented through machine parameter tuning, post-processing, such as acid etching and electro polishing, and design compensation strategies [83]. The additional post-process can have a substantial effect on the mechanical properties, and biological performance [70, 84]. Machine parameter optimization can also lead to a strut resolution improvement with a reduction of the minimum strut thickness below the nominal 200 micron limit, currently plotted in the design space charts. A second method is to incorporate the manufacturing errors into the geometrical model used to create the design charts. This strategy permits visualizing the properties of the manufactured samples on the charts, thereby accounting for any variation in the strut cross-sectional profile and thickness throughout the unit cell. The design charts, therefore, could capture the impact that prescribed manufacturing parameters and process errors of a given manufacturing technology might have on the design domain of a given cell topology.

3.7 Mechanical Characterization

3.7.1 Methods

For the compression testing of samples, a 50 KN MTS servo-electric testing machine was used. Five replicates for each design solution were tested. The samples are compressed with a constant strain rate of 0.01 s^{-1}. The stiffness, yield and ultimate strength of the each sample were determined from the stress–strain curves. The ISO-13314 standard was followed to determine the sample stiffness as the maximum slope of the stress–strain curve. The yield strength was measured using the 0.2% offset method based on the maximum stiffness, and the first maximum compressive strength was also recorded. The mechanical properties were compared between the two topologies at each design density using an unpaired two sample Welch's unequal variances t-test. The two tailed P-value is reported in table 2, with statistical significance at $P<0.05$.

3.7.2 Results: Mechanical Properties

Figure 10 shows the representative stress-strain curve of an Octet truss lattice at 50% porosity. As can be seen, the compressive stress-strain curve can be divided into three main regions: linear elastic, plateau, and densification. Sample stiffness is obtained from the maximum value of stress-strain slope in the linear elastic region, and their yield strengths are obtained from 0.2% offset method. The results are presented in table 2.

The values of stiffness and yield strength are compared in Figure 8 for Tetrahedron and Octet trusses. For the Tetrahedron topology, stiffness and strength of the lattice samples decrease with increasing porosity. Octet truss shows similar decrease up to a design porosity of 70%, with no decrease in strength at 75% designed porosity. At a low designed porosity of 50%, the Octet truss is stronger and stiffer than the Tetrahedron. However, as the porosity increases, the trend reverses, with the strength and stiffness of the Tetrahedron much higher than that of the Octet truss.

The Gibson and Ashby power law equation is also used to correlate the experimental results to a closed form equation [34]. The constant and the power of the equation are obtained using a linear regression method. These equations can be used to predict the effective mechanical properties of the Tetrahedron and Octet truss as a function of relative density. As can be seen in Figure 11, the empirical equation correlates better for the Tetrahedron samples with (R^2>0.90) compared to Octet truss samples with (R^2<0.86).

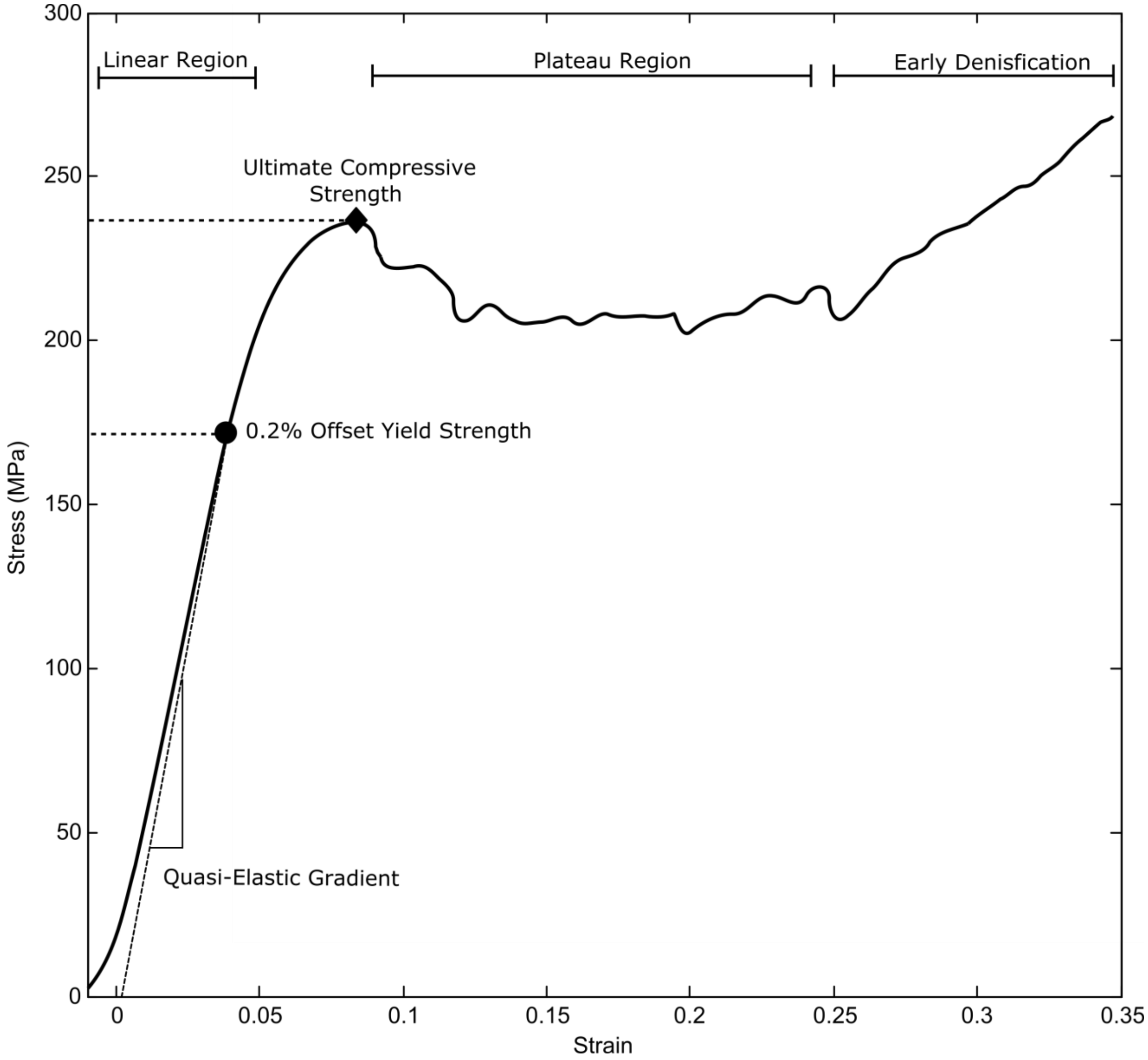

Figure 11: Compressive stress strain of a representative Octet truss at 50 % porosity. The graph shows a clear difference between the 0.2% offset yield strength and the ultimate compressive strength.

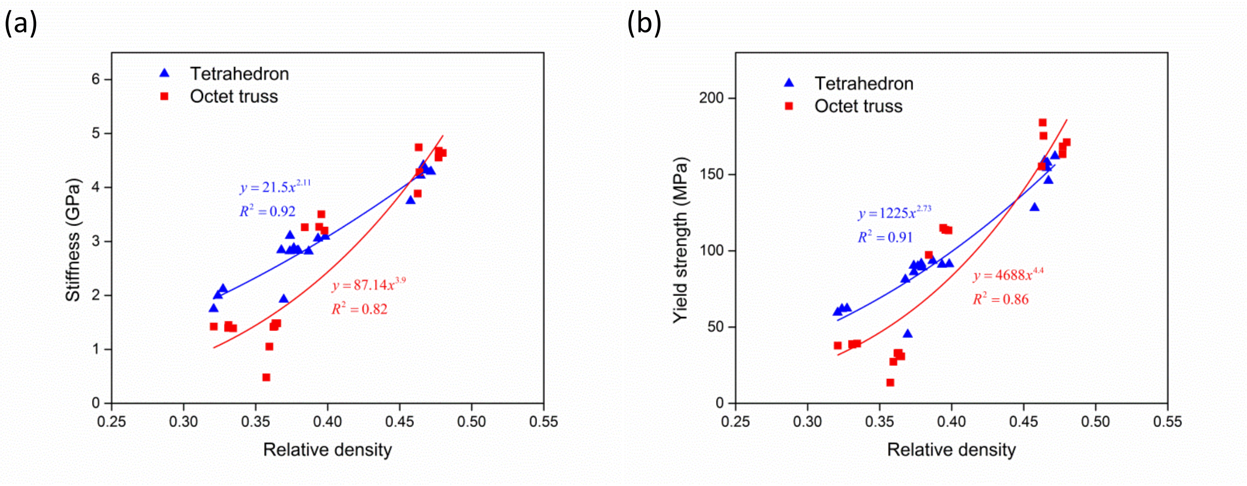

Figure 12: (a) The Young's-modulus and (b) the compressive yield strength of Tetrahedron and Octet truss lattice as a function of designed and measured porosity.

Table 2: Mechanical properties of Tetrahedron and Octet Truss samples

	Stiffness (GPa)			**0.2% Offset Strength (MPa)**			**First Maximum Strength (MPa)**		
Designed Porosity (%)	Tetrahedron	Octet Truss	P value	Tetrahedron	Octet Truss	P value	Tetrahedron	Octet Truss	P value
50	4.32± 0.07	4.58± 0.18	0.029	155.84± 6.19	172.49± 7.82	0.0063	219.47± 8.18	227.86± 10.15	0.19
60	3.11± 0.38	3.42± 0.28	0.18	98.59± 16.58	118.96± 21.59	0.14	135.52± 22.91	145.47± 33.83	0.6
70	2.89± 0.12	1.37± 0.18	1.20E-06	87.85± 4.23	30.96± 2.10	1.30E-07	119.61± 3.74	31.37± 2.19	2.50E-09
75	1.95± 0.15	1.23± 0.40	0.015	57.20± 8.13	33.58± 11.18	0.008	67.60± 3.40	39.27± 2.76	1.40E-05

3.7.3 Discussion: Mechanical Properties

For low density (high porosity) values, the mechanical properties of a cellular material can be predicted via the standard power law equations introduced by Gibson and Ashby [34]. With regards to property prediction, the effective stiffness and strength of stretch-dominated topologies scale as a function of $\bar{\rho}$ to the power of 1. On the other hand, the stiffness and the strength of a bend-dominated material are governed, respectively, by $\bar{\rho}^2$ and $\bar{\rho}^{1.5}$ [34, 85]. Upon mechanical testing of the Tetrahedron lattice, the stiffness is found to follow the power law of $\overline{\rho}^{2.1}$, whereas the stiffness of the Octet truss scales follow $\overline{\rho}^{3.9}$. Both power laws deviate from the Gibson and Ashby predictions, a discrepancy that is expected, as we are examining beyond the range in which those relations are valid. In addition, as discussed in the previous section, the manufacturing deviations can be on the order of the designed strut thickness features. As reported by Simone and Gibson [86], manufacturing defects result in local heterogeneities and stress concentrations that affect the yield strength of the sample. Manufacturing defects in porous structures would also affect the deformation modes through the entire specimen, thereby leading to an earlier failure of the struts and a reduction in stiffness and strength. A similar drop in stiffness and strength properties has been reported in the literature for porous samples manufactured with SLM and EBM [71, 87]. As shown in Figure 8, the Octet truss lattice at high porosity shows a sudden drop in mechanical properties. One cause can be attributed to the smaller average strut dimensions for the Octet truss samples at lower porosity. Previous studies indicated a dependency on strut thickness in addition to porosity, with thinner struts resulting in lower strength even at constant porosity [71]. The decrease in stiffness and strength, however, contrasts to the findings of Yen et al [88], who found that samples with equal porosity but larger cell size (and hence strut size) had decreased strength and stiffness. For both of the topologies tested in this paper, the strut thickness and porosity are equivalent. However, the strength of the Tetrahedron at high porosity (70% designed) is significantly higher (87.85±4.23 vs. 30.96±2.10 MPa, $P=1.3\times10^{-7}$). At high porosity, the stiffness of the Tetrahedron is also higher than that of the Octet truss (2.89±0.12 GPa vs. 1.37±0.18 GPa, $P=1.3\times10^{-6}$). This is in contrast to the lowest 50% porosity design where the Octet truss is both stronger and stiffer than the Tetrahedron. This drastic decrease in strength and stiffness at high porosity could be attributed to material agglomeration in the high porosity Octet truss cells. From CT images, the occlusion of some pores of the Tetrahedron elements surrounding the Octet truss is observed. In an Octet truss cell, the surrounding Tetrahedron pores are no longer void: a manufacturing outcome that could potentially lead to a change in the mechanism of deformation. The manufactured Octet truss sample is no longer dominated by strut stretching, rather a failure mode dominated by bending. While further study is required to substantiate this observation, the experimental data obtained in this work show that at high values of porosity and for strut thickness near the manufacturing limits, the Octet truss is more sensitive to manufacturing error than the Tetrahedron lattices.

Because of the interdependence of cell topology, strut thickness, cell size, porosity, and pore size, a comparison with the results in the literature is challenging. This explains why a diverse range of experimental design strategies exist in the literature. The design charts presented in this work can be used to assess the choices and merits of other studies existing in the literature on the subject. Van Bael et al. tested the cell response and compressive stiffness of a set of SLM lattice structures for high and low pore sizes (500 and 1000 microns), at a constant wall thickness of 200 microns [67]. Warnke et al. used a similar design with variable pore sizes ranging from 450 microns to 1200microns and a cubic cell topology [89]. This design, however, results in different porosities for each selected topology, making direct mechanical comparisons between topologies difficult. This experimental design can be visualized by moving along the lower wall thickness constraint of the design chart. In contrast, Yan et al. tested a single cell topology at constant density, with varying cell size and strut thickness in compression [88]. This design results in different pore sizes for each sample, and can be visualized by moving along a line of constant density on the design chart.

The design charts presented in this paper provide a systematic tool to visualize the whole design space and the relationship of porosity, strut thickness, and cell size with respect to mechanical properties and manufacturing limits. Future work is required to create response surfaces that estimate domain characterized by mechanical performance metrics, along with manufacturing and bone ingrowth limits.

3.8 Performance of Tetrahedron and Octet Truss Relative to Tantalum Foam

The *in vivo* canine study results are part of a complementary pilot study that aims to assess the biological performance of highly porous structural biomaterials with a stretch-dominated mechanical behavior: Octet truss and Tetrahedron based. The details of the study are beyond the scope of the thesis, and the investigative work is primarily completed by Jenny Ann Pura and Dr. Michael Tanzer as mentioned in the contributions. However the results are provided insofar as to contextualize the performance of the Octet Truss and Tetrahedron based materials presented herein to other porous biomaterials, namely trabecular metal (TM).

The primary goal is to determine if bone ingrowth occurs within stretch-dominated lattices manufactured with SLM. The Tetrahedron-based transcortical sample has a pore size and porosity of 438 and 55%, respectively, representing a point in the middle of the design space as detailed in section 3.4. The point selected for the Octet truss is close to the upper bound of the pore size in the feasible design space with pore size and porosity of 772 and 76%, respectively. The *in vivo* studies clearly demonstrate that bone ingrowth occurs in all implants in a reproducible and predictable fashion. Both topologies demonstrate early and extensive bone ingrowth by 4 weeks, averaging 29% and 36% for the Tetrahedron and Octet truss respectively. By 8 weeks' time, there is a further 41% and 58% increase in bone ingrowth for the Tetrahedron and Octet truss topologies. Four and six week canine studies have shown that the amount of bone ingrowth into porous coating varies between about 15% to 50% [90], while for TM, the amount of ingrowth is higher and increases from 13% in two week to 53% in four weeks [25]. The amount of bone ingrowth for Tetrahedron and Octet truss samples, which is in the range of other porous coatings and lower than TM. The amount of bone ingrowth is proportional to the porosity of sample. TM has porosity of 75 to 85%, significantly higher than the porosity of the transcortical implants manufactured for this study. This may be a contributing factor to the reduced amount of bone ingrowth in the high strength porous samples compared to TM.

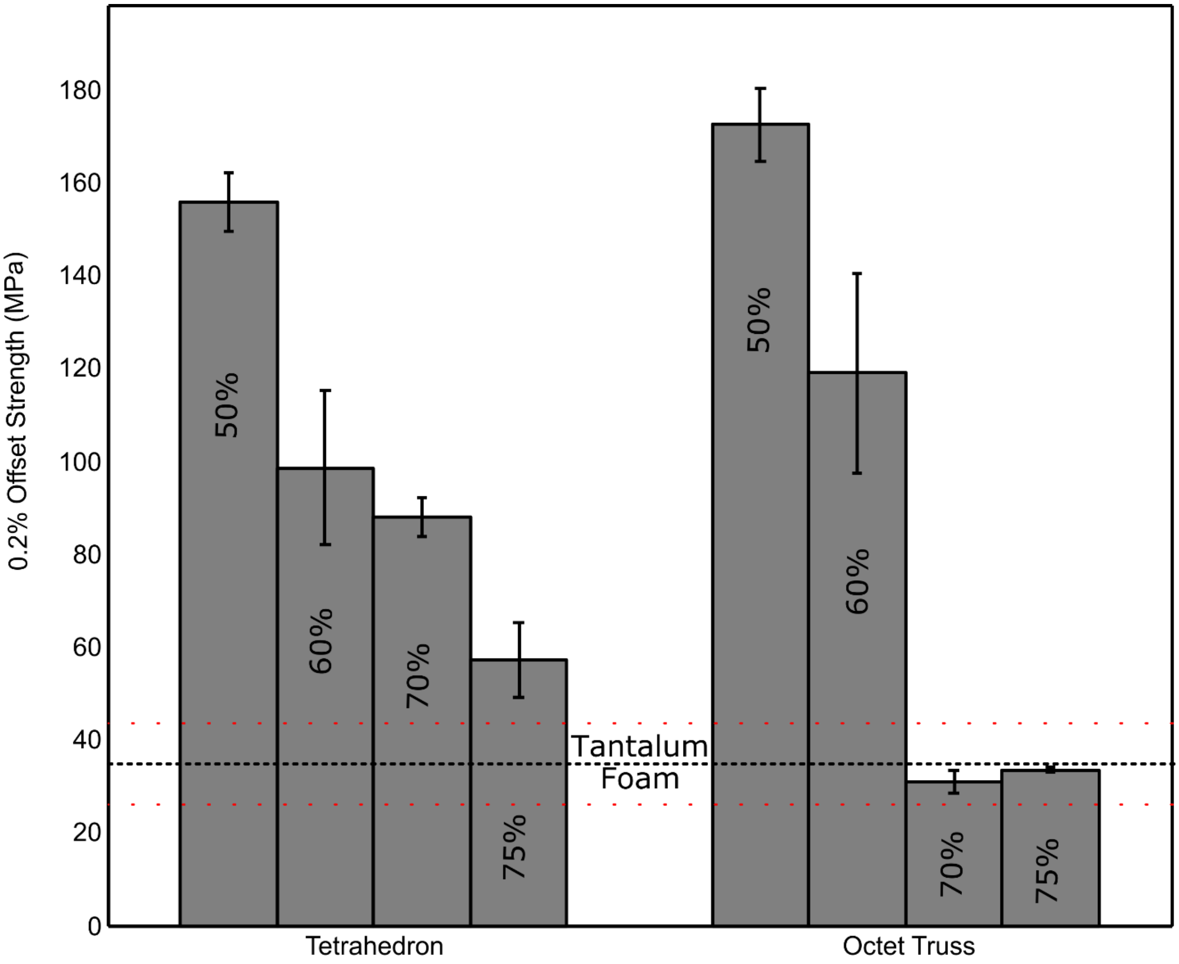

Figure 13: Mechanical strength of the tetrahedron and octet truss topologies at various porosities compared to tantalum foam [51].

One of the main advantages of the stretch dominated lattice samples compared to TM is their mechanical strength. Figure 12 shows that the strength of manufactured samples is significantly higher than that of TM. Furthermore, because these samples are manufactured with additive manufacturing, the porosity gradient can be tightly tailored to minimize stress shielding while maintaining sufficient strength. High- strength porous structures can be manufactured with an interface layer that has optimal pore size and porosity for bone ingrowth, whereas the internal microstructure can be designed to feature lower porosity, resulting in high mechanical strength to support physiological loadings. The bone ingrowth results are encouraging and require further corroboration to understand the impact of cell topology, pore size and porosity on bone ingrowth.

Chapter 4: Functional Application to a Hip Replacement

As discussed in chapter two, a total hip arthroplasty (THA) is used to replace a damaged hip joint with a mechanical analog to restore motion and alleviate discomfort. THA is commonly used to treat osteoarthritis, a condition that can cause significant pain and leads to drastically reduced mobility, or trauma, among other indications. The joint is replaced with an artificial femoral stem and femoral head that interfaces with an acetabular cup component to function as a ball and socket joint. Due to the degree of relief provided to the patient and the relatively low complications associated with the procedure, it has been heralded as one of the most successful medical interventions.

Despite the success of THA, there remain several alarming complications. One of the main complications after a THA is aseptic loosening of the implant. Various mechanisms for aseptic loosening have been proposed including: bone resorption secondary to stress shielding [91], excessive micro-motion of the stem as a result of primary instability [19, 92], excessive local stress at the bone-implant interface [93], formation of wear debris-induced osteolysis [94, 95], high fluid pressure at the joint [96, 97], endotoxin [98, 99], non-sealed interface of bone and implant [100, 101] and individual or genetic patient variations [102]. The problem of bone resorption secondary to stress shielding is particularly intriguing since it is dependent on the implant's stiffness. It can therefore be addressed through using fully porous biomaterials to tune the implants such that it is mechanically biocompatible with the host bone.

4.1 Stress Shielding in Total Hip Replacements

The origin of bone resorption in bone-replacement implants arises from the mechanical mismatch between femoral bone and implant. Materials currently used in hip implants, including 316L stainless steel, cobalt chromium alloys, and titanium-based alloys have stiffness considerably higher than that of bone. The elastic moduli of bone vary in magnitude from 4 to 30 GPa depending on the type of the bone and the direction of measurement [103]. However, the values of Young's modulus of chromium and titanium alloys are 220 and 110 GPa respectively, which are almost one order of magnitude higher than that of bone. Once a metal implant is implanted within the bone, the majority of load will be transferred to the implant and away from the surrounding bone due to its high stiffness. This leads to the bone being under-loaded compared to its natural state. As a result bone, a living tissue that is sensitive to mechano-transduction, will start to lose mass by an adaptive process known as bone remodeling [104, 105]. This phenomenon is usually referred to as stress shielding effect [91, 106].

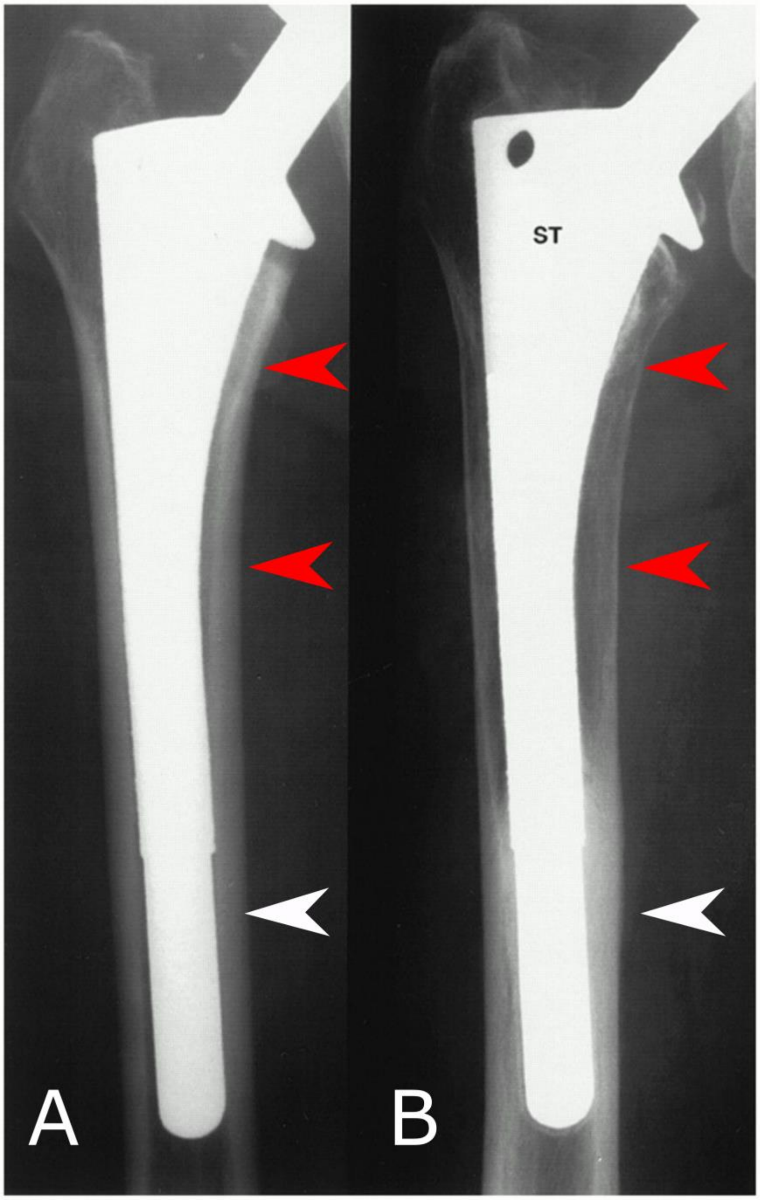

Figure 14: Reduced intensity on radiograph surrounding the implant at right (B) shows reduction in bone stock medially at the red arrows [107].

The reduction in bone stock can lead to serious complications, such as aseptic loosening or peri-prosthetic fracture [108]. As a secondary effect, even if there are no direct complications, as a result of the reduction in bone quality from stress shielding, stress shielding significantly increases the risk of a revision surgery, should one be required due to other implant failures such as articular wear. Both the long term performance and the safety of revision surgeries are a growing concern since the average life expectancy is increasing, and patients are receiving THAs at younger ages. Meaning the predicted number of revision surgeries is predicted to rise drastically [109].

Many studies have been performed to reduce stress shielding effect. Since stress shielding is contingent upon the implant's stiffness, these attempts sensibly fall into either the modification of the geometrical profile, or the modification of the material properties, or a combination of the two. Geometrical modifications include changing the geometry of stem through modifying its cross section profile [110], decreasing stem length [111, 112], creating taper and curvature along the femoral stem [113], adding collar or anchoring attachment at the proximal portion of the stem [111, 114], and designing a stem with hollow structure and internal grooves [115]. These modifications all serve to effectively lower the area moment of inertia of the implant to reduce its bending stiffness. Whereas modifications of material properties include stems with functionally graded materials, composite structures such as the VerSys Epoch® (Zimmer, Warsaw, IN) that has a solid metallic core surrounded by a low modulus polymer and a titanium fiber mesh coating to achieve bone ingrowth[116, 117], or cellular materials fabricated through EBM with uniform porous cellular structure [118].

4.2 Implant Design and Tuning Process for Optimal Material Distribution

Recently, we have introduced a microarchitectured high strength fully porous biomaterial fabricated through Selective Laser Melting (SLM) for load bearing orthopedic applications [119]. The hallmark of this material is the controlled topology, porosity, pore shape and size, interconnectivity to allow for early and extensive bony ingrowth for implant osseointegration, along with superior strength for the load bearing requirements of orthopedic implants. This technique allows for a combination of graded material and morphological properties, gradients in pore size and porosity to achieve a reduction in stiffness to embody optimized graded material properties to reduce stress shielding while respecting bone ingrowth and manufacturing requirements [120, 121]. Previous work has shown the proof of concept for using graded cellular materials to fabricate an optimal design for reduction of stress shielding [63].

This thesis serves to bridge the gap between theoretical distribution of optimal parameters, embodiment of the optimal solution through cellular materials, and in-vitro evaluation of the proposed performance through the design of an optimal 3D fully porous hip implant with a minimally invasive geometry. To demonstrate the potential to minimize bone loss via material microarchitecture tailoring in porous hip implants, an experimental investigation has been undertaken. Previous work within the group created a high fidelity physiological finite element model of an implanted human femur. This model was used to both determine an optimum design, as well to quantify the reduction in stress shielding that could be expected from a tuned fully porous hip implant. The resulting material distribution from the optimization is used to embody and manufacture the implant respecting the design space limitations addressed in the previous chapter. An in-vitro experiment is used to compare the performance of the fabricated optimal implant relative to a solid control in composite femora. Both the intact and implanted femurs are loaded in a quasi-physiological loading state to measure surface strain using Digital Image Correlation (DIC). The change of strain between intact and implanted femur is used as a proxy for stress shielding. The experimental model is not intended to serve as a direct validation of the physiological FEA model, but rather as separate complementary investigation.

The design process of the total joint replacement is a development founded on previous work and is based upon an integration of a multiscale mechanics approach and an optimization strategy to deal with the scale-dependent material structure, and to optimize the graded property distribution for minimum bone resorption. The main steps of design and optimization consist of : A finite element model of the bone implant system from CT-scan data with material properties based on the Houndsfield intensity of the voxel [122] with the effective elastic moduli of bone obtained through the relation proposed by Wirtz et al. [123]. The system is modeled in physiological single stance phase of the gait cycle [124]. The porosity of the lattice material constituting the hip replacement is allowed to vary, and based on an NSGA II algorithm a porosity distribution that minimizes bone resorption is found. Although the method could be extended to create patient specific implants with a specific tailored properties, especially due to the flexibility of manufacturing using SLM, there remain several key challenges such as computational time and regulatory approval. As such, the optimum material property distribution determined with the computational model is used for the benchmark implant.

4.3 Experimental Design Rationale

To assess the performance of the tuned fully porous implant it was tested in an in-vitro biomechanical model. A commercially available a fully solid stem was used as a control to allow for a comparative analysis. The biomechanical model was based on assessing the reduction in cortical strain on a femur in both its intact natural state, and after implantation with a femoral prosthesis. This approach has been widely used in the literature to assess biomechanical performance for orthopedic implants, with a variety of loading conditions and strain measurement techniques [125, 126].

To discuss the loading set up for the investigation undertaken, it is important to understand the complexity of the physiological loading that the femur experiences during every day activities. The study of biomechanics is inherently challenging because of the over constrained actuation of the skeletal system from various muscles, at various insertion locations. The femur alone interacts with 17 muscles [127]. The complex interaction of these muscles is what allows for a wide range of nearly seamless flexion, extension, and rotation of the joints. As elucidated in an earlier section, this contributes to loads that are significantly higher than simply the bodyweight above the joint from the actuation to balance moments. This can be further complicated by variations in muscle strength, and recruitment from neuromuscular control in addition to the effect of any neurological pathologies or injuries that can alter the local loading state. The refinement and analysis of the femoral loading remains an important topic of significant research within the biomechanical community.

Despite the complexity of the biomechanics involving the hip, in-vitro biomechanical models are critical for evaluating the efficacy and safety of new joint arthroplasties. In these in-vitro models, the natural physiological loading state is simplified to varying degrees. Although absolute properties, such as micro motion, can be measured using a standardized model for stair climbing, there is no consensus about the optimal loading condition for analyzing changes in strain or stress on the proximal femora[126]. Rather, it is instead important to compare the relative changes in strain relative to an existing implant. As such, a simplified loading phase describing single leg stance with only acetabular forces was chosen in this investigation in order to minimize variance and limit confounding factors for changes in the proximal strain distribution.

Six large left adult artificial femurs (Model 3406, Sawbones, Vashon, WA) were used. The composite femurs are anatomically consistent with a human femur. They consist of a glass fiber and epoxy resin to simulate the cortical bone, and a polyurethane foam core to represent the cancellous bone. Composite femurs have been shown to have similar biomechanical behavior to fresh cadaver specimens during loading [128]. Additionally, composite femurs show very low inter-specimen variability relative to cadaver femurs. Namely, their geometry and material properties are nearly identical to one another, within tolerances of injection modeling processes which are orders of magnitude lower than anatomical variations. Additionally, their properties are not dependent upon parameters, such as storage method, humidity, time from harvest, factors that can substantially alter the properties of cadaver bone [129]. This minimized variability is advantageous for the current study, as it allows for a direct comparison of a solid implant relative to a fully porous implant, eliminating confounding factors. Additional advantages of the composite bones relative to cadaver specimens are numerous including: consistent material properties, availability, non-biohazard, and cost.

4.4 Assessment of Implant Size

The Trilock implant is designed to achieve metaphyseal contact with the cortical bone to transmit load to the proximal femur [130]. To recreate the intended loading condition, the choice of the correct implant size is imperative. Another critical parameter is the recovering of the appropriate neck offset. In an operative situation, this is important to restore the range of motion as accurately as possible, and to achieve proper leg length to avoid discrepancies that can negatively impact gait. It is also very important for any biomechanical study, since it affects the moment arm of the applied acetabular force. If the femoral neck offset is reduced after implantation, it leads to an overall lower strain on the proximal femur due to the decreased moment, and conversely, if the offset is too large, it will underestimate the effect of stress shielding. Studies that do not account for variations of femoral neck offset can be very misleading, because the change in strain is a result of the offset, as opposed to the implant being analyzed [131].

To account for the factors described above, all femurs were radiographed in the anterior posterior direction so as to determine neck offset and stem sizing. The neck offset was measured in a three step process that is widely used for radiological analysis [132]. The first step consists of measuring the width of the proximal femoral canal at two locations, and marking the center point of the canal at two levels. The two points are then connected to serve as the centerline of the femoral axis. Next, the center of the femoral head is marked by means of fitting a template circle to the intact femoral head. Finally, a line is drawn orthogonally from the femoral axis to the marked center of the femoral head. The distance along this line from the center of the femoral head to the centerline of the femoral shaft is the effective neck offset. The implant size was selected based on operative templates provided by Depuy Synthes (Warsaw, IN) and the judgment of an experienced orthopedic surgeon and chosen to be a size 6. To confirm the implant size, the femur was broached with progressively larger rasps until the size six rasp was seated. Another radiograph was taken, with the rasp left in the femur. Both medial and lateral contact between the rasp and the cortical bone was observed, indicating that the size was appropriate. Once the implant size was determined, the neck offset and femoral head component could be appropriately selected from the sizing information provided by Depuy. The implant size was determined as size 6 implant with an extended neck offset (HI) with a +5 offset 32 mm diameter femoral head.

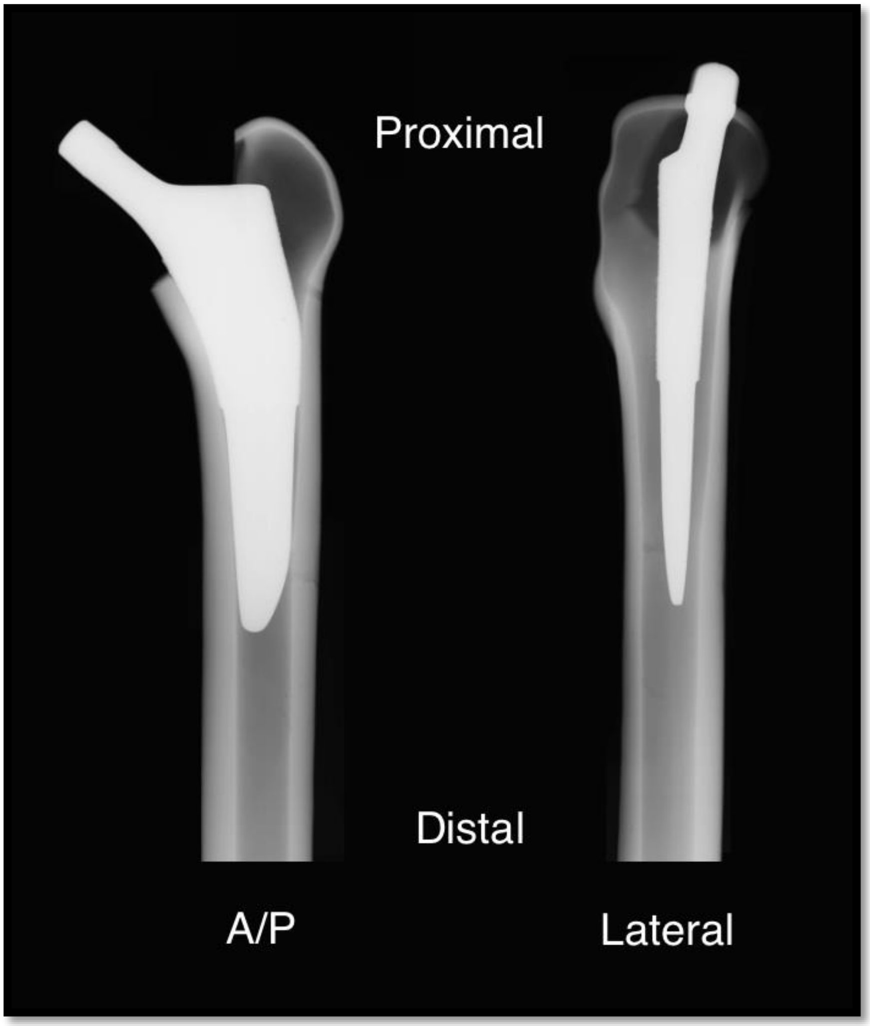

Figure 15: Anterior Posterior and Medial Lateral Radiograph showing the proper implant fit.

4.5 Implant Design and Manufacturing

Once the appropriate implant size was determined, a size 6 HI offset Trilock stem was obtained from Depuy. To effectively examine the effects of a fully porous microarchitecture, the implant macroscopic geometry should be prescribed. To accurately model the macroscopic design of the implant, a Depuy stem was 3D-scanned using an Arctec Spider (Palo Alto, CA) scanner. The scanning generated a point cloud of the implants surface with accuracy of 50 microns. Solidworks was used to create a CAD model from the point cloud information. The solid model was then aperiodically tessellated with a tetrahedron topology, similar to the tetrahedron topology described in chapter 3. The density distribution obtained from the optimization was mapped to the size 6 implant. On the proximal bone interfacing surface of the implant, the unit cell size was constrained to 1.6 mm with wall thickness of 300 microns, as gathered from the design charts presented in chapter 3. This choice resulted in a porosity of 70% and pore size of 500 microns, equivalent to the transcortical implants in chapter 3 that showed early and extensive ingrowth. Although no ingrowth is modeled in the in-vitro analysis, the implant tested should have features as close as possible to those that would be implanted in-vivo. The bone implant interface surface with high porosity was imposed for a depth of 500 microns within the implant design domain. The distal portion of the implant had the largest possible cell size to allow for powder evacuation, and a 200 micron skin encapsulating the distal region. This skin is again a feature that would be used for an in-vivo model to reduce distal ingrowth, which has been shown to increase stress shielding for implants with total porous coating [133, 134]. Throughout the rest of the implant, the cell size and thickness were allowed to vary to meet the optimized density distribution while respecting manufacturing limitations of 200 micron minimum strut thickness. An ellipse relief and threaded inserter were added to the fully porous implant to allow it to interface with the existing Depuy surgical instrumentation. This enables the surgeon to place the fully porous implant with identical operative equipment and technique, eliminating a potential source of variability.

In order to embody the optimum material distribution as determined from the optimization the relative density of each tetrahedron lattice is obtained from the average of relative density over the lattice using Gauss quadrature integration technique with one Gauss point.

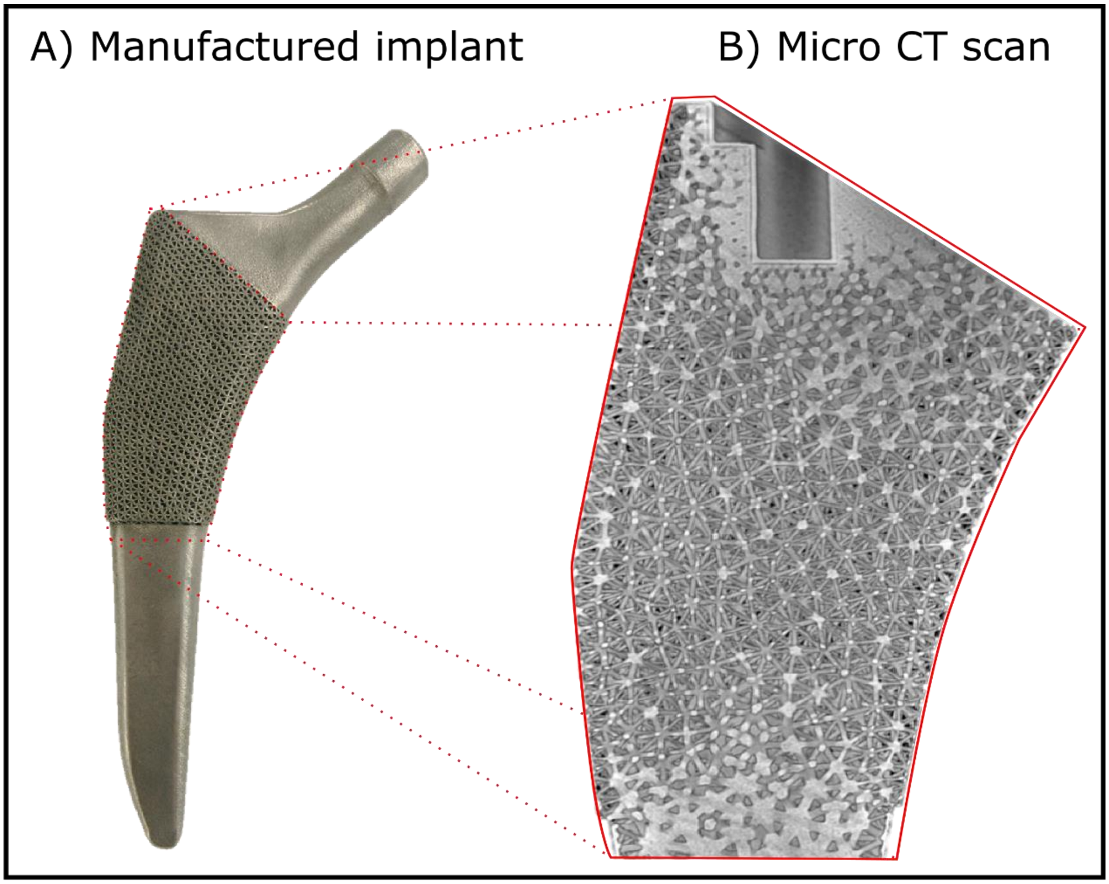

Figure 16: A) SLM manufactured fully porous hip replacement. B) CT cross section of the proximal portion of the fully porous hip replacement implant. The reduced cell size at the medial and lateral border of the image shows the interface for bone ingrowth.

The lattice structure is then reconstructed by remapping its relative density to the interior microstructure of the lattice. The samples are produced using the SLM process by the Renishaw AM250 with a power of 200 W and a laser spot diameter of 70 µm. The powder size is between 15-55 µm, and the powder layer of 30 µm is used, and a 2 hr heat treatment under argon. The parameters used are identical to those used the investigation of the preceding chapter.

4.6 Experimental Methods

To assess the change in strain between an intact femur and a femur with an implanted prosthesis, the loading was divided into two phases: the intact phase, and the implanted phase. Before loading took place, the femurs were prepared and mounted in the testing jig, and the implant surface was prepared for digital image correlation (DIC). The experimental processing and set up are described below.

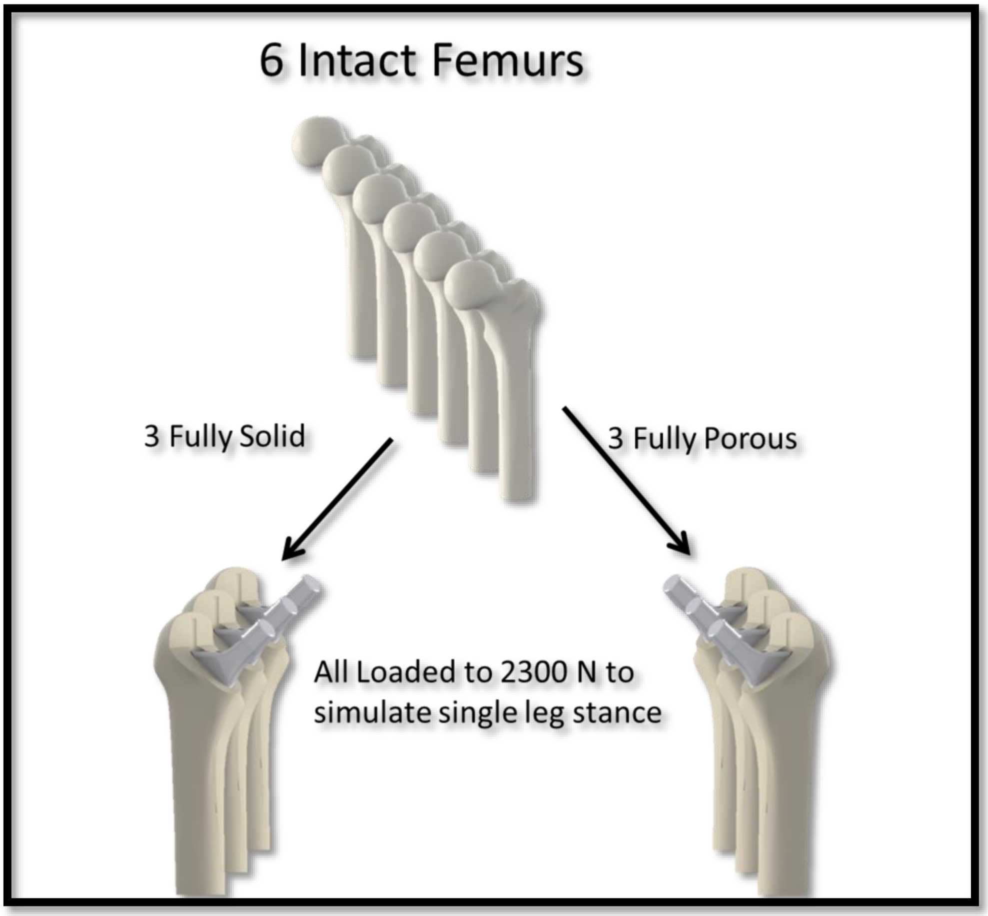

Figure 17: Schematic representation of experimental set up.

4.6.1 Femoral Potting

All femoral condyles were resected at a distance of 22 cm measured from the tip of the greater trochanter. Using a customized stand, the femurs where angled in 12 degress flexion, and 12 degrees adduction, as measured by a plumb weight and goniometer. Using Suprastone (Kerr Group, Charlotte, NC) dental cement, a mold of the distal femur was created to serve as a supplement to the angle measurement. This choice ensured consistency in the femoral orientation and positioning. The distal segment of the femurs was cleaned with 70% isopropyl alcohol and lowered into the center of a 10.2 cm diameter polyethylene container. The femur was lowered into the container until the distal aspect of the femur was 13mm from the base of the container, and positioned such that the center of the femoral shaft corresponded with the center of the container. A total of 350 ml of epoxy (3M, Saint Paul, MN) was then added to the container in two phases. For the first phase an initial volume of 250 ml was added to stabilize the femur. After one hour the second phase consisted of an additional 100 ml. For both phases the mixtures consisted of a ratio of 80:1 resin to hardener. The process was conducted in two distinct phases in order to avoid cracking of the epoxy layer, which can occur if the layer thickness is greater than 25.4 mm due to the exothermic effect of polymerization. The construct was allowed to harden for at least 24 hours. The process was repeated for all six femurs.

4.6.2 Femoral Painting

DIC relies on the contrast between speckles and the surrounding surface in order to correlate the motion and deformation of the surface and calculate the strain [135]. The manufactured color of the femurs is a dark brown that does not provide sufficient contrast for either black or white speckle patterns. As such, a base coating of white aerosol paint was applied in 3 layers, with particular care to provide a consistent finish on the medial calcar of the femur. A black speckle pattern was then applied to the femoral surface with speckles ranging from 500-1000 microns by means of sputtering aerosol paint. For DIC, the best correlations can be obtained when the ratio of speckles to background is roughly 50%. After speckling, any areas without sufficient speckle density had individual speckles added by hand, especially in areas of high curvature to avoid aerosol speckle streaking.

4.6.3 Image Acquisition and Calibration

A stereo mounted camera set up was used to acquire synchronized images of the medial calcar covering Gruen zones four through seven (Figure 20). The cameras where mounted in a vertically stacked position to increase the mutual information available for DIC analysis. The cameras used where 5MP monochrome grasshopper cameras (Point Grey, Richmond BC) with digital synchronization. They both had identical 35 mm focal length c-mount Fujinon lenses (Lebanon, NH). The cameras where positioned 30 cm away from the sample, with a 30 degree angle separating the cameras.

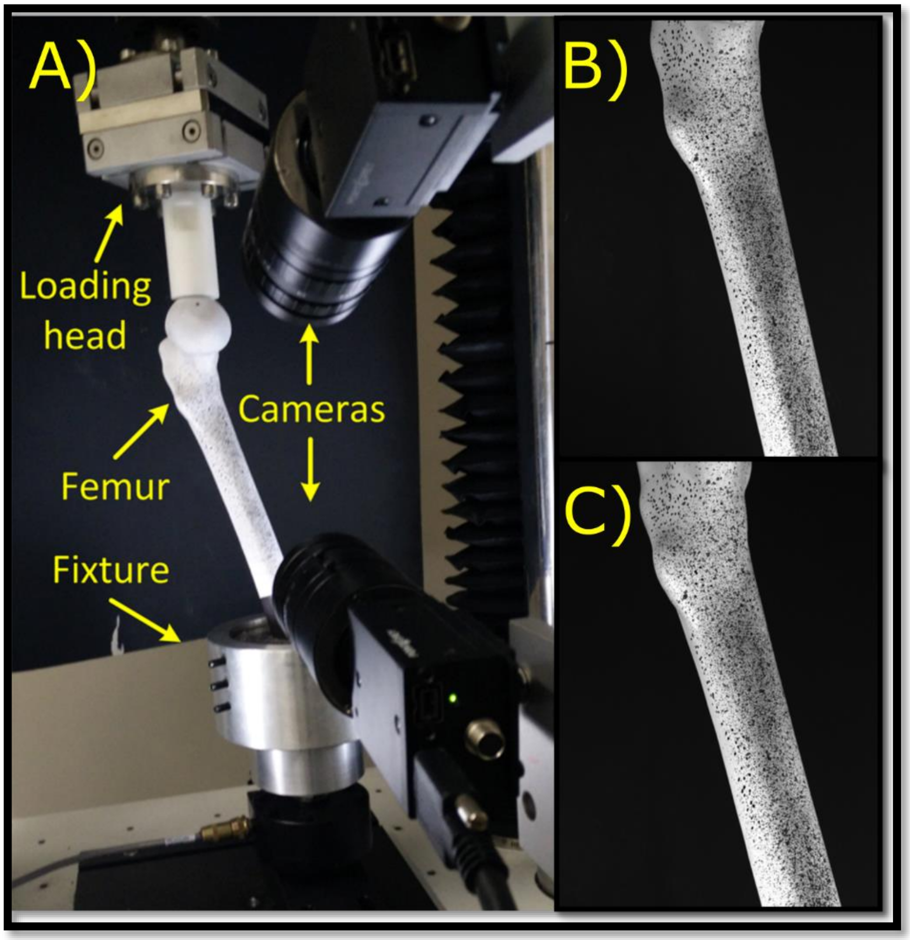

Figure 18: A) Experimental DIC set up, with loading head, femur, fixture and stereoscopic cameras. B) View of upper camera. C) View of lower camera.

The cameras were mounted on a t-extrusion fixture connected to the load frame to ensure consistent images, and the focus and aperture locked through means of a manual screw. Ambient lighting in addition to a twin goose neck lamp was used to provide sufficient illumination. Synchronized images where taken at a frequency of 15Hz starting 0.5 seconds before the load cycle, and lasting for the duration of the loading cycle.

Calibration was performed using a 9X12 circular pattern with 9 mm spacing using a grid generated by VIC 3d. This grid size was chosen to fill up the majority of the field of view in order to provide the best calibration for the system. Despite the rigid camera fixation to the load frame, the calibrations where repeated when the implanted femurs where analyzed in order to avoid the possibility of camera movement after the femurs where removed from the load set up to be prepared for implantation.

4.6.4 Loading

The prepared femur was inserted into a customized fixture that held the potted distal portion of the femur. A customized fixture that allowed for transmission of axial forces, but was free to translate in the transverse plane, applied a load of 2300 N to the femoral head at a rate of 200 Newtons per second, with a 2 second dwell at 2300N, and then returning to the unloaded state. 2300 N represents approximately 300% bodyweight (BW) of an average male which is expected to be translated through the acetabulum during single leg stance. The translating loading fixture served two purposes: firstly, to self-center on the femoral head, and secondly to prevent physiological moments during loading while the natural flexion of the femoral shaft was allowed. The force actuation was conducted on a Bose 3510 Electroforce fatigue tester (Eden Prairie, MN), with force measurements taken from a 12.5 KN load cell sampling at 200 Hz.

4.6.5 Experimental Sequence

Phase one consisted of loading the intact femurs following the preparation previously described and loading sequence. After the loading procedure was applied, the femurs were then removed from the loading jig. From the pre-operative template measurements, the femurs where marked at a height of 7mm from the lesser trochanter, and the femoral head resected by an experienced surgeon. The femurs were then inserted into another jig to stabilize them for implantation. The femurs were oriented in a manner similar to the exposure that would be gained through an anterior approach. This choice allows a gross replication of the intraoperative position in order to maintain consistency in surgical approach for the surgeon. The canal was broached and successively reamed using standard operative equipment supplied by Depuy. After preparation, the femur received either a fully porous, or a solid control femoral stem implant.

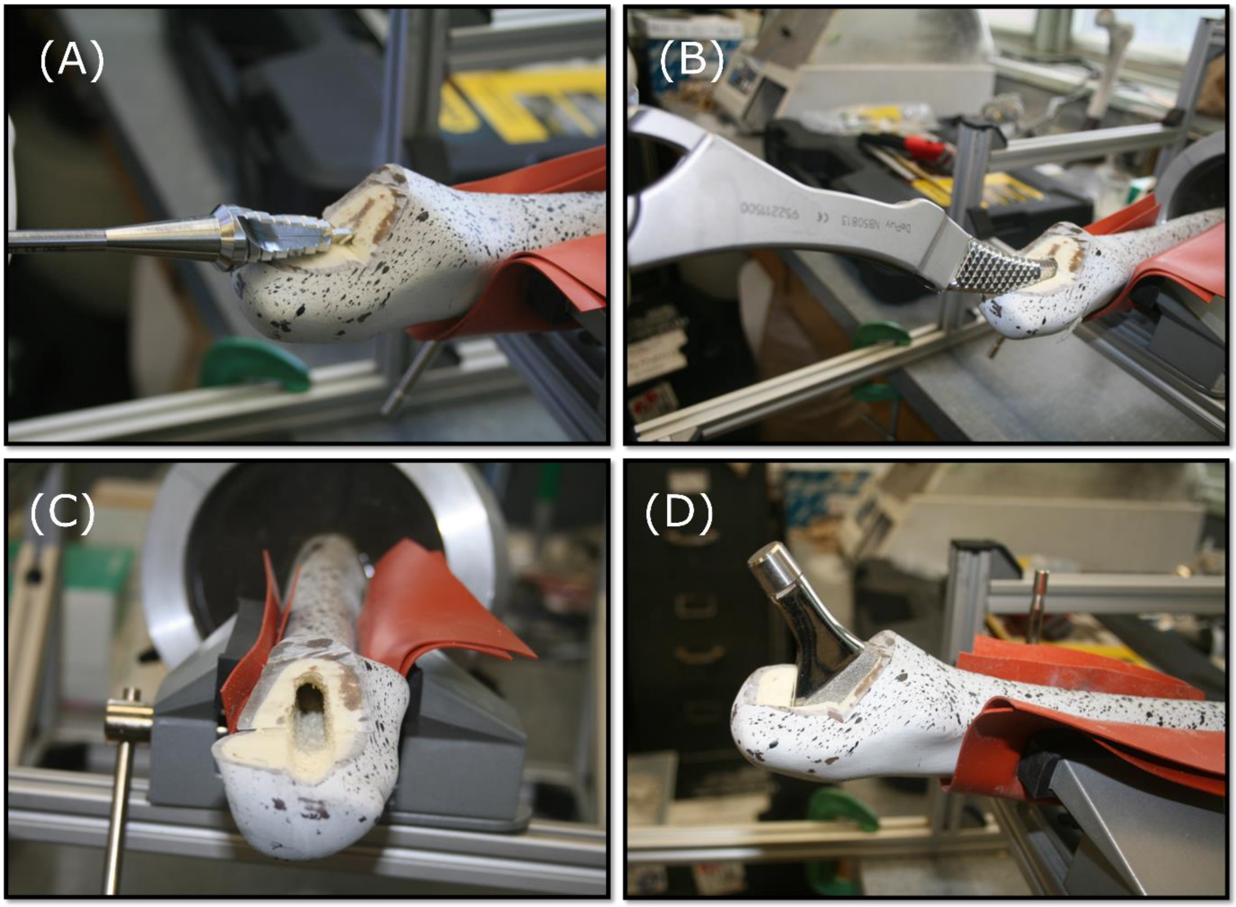

Figure 19: Insertion of the femoral components: A) Removing excess bone at the greater trochanter to avoid varus stem position. B) The femur is broached with successive rasps up to size 6. C) Prepared canal shows proper anteversion. D) Stem after implantation.

Due to the substantial physical effort required to implant the femurs, the implantations were conducted in pairs, with one femur receiving a fully porous stem and the other a fully solid control stem. An Anterior-Posterior (AP) and Medial-Lateral (ML) projection radiograph were taken to ensure consistent implant position, and correct the length of the neck offset. The implanted femurs were mounted in the same loading jig, and loading and image acquisition procedure repeated.

4.7 Experimental Processing

The use of DIC with a registration to an atlas femur was a key contribution of this work. It allows for a much finer and accurate assessment of changes of strain compared to existing methodologies that rely on an approximately placed physical or virtual strain gauge. Further details in comparison to existing methods for examining changes in surface strain is provided in section 4.9.3. There are two distinct levels of averaging to arrive at the final results for strain shielding. The first is a temporal average for each femur analyzed during the 2300N load application at every subset. The average subset value for each femur is then registered to an atlas femur, so that the compressive strain post implantation can be compared to the compressive strain pre implantation for each femur. This allows for the calculation of strain shielding in each femur, as segregated by the Gruen zone. Section 4.7.1 details how the measured strain shielding is calculated and used as a proxy for stress shielding. The average strain shielding of each Gruen zone can subsequently be calculated for each treatment arm (fully porous implant or control fully solid implant). The details of the procedure are elaborated below.

VIC3D (Correlated Solutions, Irmo, SC) was used to run the digital image correlation on the obtained data sets. To process the images, an oversized rectangular Area of Interest AOI was drawn around the complete femur to extract all possible data, and a subset size of 20 pixels, with a 5 pixel step, was used with a strain smoothing filter of 15 pixels. The correlation was run for all images within the sequence. Because the investigation was looking at the loaded state of the femur, the images during the 2300N loading plateau were selected and exported to Matlab for further processing. The data obtained during loading were not used for further analysis.

Within Matlab, the exported data files provided the position and strain for each subset in the DIC analysis. The average principle compressive strain and standard deviation was calculated for each subset over the images obtained during the fully loaded phase of the gait cycle for each femur. If a subset within any image deviated by more than three standard deviations from the mean, it was removed from the data set, and the average recalculated. This represents a temporal average of principle strain for each subset, of each femur tested. For further processing the data were reformatted into a rich point cloud (RPC). The RPC consisted of a cloud of points with xyz coordinates of the subsets, along with their corresponding average values of principle compressive strain.

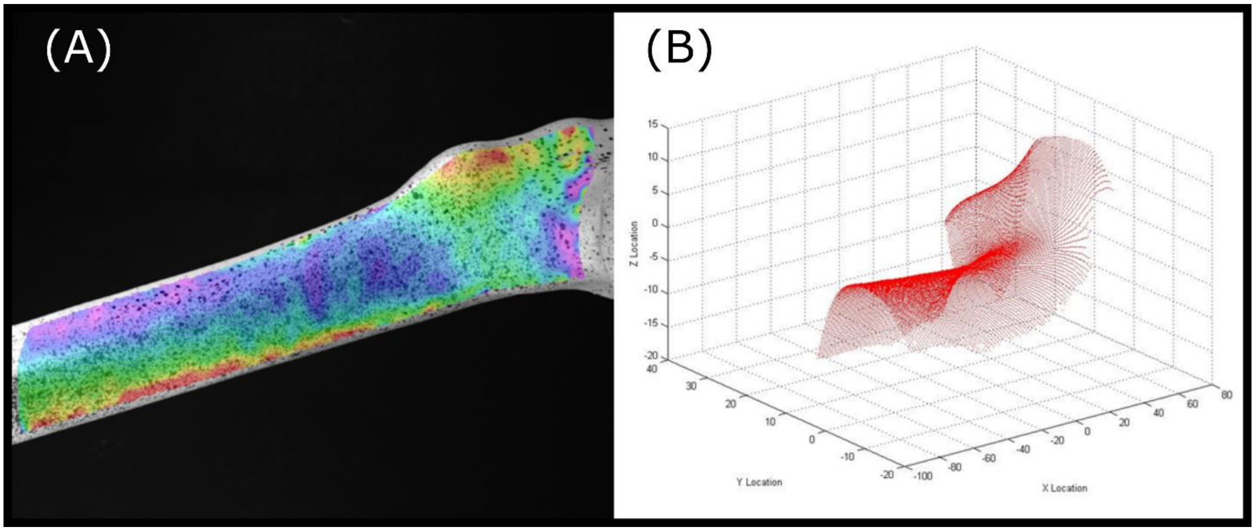

Figure 20: A) DIC results in VIC 3D. B) Native DIC data exported to Matlab to create a rich point cloud for registration to an atlas femur for further analysis.

To ensure consistent positioning of the data, the RPC was registered to an atlas reference of the composite femur. This was achieved through means of a rigid body registration using an iterative closest point method with KD Tree logic and plane minimization to improve accuracy[136]. The results of the registration were manually inspected to ensure that registration was appropriate. The registration of the data set to a reference femur insured that the local strain measurement was consistently anatomically located. A 20 pixel subset with a five pixels step size is used with a pixel size of approximately 100 microns. This corresponds to a grid of data points along the surface of the medial calcar spaced approximately 500 microns apart. The registration procedure of each data set to the reference femur atlas provides a consistent reference for comparison between each treatment group.

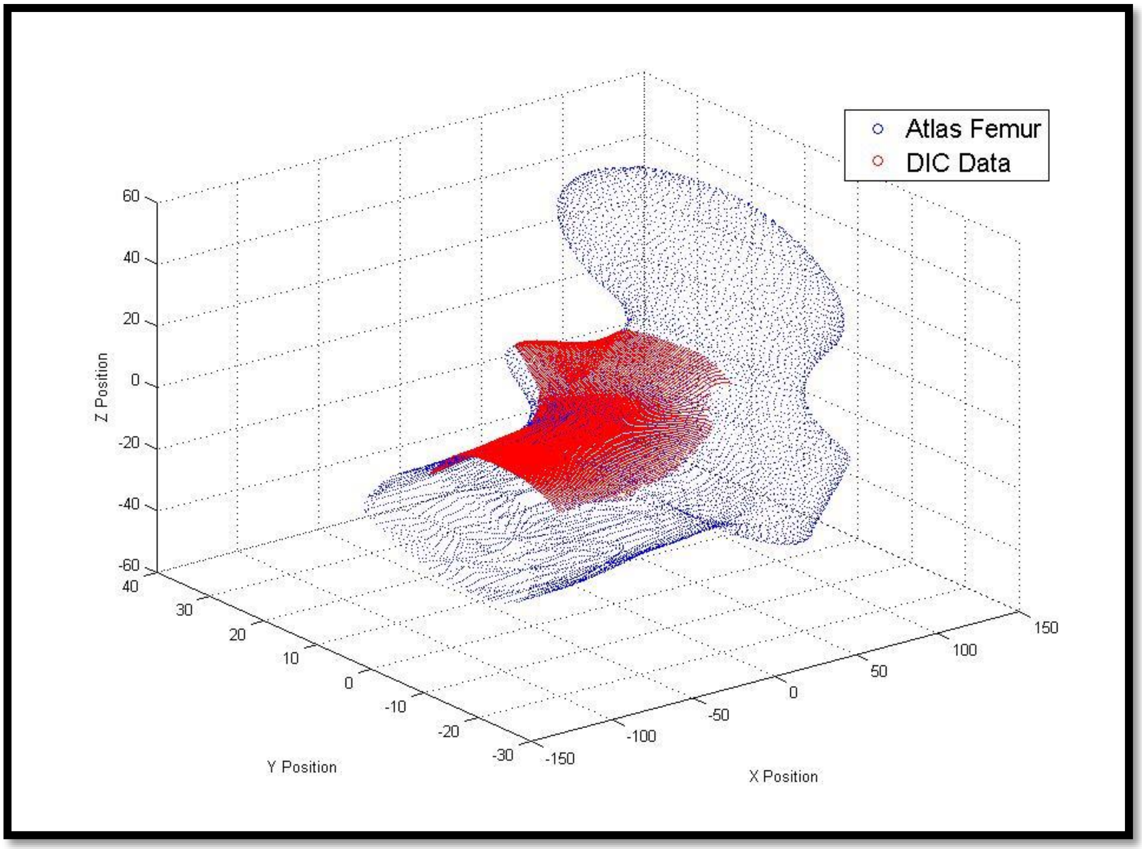

Figure 21: RPC (red) registered to the atlas femur (blue). This ensures consistent anatomical position for strain measurements.

4.7.1 Quantifying Bone Susceptible to Resorption

After registration, the strain of the intact femur and the implant femur can be accurately compared. Due to the complex geometry of the medial calcar, there are variations of strain along the surface. The registration of the data set to an atlas reference effectively eliminates position errors during comparison. The reduction in principle compressive strain is calculated as the strain after implantation divided by the strain of the intact femur. This can be graphically visualized along the surface of the femur by means of a contour plot. For quantitative evaluation, the medial calcar was divided into the standardized Gruen zones 7, 6, and 5, with the edges excluded due to the increased noise from subsets that are more than 15 degrees out of the plane of the camera. If the reduction of strain after implantation was greater than 50% relative to the intact femur, the subset was deemed to be prone to bone resorption. The percentage of subsets within each zone susceptible to resorption was calculated for each Gruen zone, and for each of the individual femurs. The percentage of bone susceptible to bone resorption was calculated for each femora. The average percentage of bone susceptible to resorption was calculated from the three replicates of each treatment. The results are shown in table 3. To compare the performance of the implant type, each Gruen zone was compared using an unpaired student t-test with unequal variance, with statistical significance set at P<0.05.

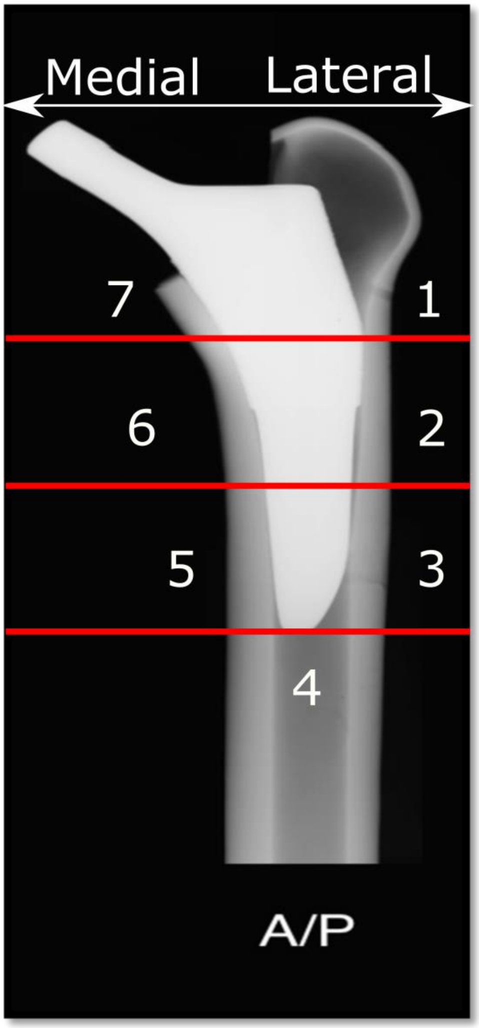

Figure 22: Gruen zones to assess the area of bone susceptible to resorption.

4.8 In-vitro Performance Evaluation Results

Radiographic evaluation showed good fit and alignment of all implants within the femoral metaphysis, with contact on the cortical bone both medially and laterally. Additionally, the implant axis was in-line with the femoral axis indicating no varus or valgus positioning error. Because of the correct placement, no femoral models were discarded from analysis in the study. All implanted femurs showed a reduction of strain compared to the intact femur in the proximal section of the femur. Visually, a composite average of all femurs for both groups' shows that the extent of strain shielding extends further distally on the intact femur compared to the intact femur.

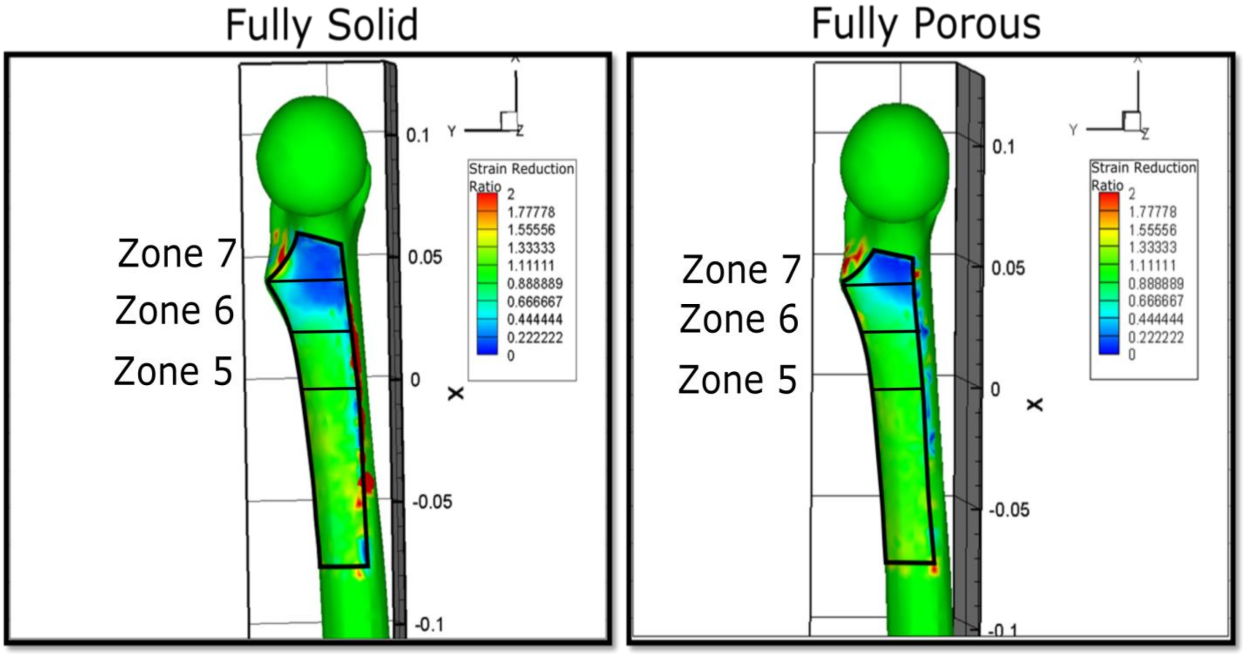

Figure 23: Average change in strain post implantation of all femurs when loaded to 2300 N. The distal portion of the stem shows no variation in strain indicating that the neck offset was maintained and the comparison is valid.

Distal to the implant there is no significant difference in the strain between the intact and implanted femur for both implants. This indicates that the neck offset was appropriately established after implantation, indicating that the loading set up was valid for a comparison. Gruen zone 6 showed a statistically significant reduction in strain shielding in the fully porous implant as compared to the fully dense implant (24.1±4.9% vs. 7.4±7.0% $P < 0.05$). Gruen zone 5 and 7 showed no statistically significant differences. Gruen zone 7 showed the highest extent of strain shielding for both implants, 69.8±23.9% for the fully solid implant and 70.9±13.5% for the fully porous implant (P>0.05). Gruen zone 5 experienced the least for both implants tested, 6.8±9.9% and 2.2±3.2% for the fully solid and fully porous implants respectively (P>0.05).

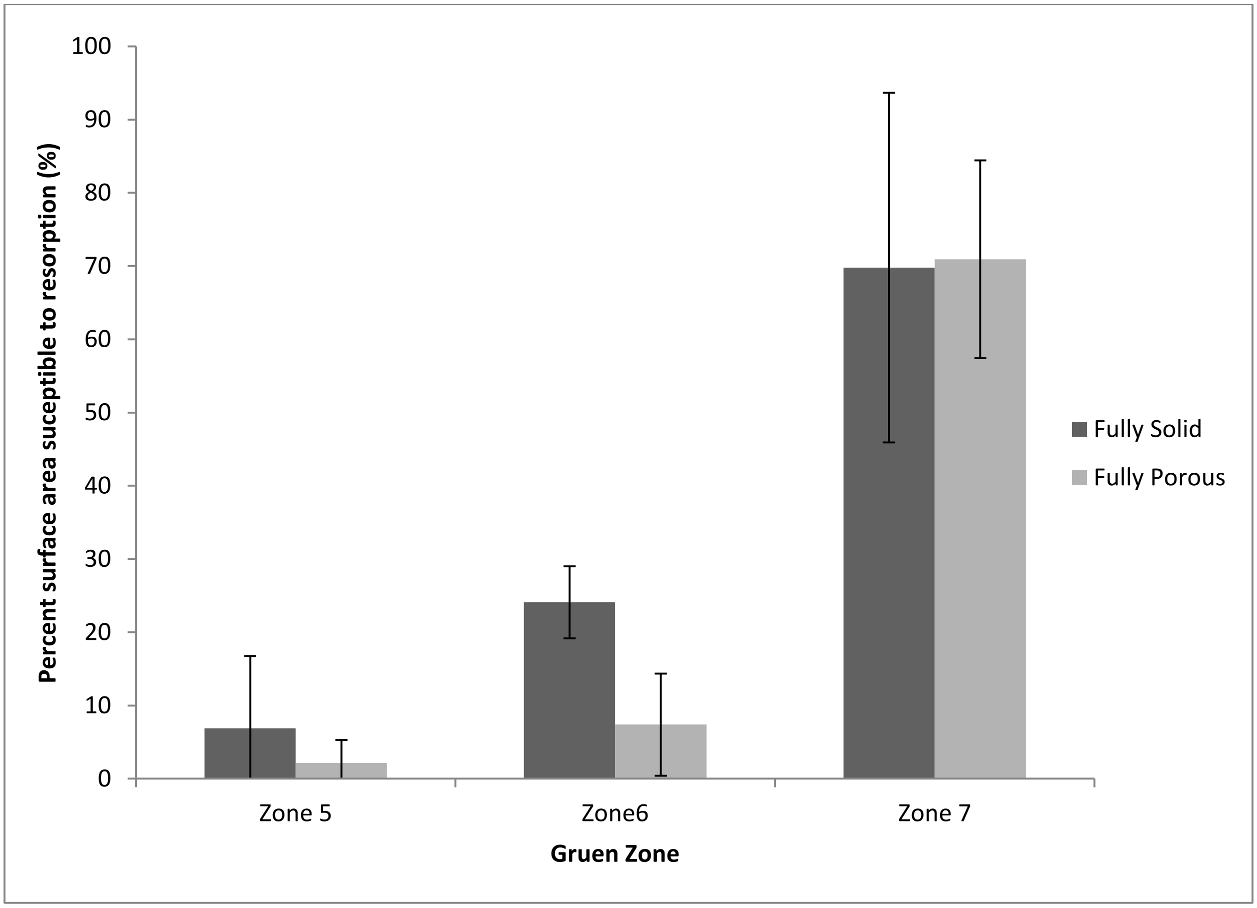

Figure 24: Percent of the area susceptible to bone resorption for fully solid and fully porous implant.

Table 3: Table of intermediate results showing the resorption for each Gruen zone for paired femurs that receive either a fully solid or fully porous implant.

Table of intermediate results

Femur pair	Fully solid implant *average resorption (%)*			Fully porous implant *average resorption (%)*		
	Zone 5	Zone 6	Zone 7	Zone 5	Zone 6	Zone 7
1	2.40	27.57	93.96	5.79	16.39	57.50
2	0.00	22.76	65.68	0.00	0.61	72.36
3	18.20	25.46	46.73	0.67	8.45	81.93
Average	**6.87**	**25.26**	**68.79**	**2.15**	**8.49**	**70.60**
Standard deviation	**9.89**	**2.41**	**23.77**	**3.17**	**7.89**	**12.31**

4.9 Discussion

4.9.1 Interpretation of experimental results

The research question of this chapter was to test whether a tuned fully porous implant can reduce the amount of bone susceptible to stress shielding. This work shows that there is a significant reduction in stress shielding in Gruen zone 6. Since all factors other than the implant were held constant, we can be confident that the variation in strain shielding is a result of the tuned porous hip replacement. Furthermore, the consistency of strain distal to the implant indicates that the comparison is valid, and that the differences are not due to changes in the neck offset.

To the author's knowledge, this is the first time that a tuned fully porous hip replacement has been shown to reduce stress shielding in the proximal femur. This provides an example for how a fully porous biomaterial can be tailored to reduce a serious clinical concern, with potentially fatal complications.

It is important to note that the design of the implant can also greatly affect stress shielding. Previous generation cementless implants where fully porous coated with a cylindrical distal portion that would contact the diaphysis. These cylindrical implants showed significantly higher stress shielding as compared to shorter stems with taperness and proximal coatings for bone ingrowth. The Trilock design that was used for this study falls into the latter category. Furthermore, the tapered proximally coated designs can be implanted using minimally invasive techniques, thereby reducing operative trauma, and the associated surgical recovery. For this reason, proximally tapered minimally invasive implants are substantially more popular.

If a previous generation stem was used, the expected difference in strain shielding would be expected to be much larger; however it could be susceptible to a claim that the improved performance is not equivalent to the performance of modern bone preserving designs. Since this experiment was conducted using a bone preserving macroscopic geometry, the improvement seen from tuned fully porous implant extends beyond that of a state of the art minimally invasive macroscopic geometry, providing a potential new minimum for bone resorption after total hip replacement.

Despite the improvement in stress shielding, Gruen zone 7 demonstrated significant change in loading after implantation for both implants used. This could be partially attributed to the lack of an abductor muscle in the loading case, which if present, would increase the bending moment in the medial lateral plane, thereby increasing the compressive strain on the medial calcar. However, a more likely cause is that the superior aspect of the bone is completely unloaded after the femoral neck is resected. Previous implant designs relied on a collar to load the resected portion of the femoral neck, although they were still made from fully solid high stiffness metals, so little improvement in stress shielding was seen. It is unclear if a combination of a collared design along with a tuned fully porous implant would reduce stress shielding significantly in Gruen zone 7. However, the reduction seen in Gruen zone 6 could potentially lead to a decrease in peri-prosthetic fractures.

The absolute strain was not verified relative to a strain gauge in this experiment. However, previous work by Gilchrist et al has shown reasonable agreement between strain gauges and DIC and indicates that DIC is more appropriate for complex geometries such as human bone [137]. Furthermore, the experimental model presented in this work is not estimating the true strain of the femur, but rather looks at the relative strain between an intact and implanted femur. Because the field quantity of interest is the change of strain, any bias of the DIC experimentation is removed. This is also ensured by the use of a rigid jig fixing the cameras to the load frame, as well as 3D DIC acquired with synchronized stereoscopic image acquisition. This avoids bias that can be introduced by deviations in the optical axis of the camera for overlaid 2D DIC relying on a single camera [138].

4.9.2 Relation to Alternative Designs That Reduce Stress Shielding

Although this chapter presents the first tuned fully porous implant that can reduce stress shielding, there have been several other attempts to reduce stress shielding. The most notable that have been clinically used are iso-elastic composite stems. Iso-elastic stems are designed to have equivalent bending stiffness in the medial lateral plane as the host bone. This is usually achieved through a solid CoCr or Ti64 core, surrounded by a more flexible polymer. The first iso-elastic stems had dismal performance due to excess micromotion after implantation, substantially affecting clinical outcomes, and are no longer used due to the high incidence of adverse effects. More recently, Zimmer developed the Versys Epoch stem, which had a solid CoCr center, surrounded by a polymer, and finally coated in a porous fiber mesh. The implant showed drastic decreases in stress shielding in a long term canine study, despite the fact that the amount of ingrowth was limited due to polymer infiltration into the porous coating during manufacturing. The epoch also has good clinical performance. However, it has not enjoyed widespread use since it is not compatible with a minimally invasive approach. Patient specific anatomically shaped stems have also been proposed and have shown reduced stress shielding in-vitro. Generally, anatomical stems are designed such that they can be implanted in direct contact with the entire length of the proximal medial cortex. Since there is a tight and continuous fit, the load is transferred to the medial calcar, leading to a strain distribution similar to that of the intact femur. In addition to patient-specific anatomical implants, there are also generalized anatomical implants. While they provide less stress shielding compared to fully porous coated implants, they do not offer the performance of a patient-specific stem. The possibility of a patient specific anatomical stem combined with a graded porous microstructure remains an intriguing opportunity to further reduce stress shielding and improve implant performance.

4.9.3 Development in Experimental Assessment of Stress Shielding

There have been a significant number of studies examining the stress shielding phenomenon. They typically rely on surface strain gauges or finite element studies. Although there have also been studies that use photoelastic coatings, thermography camera, and DIC. Although DIC has been used for measuring strain in previous experiments, the technique presented in this chapter represents an advance in the analysis of stress shielding phenomenon in-vivo through the means of a quantitative comparison of two dimensional surface strains on complex anatomical features.

The most common practice for assessing stress shielding has been through the means of surface strain gauges, with the technique first reported by Oh et al to analyze various hip implants in the late seventies [139]. In this experimental design, strain gauge rosettes are placed at various anatomical locations of the proximal femur. Typically one strain gauge is used per Gruen zone, for the given aspect (medial, lateral, anterior, and posterior) of the femur under investigation. This allows for the value of strain at discrete points along the femur. A recent study that employed this design was Østbyhaugh et al, who analyzed the performance of a custom anatomical femoral stem, where they could compare the change in strain at 9 locations between a custom anatomical stem and an ABG-I stem [140]. Although effective and widely used, the strain gauge positioning can vary between each different femur, potentially altering the resulting strain measurement. Additionally, strain information is only known for a select number of discrete points at the location where the strain gauge is bonded to the bone. More recently Tayton et al used DIC to record the surface strain on the medial calcar of a femur that received either a metallic stem or a flexible composite stem [141]. This allowed for qualitative evaluation of the surface strain between both implant types over the entire medial aspect of the femur. They quantitatively analyzed the data by drawing a line from the proximal portion to the distal portion of the stem and comparing the reduction in strain. This can be conceptually understood as an evolution of a point based strain gauge technique of strain values along a line throughout the proximal femur. Again, the positioning of the line could potentially vary, thereby influencing the resulting strain measurements if its positions vary either anteriorly or posteriorly. The technique described in this chapter is a further extension from quantitative discrete strain values and the subsequent evolution to strain values along a line, to strain values along a surface. This allows for quantitative evaluation of the change in surface strain after implantation across the area of interest. Furthermore the registration to an atlas femur ensures that the comparisons between femurs are at nearly identical anatomical locations. The technique is inspired from processing used to analyze the complex changes that occur in functional Magnetic Resonance Imaging (fMRI) activation for stroke recovery patients during rehabilitation [142].The technique introduced in this chapter can be extended to allow for non-rigid registration and can be used for cadaver femora, which possess unique anatomical variations. This would allow for an effective comparison controlling for natural variations in human morphology. A further extension of this processing technique is to use three dimensional volumetric DIC to compare three dimensional variations in strain experimentally. However, the 3D DIC set-up is cumbersome and requires specialized volumetric imaging modalities such as CT or MRI in addition to a speckle contrast throughout the volume of interest[138]. Additionally, it is well documented that implants can degrade the volumetric analysis of three dimensional imaging modalities [143]. As such, its use was unfeasible in the current study.

4.9.4 Relating the Change in Strain In-Vitro to Clinical Data

Although bone resorption secondary to stress shielding is a result of altering the stress after implantation, it is important to note that it is an adaptive process that occurs over time. Generally stress shielding will manifest over the course of 2 years, after which it will become radiographically stable. The current study models a femur directly post-operatively, before there has been ingrowth, and no adaptation is possible. This experimental design serves to represent the proportion of bone in the medial calcar that is susceptible to stress shielding. There exist several computational techniques that will either project bone loss, such as re-iterative modelling that will remove portions of unloaded bone and recomputed the new stress distribution to determine the direction of remodeling. For in-vitro analysis, there are no models available for modeling the temporal variation in bone resorption. This makes a direct comparison to clinical DEXA studies that measure bone resorption difficult, and is further compounded by the difference of a simplified loading in-vitro and the complex physiological loads that are experienced in daily living. Furthermore, a multitude of factors such as age, gender, activity level, comorbidities, and pharmacological agents can affect the extent of stress shielding. Rather than providing exact prediction of the reduction in stress shielding that could be expected in a tuned fully porous hip replacement, this work shows that stress shielding can be reduced. It also complements the physiological FEA model that that shows a reduction in stress shielding for fully porous implants with a tuned microarchitecture. This result provides supporting evidence for further investigations, such as long term animal models that can more accurately capture the biological complexities of bone remodeling.

4.10 Conclusion

This work shows that a tuned fully porous material can be used to reduce stress-shielding, a serious clinical shortcoming of current total hip replacements. The tuned material properties can be achieved through means of mapping a microarchitecture lattice that can be successfully manufactured with no entrapped powder. The design also maintains ideal morphological properties at the bone implant interface to encourage extensive and early ingrowth. Although further in-vivo work is required to assess the true reduction in bone resorption that can be conferred from a fully porous hip replacement, the experimental results bolster previous computational models that predict a reduction in stress shielding and the associated reduction of bone stock. This promising development may possibly pave the way for tuned fully porous microarchitecture bone interfacing implants to increase implant service life in orthopedics.

Chapter 5: Final Remarks and Future Work

In chapter 3, a new method to visualize the interaction of morphological parameters for a unit cell was introduced. The method allows for a systematic understanding of the relation between cell topology, strut thickness, cell size, and the resulting porosity and pore size. It allows also for a clear understanding of the accessible design space that respects bone ingrowth limitations along with minimum nominal strut thickness that can be fabricated through selective laser melting, or any other automated process of manufacture. The results of this work sets the ground for more thorough investigations into the design space to understand the morphological parameters influencing the mechano-biological response of porous biomaterials for bone tissue replacements. The results contribute also to clarify current open issues and conflicting views in the literature on a range of points, such as the influence of strut thickness and cell size on mechanical properties, and the relationship between pore size and porosity for bone ingrowth.

Additionally, this work was the first to propose and introduce the use of stretch dominant topologies, such as tetrahedron and octet truss lattices, for bone interfacing applications. In quasi-static compression the tetrahedron topology can have strength up to five times that of tantalum foam, the most performant material available in the orthopedic market. Bone ingrowth studies confirmed early and extensive ingrowth into both stretch dominant topologies, although the rate of ingrowth is not as extensive as that of tantalum foam. This development is a major breakthrough for fully load bearing orthopedics since a fivefold increase of strength is gained. This entails that more severely loaded implants can be conceivably manufactured, without any compromise in bone growth properties.

Chapter 4 showed how a stretch dominated microarchitectured material can be exploited and tuned to address a clinical problem: bone resorption secondary to stress shielding. Chapter 4 demonstrated, for the first time experimentally, that a tuned fully porous implant with optimum material properties can reduce stress shielding in an in-vitro biomechanical model. The optimized material property distribution is transferred to a detailed design of tessellated tetrahedron microarchitecture by means of a mapping procedure. In addition to achieving graded material properties, the microarchitecture respects bone ingrowth limitations at the bone implant interfaces, and manufacturing limits of SLM throughout the implant. Furthermore, CT analysis has shown that the porous implant was successfully manufactured with no powder entrapment. The reduction of 60% of bone susceptible to stress shielding could conceivably reduce the bone loss and reduce the occurrence of aseptic loosening or peri-prosthetic fracture. The increased bone stock has the potential to substantially decrease the technical complexity and associated risk of a revision surgery. Although the in-vitro reduction of stress shielding has very exciting clinical ramifications, extensive future work is required to investigate the efficacy and safety of a fully porous total hip replacement.

5.1 Future Work: Material Perspective

This section discusses future work from a twin vantage point of further developing the understanding of high strength fully porous materials, as well as the required development for fully porous implants that exploit their structural efficiency.

Morphological analysis clearly showed over melting of struts in the manufactured topology. This discrepancy between the strut as designed and as manufactured results in a shift of the final morphological properties (lower pore size, and lower porosity) from that predicted in the design chart. One possible approach is to incorporate the manufacturing errors into the creation of the design chart. An example of this would be to vary the cross section of struts in the parametric model based on their angle relative to the build plane. Another approach is to minimize the discrepancy between the as designed and as manufactured. This can be achieved from two fronts. The first is machine parameter optimization. In this method, the machine processing parameters such as laser power, scan speed, and hatching distance (among many other parameters) are varied to improve the manufacturing resolution. However, care must be taken to ensure that the resulting parameters can still form fully solid struts, and will not result in material voids throughout the strut thickness [144]. Another method to reduce the manufacturing deviation is with design compensation. In this paradigm, the designed microarchitecture is specifically designed with thinner than desired struts in order to have the over melted geometry be what was originally targeted. Additionally, part of the deviation is incurred from semi melted beads on the strut surface. These semi-melted beads reduce porosity without a significant addition to mechanical strength. Given the complex three dimensional network of lattice microarchitecture, mechanical polishing is extremely difficult. Alternate methods such as pulsed electro polishing can be explored to remove semi sintered beads, along with obtaining optimum nano-scale roughness for bone ingrowth [145].

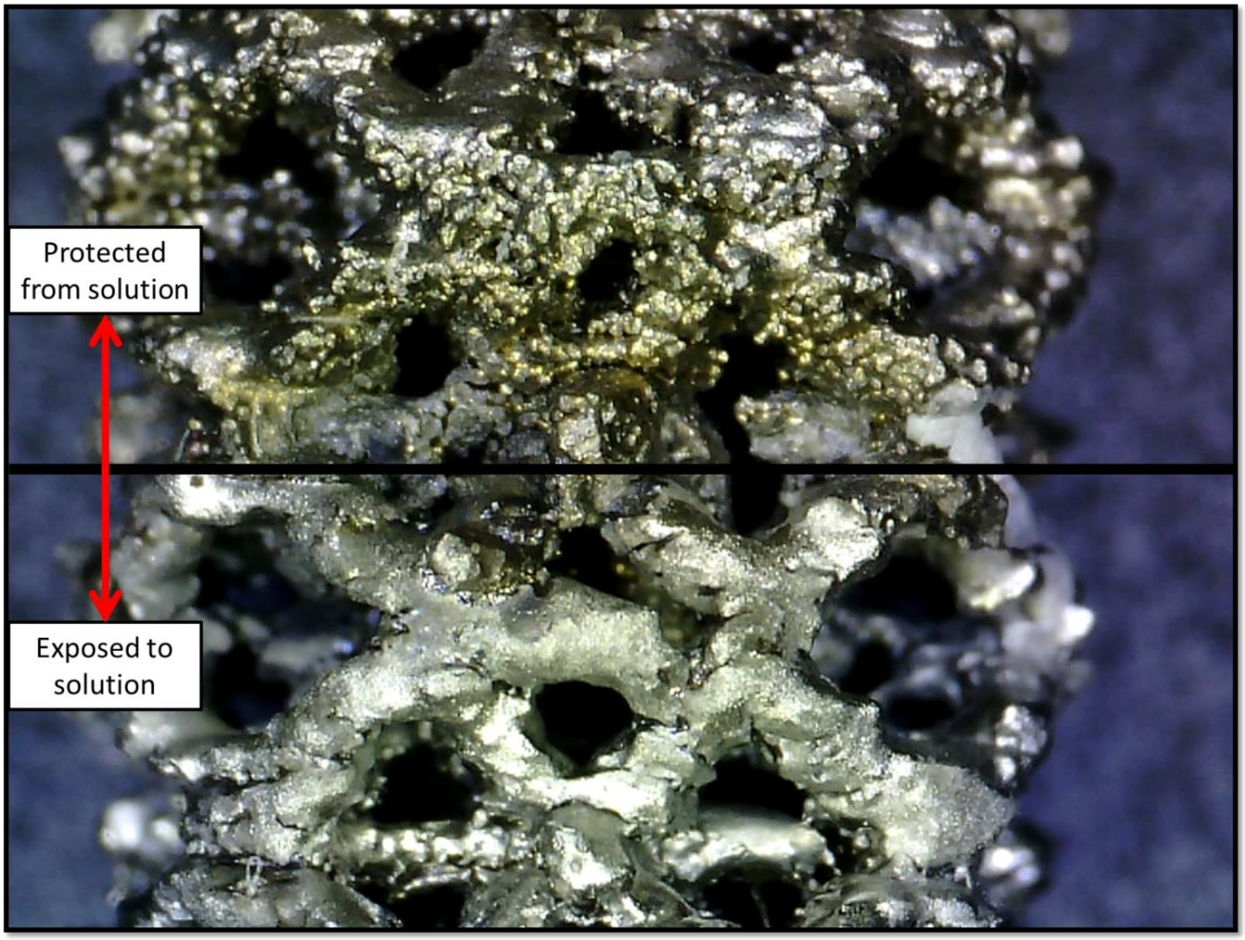

Figure 25: Transcortical implant with semi sintered bead removal through pulsed electro polishing.

The design charts presented in this work provide an intuitive visualization method to assess the interaction of morphological parameters. This improved understanding can be used to systematically assess the interplay between all the morphological parameters and their resulting effect on the mechano-biological response. One possible method for understanding the interactions is through the development of a response surface methodology. In this method, experimental points are selected throughout the design space, and an empirical response which is generated from the data. These data can both serve as a direct addition to the charts as in figures 24 and 25. Alternatively, the empirical response surface can serve as a benchmark to examine the validity of various computational models for mechanical properties and bone ingrowth parameters.

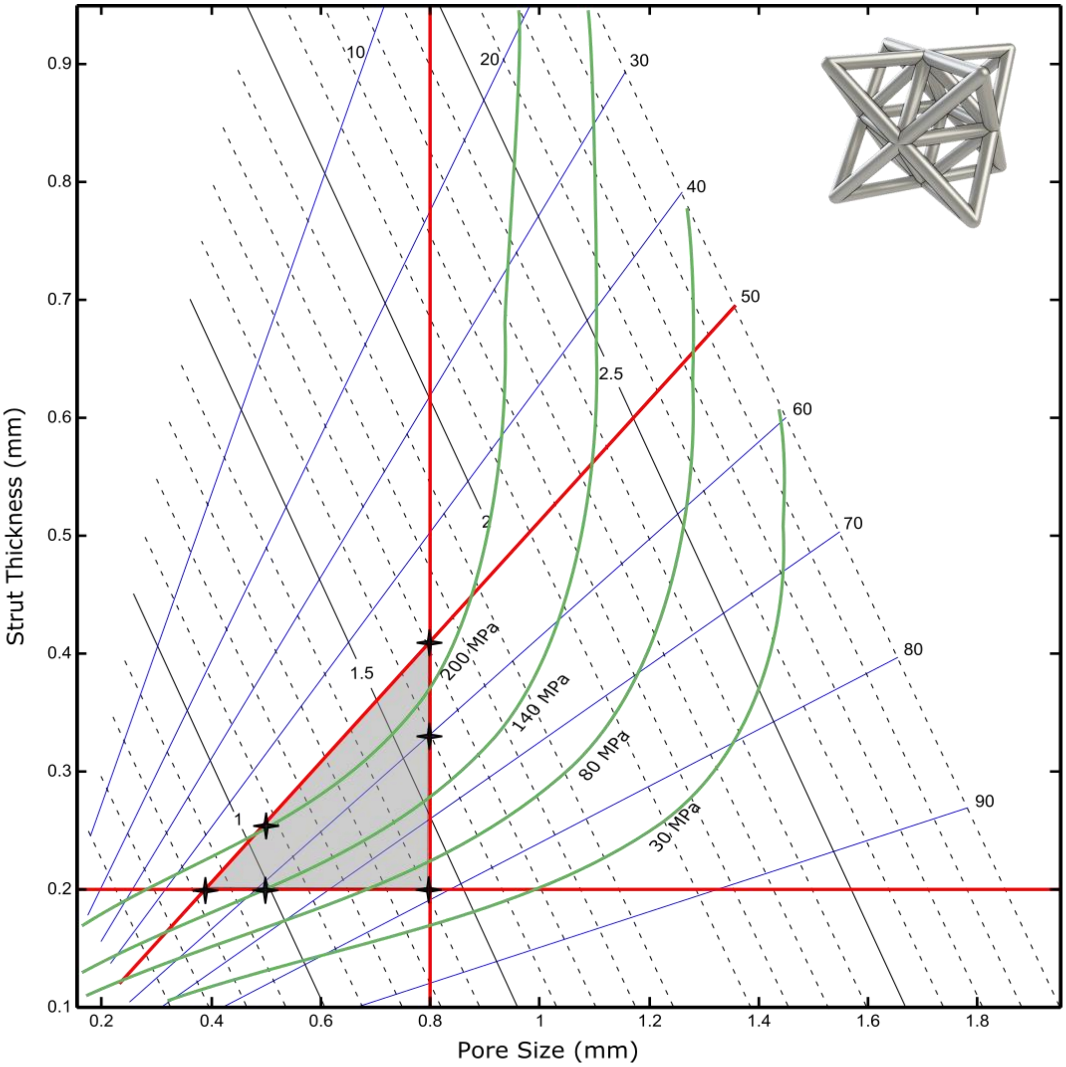

Figure 26: Hypothetical Lines of constant strength as predicted by a response surface created from experimental data throughout the admissible design space and beyond.

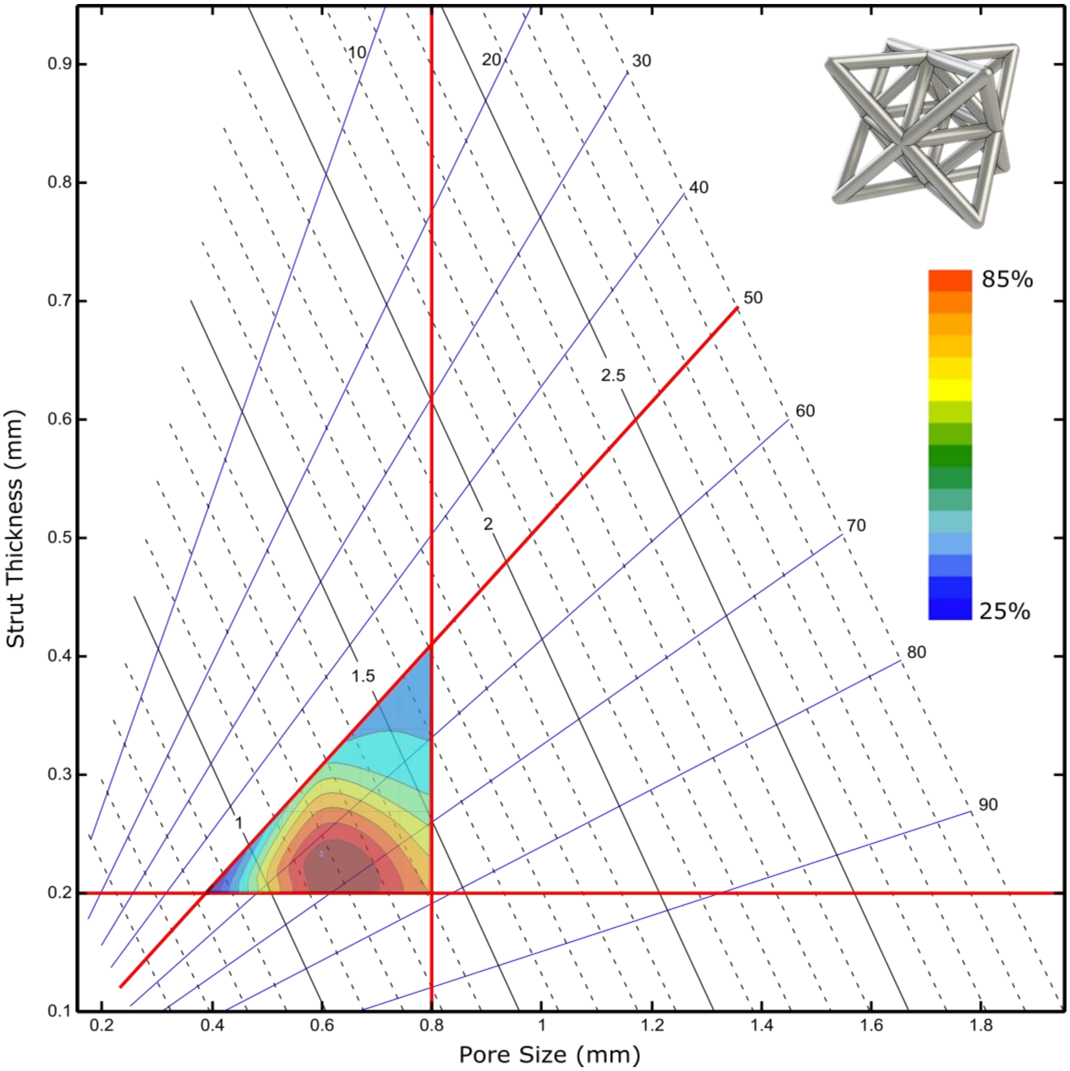

Figure 27: Hypothetical bone ingrowth response over the admissible design space.

To fully understand the behavior of stretch dominated fully porous biomaterials additional loading conditions should be analyzed so as to characterize the full stiffness matrix of the material. Additionally, understanding the fatigue behavior is imperative.

Another important factor is the friction coefficient of the material. As discussed in greater detail in chapter 4, bone ingrowth is dependent upon primary fixation and will not occur if there is excessive micromotion [19]. Micromotion is dependent upon both material stiffness as well as the coefficient of friction. The coefficient of friction should be characterized through standardized means in order to compare it to existing biomaterials through standard techniques.

5.2 Future Work: Total Hip Replacement Development

The development of the total hip replacement application is dependent upon both the work done at the material analysis scale, and to specific functional tests for total hip replacements. Critical tests to ensure the safety of a fully porous hip replacement include micromotion analysis and the determination of the fatigue endurance of the implant.

Micromotion analysis is required on the final implementation of the implant since it is dependent on the stem flexibility and coefficient of friction. The stem flexibility contributes to the shear at the bone implant interface, and the coefficient of friction must be obtained to limit interface motion. As opposed to the stress shielding investigation, which is comparative between two implants, there is a strong consensus for modelling an in-vitro micro motion set up since the obtained value should be interpreted as an absolute result. To measure micromotion, a stair climbing load should be modeled on the femur and micromotion should be less than 50 microns [19]. A micromotion fixture has been designed as described by Østbyhaug et al that simulates stair climbing for micro motion investigations with no holes in the cortex to measure the interface motion [146, 147]. Additionally, although synthetic femurs possess similar overall biomechanical behavior to cadaver femurs, the interface frictional properties vary significantly between natural cadaver bone and synthetic bone used in the sawbones models [148]. As such the micromotion experiments should be conducted on matched pair cadaver femurs.

Figure 28: Physiological loading jig that simulates stair climbing with attached micromotion fixture to measure the movement at the bone implant interface.

Fatigue testing is a major bottle neck for the design orthopedic implants. To assess their fatigue strength, there are two relevant standards that exist for total hip replacement stems. The first and most severe of the standards is ISO 7206:4, which models the worst case fatigue loading of distal fixation. The implant is required to withstand 10 million cycles (simulating ten years of service life) with no fracture or excessive displacement [149]. The second standard simulates proper fixation and examines the fatigue properties of the neck under a similar loading regime [150]. Due to the potential increased service life that would be conferred by a total hip replacement that can reduce stress shielding, the projected service life for fatigue tests may also have to be increased. Additionally, the microarchitecture can be optimized with continuous contours at nodal intersections to improve fatigue life, and future work would involve an optimum implant design that can minimize bone resorption while simultaneously maximizing fatigue life[151].

On a final note, the fully porous microarchitecture is not limited to total hip replacements. It can also be used for a number of applications including trauma, reconstruction, knee, dental and spine.

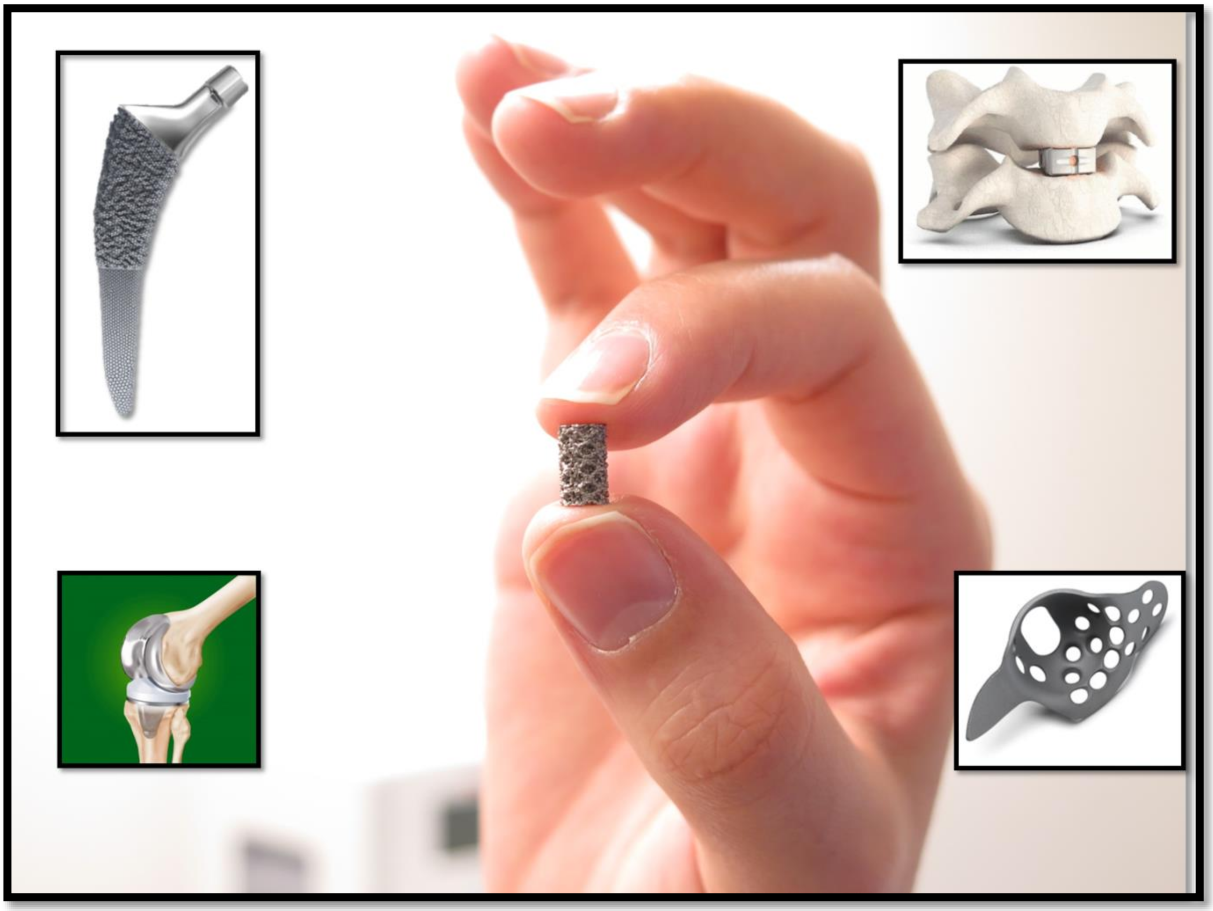

Figure 29: Other potential applications for a high strength fully porous biomaterial. From top left in clockwise order: Total hip replacement, spinal fusion cage, Burch-Schneider pelvic reconstruction cage, and total knee replacement.

References

[1] W. R. Frontera, J. K. Silver, and T. D. Rizzo, *Essentials of physical medicine and rehabilitation: Musculoskeletal disorders, pain, and rehabilitation*: Saunders/Elsevier, 2008.

[2] D. T. Felson, "Epidemiology of hip and knee osteoarthritis," *Epidemiologic reviews,* vol. 10, pp. 1-28, 1987.

[3] R. Crawford and D. Murray, "Total hip replacement: indications for surgery and risk factors for failure," *Annals of the rheumatic diseases,* vol. 56, pp. 455-457, 1997.

[4] S. Kurtz, K. Ong, E. Lau, F. Mowat, and M. Halpern, *Projections of Primary and Revision Hip and Knee Arthroplasty in the United States from 2005 to 2030* vol. 89, 2007.

[5] V. P. Stephanie Cheng, Erc De Sa, Alina Dragam, Shirley Chen, Nicole De Guia, "Title Hip and Knee Replacements in Canada: Canadian Joint Replacement Registry 2013 Annual Report," Canadian Institute for Health Information2013.

[6] G. Hooper, A. Rothwell, M. Stringer, and C. Frampton, "Revision following cemented and uncemented primary total hip replacement a seven-year analysis from the New Zealand Joint Registry," *Journal of Bone & Joint Surgery, British Volume,* vol. 91, pp. 451-458, 2009.

[7] Y.-H. Kim, J.-S. Kim, J.-W. Park, and J.-H. Joo, "Comparison of total hip replacement with and without cement in patients younger than 50 years of age THE RESULTS AT 18 YEARS," *Journal of Bone & Joint Surgery, British Volume,* vol. 93, pp. 449-455, 2011.

[8] L. Tang and J. W. Eaton, "Inflammatory responses to biomaterials," *American journal of clinical pathology,* vol. 103, pp. 466-471, 1995.

[9] D. Murray and N. Rushton, "Macrophages stimulate bone resorption when they phagocytose particles," *Journal of Bone & Joint Surgery, British Volume,* vol. 72, pp. 988-992, 1990.

[10] G. Keegan, I. Learmonth, and C. Case, "Orthopaedic metals and their potential toxicity in the arthroplasty patient A REVIEW OF CURRENT KNOWLEDGE AND FUTURE STRATEGIES," *Journal of Bone & Joint Surgery, British Volume,* vol. 89, pp. 567-573, 2007.

[11] J. Paul, "Force actions transmitted by joints in the human body," *Proceedings of the Royal Society of London B: Biological Sciences,* vol. 192, pp. 163-172, 1976.

[12] E. J. Cheal, M. Spector, and W. C. Hayes, "Role of loads and prosthesis material properties on the mechanics of the proximal femur after total hip arthroplasty," *Journal of orthopaedic research,* vol. 10, pp. 405-422, 1992.

[13] G. Bergmann, F. Graichen, and A. Rohlmann, "Hip joint loading during walking and running, measured in two patients," *Journal of biomechanics,* vol. 26, pp. 969-990, 1993.

[14] B. Morrey, L. Askew, and E. Chao, "A biomechanical study of normal functional elbow motion," *The Journal of Bone & Joint Surgery,* vol. 63, pp. 872-877, 1981.

[15] J. Hurov, "Anatomy and mechanics of the shoulder: review of current concepts," *Journal of Hand therapy,* vol. 22, pp. 328-343, 2009.

[16] C. M. Styles, S. L. Evans, and P. J. Gregson, "Development of fatigue lifetime predictive test methods for hip implants: Part I. Test methodology," *Biomaterials,* vol. 19, pp. 1057-1065, 1998.

[17] T. P. Schmalzried, E. S. Szuszczewicz, M. R. Northfield, K. H. Akizuki, R. E. Frankel, G. Belcher*, et al.*, "Quantitative assessment of walking activity after total hip or knee replacement*," *The Journal of Bone & Joint Surgery,* vol. 80, pp. 54-9, 1998.

[18] S. D. Cook and K. A. Thomas, "Fatigue failure of noncemented porous-coated implants. A retrieval study," *Journal of Bone & Joint Surgery, British Volume,* vol. 73, pp. 20-24, 1991.

[19] R. Pilliar, J. Lee, and C. Maniatopoulos, "Observations on the effect of movement on bone ingrowth into porous-surfaced implants," *Clinical orthopaedics and related research,* vol. 208, pp. 108-113, 1986.

[20] C. A. Engh, D. O'Connor, M. Jasty, T. F. McGovern, J. D. Bobyn, and W. H. Harris, "Quantification of implant micromotion, strain shielding, and bone resorption with porous-coated anatomic medullary locking femoral prostheses," *Clinical orthopaedics and related research,* vol. 285, pp. 13-29, 1992.

[21] M. Fini, G. Giavaresi, P. Torricelli, V. Borsari, R. Giardino, A. Nicolini*, et al.*, "Osteoporosis and biomaterial osteointegration," *Biomed Pharmacother,* vol. 58, pp. 487-93, Nov 2004.

[22] A. F. Mavrogenis, R. Dimitriou, J. Parvizi, and G. C. Babis, "Biology of implant osseointegration," *J Musculoskelet Neuronal Interact,* vol. 9, pp. 61-71, Apr-Jun 2009.

[23] J. Bobyn, R. Pilliar, H. Cameron, and G. Weatherly, "The optimum pore size for the fixation of porous-surfaced metal implants by the ingrowth of bone," *Clinical Orthopaedics and Related Research,* vol. 150, p. 263, 1980.

[24] C. Engh, J. Bobyn, and A. Glassman, "Porous-coated hip replacement. The factors governing bone ingrowth, stress shielding, and clinical results," *Journal of Bone & Joint Surgery, British Volume,* vol. 69, p. 45, 1987.

[25] J. Bobyn, G. Stackpool, S. Hacking, M. Tanzer, and J. Krygier, "Characteristics of bone ingrowth and interface mechanics of a new porous tantalum biomaterial," *Journal of Bone & Joint Surgery, British Volume,* vol. 81, pp. 907-914, 1999.

[26] M. Shalabi, A. Gortemaker, M. Hof, J. Jansen, and N. Creugers, "Implant surface roughness and bone healing: a systematic review," *Journal of dental research,* vol. 85, p. 496, 2006.

[27] S. J. Hollister, "Scaffold Design and Manufacturing: From Concept to Clinic," *Advanced materials,* vol. 21, pp. 3330-3342, 2009.

[28] C. Bragdon, M. Jasty, M. Greene, H. Rubash, and W. Harris, "Biologic fixation of total hip implants: Insights gained from a series of canine studies," *The Journal of Bone and Joint Surgery,* vol. 86, pp. 105-117, 2004.

[29] O. L. A. Harrysson, O. Cansizoglu, D. J. Marcellin-Little, D. R. Cormier, and H. A. West Ii, "Direct metal fabrication of titanium implants with tailored materials and mechanical properties using electron beam melting technology," *Materials Science and Engineering: C,* vol. 28, pp. 366-373, 2008.

[30] L. Carlsson, T. Röstlund, B. Albrektsson, and T. Albrektsson, "Implant fixation improved by close fit Cylindrical implant-bone interface studied in rabbits," *Acta Orthopaedica,* vol. 59, pp. 272-275, 1988.

[31] M. Jasty, C. R. Bragdon, T. Haire, R. D. Mulroy Jr, and W. H. Harris, "Comparison of bone ingrowth into cobalt chrome sphere and titanium fiber mesh porous coated cementless canine acetabular components," *Journal of biomedical materials research,* vol. 27, pp. 639-644, 1993.

[32] M. Jasty, C. Bragdon, D. Burke, D. O'connor, J. Lowenstein, and W. H. Harris, "In Vivo Skeletal Responses to Porous-Surfaced Implants Subjected to Small Induced Motions*," *The Journal of Bone & Joint Surgery,* vol. 79, pp. 707-14, 1997.

[33] T. A. Schaedler, A. J. Jacobsen, A. Torrents, A. E. Sorensen, J. Lian, J. R. Greer*, et al.*, "Ultralight metallic microlattices," *Science,* vol. 334, pp. 962-965, 2011.

[34] L. J. Gibson and M. F. Ashby, *Cellular solids: structure and properties*. Cambridge, UK: Cambridge University Press, 1999.

[35] G. Ryan, A. Pandit, and D. P. Apatsidis, "Fabrication methods of porous metals for use in orthopaedic applications," *Biomaterials,* vol. 27, pp. 2651-2670, 2006.

[36] R. Lakes, "Materials with structural hierarchy," *Nature,* vol. 361, pp. 511-515, 1993.

[37] ISO, "Compression test for porous and cellular metals," in *Mechanical testing of metals - Ductility testing*, ed, 2011.

[38] B. Levine, "A new era in porous metals: applications in orthopaedics," *Advanced Engineering Materials,* vol. 10, pp. 788-792, 2008.

[39] J. D. Bobyn, R. Poggie, J. Krygier, D. Lewallen, A. Hanssen, R. Lewis*, et al.*, "Clinical validation of a structural porous tantalum biomaterial for adult reconstruction," *The Journal of Bone and Joint Surgery,* vol. 86, pp. 123-129, 2004.

[40] H. Hahn and W. Palich, "Preliminary evaluation of porous metal surfaced titanium for orthopedic implants," *Journal of biomedical materials research,* vol. 4, pp. 571-577, 1970.

[41] M. Bram, C. Stiller, H. P. Buchkremer, D. Stöver, and H. Baur, "High-Porosity Titanium, Stainless Steel, and Superalloy Parts," *Advanced Engineering Materials,* vol. 2, pp. 196-199, 2000.

[42] C. Wen, M. Mabuchi, Y. Yamada, K. Shimojima, Y. Chino, and T. Asahina, "Processing of biocompatible porous Ti and Mg," *Scripta Materialia,* vol. 45, pp. 1147-1153, 2001.

[43] M. Assad, P. Jarzem, M. A. Leroux, C. Coillard, A. V. Chernyshov, S. Charette*, et al.*, "Porous titanium-nickel for intervertebral fusion in a sheep model: Part 1. Histomorphometric and radiological analysis1," *Journal of Biomedical Materials Research Part B: Applied Biomaterials,* vol. 64, pp. 107-120, 2003.

[44] C. A. Engh and R. H. Hopper, "The odyssey of porous-coated fixation," *The Journal of Arthroplasty,* vol. 17, pp. 102-107, 2002.

[45] M. Petersen, I. Poulsen, J. Thomsen, and S. Solgaard, "The Hemispherical Harris-Galante Acetabular Cup, Inserted without Cement. The Results of an Eight to Eleven-Year Follow-up of One Hundred and Sixty-Eight Hips*," *The Journal of Bone & Joint Surgery,* vol. 81, pp. 219-224, 1999.

[46] J. W. MCCUTCHEN, J. P. COLLIER, and M. B. MAYOR, "Osseointegration of titanium implants in total hip arthroplasty," *Clinical orthopaedics and related research,* vol. 261, pp. 114-125, 1990.

[47] J. M. Sobral, S. G. Caridade, R. A. Sousa, J. F. Mano, and R. L. Reis, "Three-dimensional plotted scaffolds with controlled pore size gradients: Effect of scaffold geometry on mechanical performance and cell seeding efficiency," *Acta Biomaterialia,* vol. 7, pp. 1009-1018, 2011.

[48] L. Murr, S. Gaytan, F. Medina, H. Lopez, E. Martinez, B. Machado*, et al.*, "Next-generation biomedical implants using additive manufacturing of complex, cellular and functional

mesh arrays," *Philosophical Transactions of the Royal Society A: Mathematical, Physical and Engineering Sciences,* vol. 368, pp. 1999-2032, 2010.

[49] L. E. Murr, S. M. Gaytan, E. Martinez, F. Medina, and R. B. Wicker, "Next Generation Orthopaedic Implants by Additive Manufacturing Using Electron Beam Melting," *International Journal of Biomaterials,* vol. 2012, 2012.

[50] M. Manley, G. Kotzar, L. Stern, and A. Wilde, "Effects of repetitive loading on the integrity of porous coatings," *Clinical orthopaedics and related research,* vol. 217, pp. 293-302, 1987.

[51] L. D. Zardiackas, D. E. Parsell, L. D. Dillon, D. W. Mitchell, L. A. Nunnery, and R. Poggie, "Structure, metallurgy, and mechanical properties of a porous tantalum foam," *Journal of biomedical materials research,* vol. 58, pp. 180-187, 2001.

[52] D. A. Shimko, V. F. Shimko, E. A. Sander, K. F. Dickson, and E. A. Nauman, "Effect of porosity on the fluid flow characteristics and mechanical properties of tantalum scaffolds," *Journal of Biomedical Materials Research Part B: Applied Biomaterials,* vol. 73, pp. 315-324, 2005.

[53] A. D. Heiner, R. A. Poggie, and T. D. Brown, "Flexural Rigidity of Laboratory and Surgical Substitutes for Human Fibular Bone Grafts," *Journal of Musculoskeletal Research,* vol. 02, pp. 267-272, 1998.

[54] F. P. W. Melchels, M. A. N. Domingos, T. J. Klein, J. Malda, P. J. Bartolo, and D. W. Hutmacher, "Additive manufacturing of tissues and organs," *Progress in Polymer Science,* vol. 37, pp. 1079-1104, 8// 2012.

[55] S. H. Huang, P. Liu, A. Mokasdar, and L. Hou, "Additive manufacturing and its societal impact: a literature review," *The International Journal of Advanced Manufacturing Technology,* vol. 67, pp. 1191-1203, 2013.

[56] T. W. Bauer and S. T. Smith, "Bioactive materials in orthopaedic surgery: overview and regulatory considerations," *Clinical orthopaedics and related research,* vol. 395, pp. 11-22, 2002.

[57] T. H. Smit, T. A. P. Engels, S. H. M. Söntjens, and L. E. Govaert, "Time-dependent failure in load-bearing polymers: a potential hazard in structural applications of polylactides," *Journal of Materials Science. Materials in Medicine,* vol. 21, pp. 871-878, 11/07

[58] M. Niinomi, "Mechanical properties of biomedical titanium alloys," *Materials Science and Engineering: A,* vol. 243, pp. 231-236, 1998.

[59] L. Mullen, R. Stamp, W. Brooks, E. Jones, and C. Sutcliffe, "Selective Laser Melting: A regular unit cell approach for the manufacture of porous, titanium, bone in-growth constructs, suitable for orthopedic applications," *Journal of Biomedical Materials Research Part B: Applied Biomaterials,* vol. 89, pp. 325-334, 2008.

[60] C. Y. Lin, N. Kikuchi, and S. J. Hollister, "A novel method for biomaterial scaffold internal architecture design to match bone elastic properties with desired porosity," *Journal of Biomechanics,* vol. 37, pp. 623-636, 2004.

[61] S. J. Hollister, "Porous scaffold design for tissue engineering," *Nature materials,* vol. 4, pp. 518-524, 2005.

[62] H. Kang, C. Y. Lin, and S. J. Hollister, "Topology optimization of three dimensional tissue engineering scaffold architectures for prescribed bulk modulus and diffusivity," *Structural and Multidisciplinary Optimization,* vol. 42, pp. 633-644, 2010.

[63] S. Arabnejad Khanoki and D. Pasini, "Fatigue design of a mechanically biocompatible lattice for a proof-of-concept femoral stem," *Journal of the Mechanical Behavior of Biomedical Materials,* vol. 22, pp. 65-83, 2013.

[64] C. M. Bidan, K. P. Kommareddy, M. Rumpler, P. Kollmannsberger, P. Fratzl, and J. W. Dunlop, "Geometry as a factor for tissue growth: towards shape optimization of tissue engineering scaffolds," *Advanced healthcare materials,* vol. 2, pp. 186-194, 2013.

[65] H. Rodrigues, J. Guedes, and M. Bendsoe, "Hierarchical optimization of material and structure," *Structural and Multidisciplinary Optimization,* vol. 24, pp. 1-10, 2002.

[66] C. Cheah, C. Chua, K. Leong, and S. Chua, "Development of a tissue engineering scaffold structure library for rapid prototyping. Part 1: investigation and classification," *The International Journal of Advanced Manufacturing Technology,* vol. 21, pp. 291-301, 2003.

[67] S. Van Bael, Y. C. Chai, S. Truscello, M. Moesen, G. Kerckhofs, H. Van Oosterwyck*, et al.*, "The effect of pore geometry on the in vitro biological behavior of human periosteum-derived cells seeded on selective laser-melted Ti6Al4V bone scaffolds," *Acta Biomaterialia,* vol. 8, pp. 2824-2834, 2012.

[68] M. A. Wettergreen, B. S. Bucklen, B. Starly, E. Yuksel, W. Sun, and M. A. K. Liebschner, "Creation of a unit block library of architectures for use in assembled scaffold engineering," *Computer-Aided Design,* vol. 37, pp. 1141-1149, 2005.

[69] M. Jamshidinia, L. Wang, W. Tong, and R. Kovacevic, "The bio-compatible dental implant designed by using non-stochastic porosity produced by Electron Beam Melting® (EBM)," *Journal of Materials Processing Technology,* vol. 214, pp. 1728-1739, 2014.

[70] M. de Wild, R. Schumacher, K. Mayer, E. Schkommodau, D. Thoma, M. Bredell*, et al.*, "Bone Regeneration by the Osteoconductivity of Porous Titanium Implants Manufactured by Selective Laser Melting: A Histological and Micro Computed Tomography Study in the Rabbit," *Tissue Engineering Part A,* vol. 19, pp. 2645-2654, 2013.

[71] J. Parthasarathy, B. Starly, S. Raman, and A. Christensen, "Mechanical evaluation of porous titanium (Ti6Al4V) structures with electron beam melting (EBM)," *Journal of the Mechanical Behavior of Biomedical Materials,* vol. 3, pp. 249-259, 2010.

[72] V. Deshpande, M. Ashby, and N. Fleck, "Foam topology: bending versus stretching dominated architectures," *Acta Materialia,* vol. 49, pp. 1035-1040, 2001.

[73] M. S. A. Elsayed and D. Pasini, "Multiscale structural design of columns made of regular octet-truss lattice material," *International Journal of Solids and Structures,* vol. 47, pp. 1764-1774, 2010.

[74] A. Vigliotti and D. Pasini, "Linear multiscale analysis and finite element validation of stretching and bending dominated lattice materials," *Mechanics of Materials,* vol. 46, pp. 57-68, 2012.

[75] V. Karageorgiou and D. Kaplan, "Porosity of 3D biomaterial scaffolds and osteogenesis," *Biomaterials,* vol. 26, pp. 5474-5491, 2005.

[76] E. Abele, H. A. Stoffregen, M. Kniepkamp, S. Lang, and M. Hampe, "Selective laser melting for manufacturing of thin-walled porous elements," *Journal of Materials Processing Technology,* vol. 215, pp. 114-122, 2015.

[77] I. Yadroitsev, I. Shishkovsky, P. Bertrand, and I. Smurov, "Manufacturing of fine-structured 3D porous filter elements by selective laser melting," *Applied Surface Science,* vol. 255, pp. 5523-5527, 2009.

[78] B. S. Institution, "Mechanical testing of metals – ductility testing – compression test for porous and cellular metals," ed, 2011.

[79] G. Bugeda Miguel Cervera and G. Lombera, "Numerical prediction of temperature and density distributions in selective laser sintering processes," *Rapid Prototyping Journal,* vol. 5, pp. 21-26, 1999.

[80] D. A. Hollander, M. Von Walter, T. Wirtz, R. Sellei, B. Schmidt-Rohlfing, O. Paar*, et al.*, "Structural, mechanical and in vitro characterization of individually structured Ti–6Al–4V produced by direct laser forming," *Biomaterials,* vol. 27, pp. 955-963, 2006.

[81] F. J. O'Brien, B. A. Harley, M. A. Waller, I. V. Yannas, L. J. Gibson, and P. J. Prendergast, "The effect of pore size on permeability and cell attachment in collagen scaffolds for tissue engineering," *Technology and Health Care,* vol. 15, pp. 3-17, 2007.

[82] J. Li, J. De Wijn, C. Van Blitterswijk, and K. De Groot, "The effect of scaffold architecture on properties of direct 3D fiber deposition of porous Ti6Al4V for orthopedic implants," *Journal of Biomedical Materials Research Part A,* vol. 92, pp. 33-42, 2010.

[83] G. Pyka, A. Burakowski, G. Kerckhofs, M. Moesen, S. Van Bael, J. Schrooten*, et al.*, "Surface modification of Ti6Al4V open porous structures produced by additive manufacturing," *Advanced Engineering Materials,* vol. 14, pp. 363-370, 2012.

[84] L. Mullen, R. C. Stamp, P. Fox, E. Jones, C. Ngo, and C. J. Sutcliffe, "Selective laser melting: A unit cell approach for the manufacture of porous, titanium, bone in-growth constructs, suitable for orthopedic applications. II. Randomized structures," *Journal of Biomedical Materials Research Part B: Applied Biomaterials,* vol. 92B, pp. 178-188, 2010.

[85] M. F. Ashby, *Metal foams: a design guide*: Butterworth-Heinemann, 2000.

[86] A. Simone and L. Gibson, "Effects of solid distribution on the stiffness and strength of metallic foams," *Acta Materialia,* vol. 46, pp. 2139-2150, 1998.

[87] K. Hazlehurst, C. J. Wang, and M. Stanford, "Evaluation of the stiffness characteristics of square pore CoCrMo cellular structures manufactured using laser melting technology for potential orthopaedic applications," *Materials & Design,* vol. 51, pp. 949-955, 2013.

[88] C. Yan, L. Hao, A. Hussein, and D. Raymont, "Evaluations of cellular lattice structures manufactured using selective laser melting," *International Journal of Machine Tools and Manufacture,* vol. 62, pp. 32-38, 11// 2012.

[89] P. H. Warnke, T. Douglas, P. Wollny, E. Sherry, M. Steiner, S. Galonska*, et al.*, "Rapid prototyping: porous titanium alloy scaffolds produced by selective laser melting for bone tissue engineering," *Tissue engineering part c: Methods,* vol. 15, pp. 115-124, 2008.

[90] S. R. Frenkel, W. L. Jaffe, F. Dimaano, K. Iesaka, and T. Hua, "Bone response to a novel highly porous surface in a canine implantable chamber," *Journal of Biomedical Materials Research Part B: Applied Biomaterials,* vol. 71, pp. 387-391, 2004.

[91] A. Glassman, J. Bobyn, and M. Tanzer, "New Femoral Designs Do They Influence Stress Shielding?," *Clinical Orthopaedics and Related Research,* vol. 453, pp. 64-74, 2006.

[92] S. B. Goodman, "The effects of micromotion and particulate materials on tissue differentiation: bone chamber studies in rabbits," *Acta Orthopaedica,* vol. 65, pp. 1-43, 1994.

[93] D. Dan, D. Germann, H. Burki, P. Hausner, U. Kappeler, R. P. Meyer*, et al.*, "Bone loss after total hip arthroplasty," *Rheumatology international,* vol. 26, pp. 792-798, 2006.

[94] A. V. Lombardi Jr, T. Mallory, B. Vaughn, and P. Drouillard, "Aseptic loosening in total hip arthroplasty secondary to osteolysis induced by wear debris from titanium-alloy modular femoral heads," *The Journal of Bone & Joint Surgery,* vol. 71, pp. 1337-1342, 1989.

[95] H. C. Amstutz, P. Campbell, N. Kossovsky, and I. C. Clarke, "Mechanism and clinical significance of wear debris-induced osteolysis," *Clinical orthopaedics and related research,* vol. 276, pp. 7-18, 1992.

[96] L. Linder, "Implant stability, histology, RSA and wear-more critical questions are needed: A view point," *Acta Orthopaedica,* vol. 65, pp. 654-658, 1994.

[97] H. M. vander Vis, P. A. Berg, R. de Kleine, W. Tigchelaar, and C. J. van Noorden, "Short periods of oscillating fluid pressure directed at a titanium-bone interface in rabbits lead to bone lysis," *Acta Orthopaedica,* vol. 69, pp. 5-10, 1998.

[98] V. Hitchins and K. Merritt, "Decontaminating particles exposed to bacterial endotoxin (LPS)," *Journal of biomedical materials research,* vol. 46, pp. 434-437, 1999.

[99] A. A. Ragab, R. Van De Motter, S. A. Lavish, V. M. Goldberg, J. T. Ninomiya, C. R. Carlin*, et al.*, "Measurement and removal of adherent endotoxin from titanium particles and implant surfaces," *Journal of Orthopaedic Research,* vol. 17, pp. 803-809, 1999.

[100] T. Schmalzried, M. Jasty, and W. H. Harris, "Periprosthetic bone loss in total hip arthroplasty. Polyethylene wear debris and the concept of the effective joint space," *The Journal of Bone & Joint Surgery,* vol. 74, pp. 849-863, 1992.

[101] J. Bobyn, J. Jacobs, M. Tanzer, R. Urban, R. Aribindi, D. Sumner*, et al.*, "The susceptibility of smooth implant surfaces to periimplant fibrosis and migration of polyethylene wear debris," *Clinical Orthopaedics and Related Research,* vol. 311, p. 21, 1995.

[102] J. B. Matthews, A. A. Besong, T. R. Green, M. H. Stone, B. M. Wroblewski, J. Fisher*, et al.*, "Evaluation of the response of primary human peripheral blood mononuclear phagocytes to challenge with in vitro generated clinically relevant UHMWPE particles of known size and dose," *Journal of biomedical materials research,* vol. 52, pp. 296-307, 2000.

[103] J. L. Katz, "Anisotropy of Young's modulus of bone," *Nature,* vol. 283, pp. 106-107, 1980.

[104] J. Wolff, "Das gesetz der transformation der knochen," *Berlin,* pp. 1-139, 1892.

[105] A. Chamay and P. Tschantz, "Mechanical influences in bone remodeling. Experimental research on Wolff's law," *Journal of Biomechanics,* vol. 5, pp. 173-180, 1972.

[106] D. R. Sumner, T. M. Turner, R. Igloria, R. M. Urban, and J. O. Galante, "Functional adaptation and ingrowth of bone vary as a function of hip implant stiffness," *Journal of Biomechanics,* vol. 31, pp. 909-917, 1998.

[107] W. D. Bugbee, W. J. Culpepper, C. A. Engh, and C. A. Engh, *Long-Term Clinical Consequences of Stress-Shielding after Total Hip Arthroplasty without Cement** vol. 79, 1997.

[108] C. A. Engh Jr, A. M. Young, C. A. Engh Sr, and R. H. Hopper Jr, "Clinical consequences of stress shielding after porous-coated total hip arthroplasty," *Clinical orthopaedics and related research,* vol. 417, pp. 157-163, 2003.

[109] S. Kurtz, K. Ong, E. Lau, F. Mowat, and M. Halpern, "Projections of primary and revision hip and knee arthroplasty in the United States from 2005 to 2030," *The Journal of Bone and Joint Surgery (American),* vol. 89, pp. 780-785, 2007.

[110] P. Fernandes, J. Folgado, and R. Ruben, "Shape optimization of a cementless hip stem for a minimum of interface stress and displacement," *Computer Methods in Biomechanics and Biomedical Engineering,* vol. 7, pp. 51-61, 2004.

[111] M. G. Joshi, S. G. Advani, F. Miller, and M. H. Santare, "Analysis of a femoral hip prosthesis designed to reduce stress shielding," *Journal of Biomechanics,* vol. 33, pp. 1655-1662, 2000.

[112] T. Niinimäki, J. Junila, and P. Jalovaara, "A proximal fixed anatomic femoral stem reduces stress shielding," *International orthopaedics,* vol. 25, pp. 85-88, 2001.

[113] T. V. Swanson, "The tapered press fit total hip arthroplasty: a European alternative," *The Journal of arthroplasty,* vol. 20, pp. 63-67, 2005.

[114] R. Crowninshield, R. Brand, R. Johnston, and J. Milroy, "An analysis of femoral component stem design in total hip arthroplasty," *The Journal of Bone & Joint Surgery,* vol. 62, pp. 68-78, 1980.

[115] C. Mattheck, U. Vorberg, and C. Kranz, "Effects of hollow shaft endoprosthesis on stress distribution in cortical bone," *Biomedizinische Technik. Biomedical engineering,* vol. 35, pp. 316-319, 1990.

[116] H. Hedia, M. Shabara, T. El-Midany, and N. Fouda, "A method of material optimization of cementless stem through functionally graded material," *International Journal of Mechanics and Materials in Design,* vol. 1, pp. 329-346, 2004.

[117] S. Arabnejad and D. Pasini, "The Fatigue Design of a Bone Preserving Hip Implant With Functionally Graded Cellular Material," *Journal of Medical Devices,* vol. 7, p. 020907, 2013.

[118] O. L. Harrysson, O. Cansizoglu, D. J. Marcellin-Little, D. R. Cormier, and H. A. West, "Direct metal fabrication of titanium implants with tailored materials and mechanical properties using electron beam melting technology," *Materials Science and Engineering: C,* vol. 28, pp. 366-373, 2008.

[119] S. Arabnejad, B. Johnston, J. A. Pura, B. Singh, M. Tanzer, and D. Pasini, "Title," unpublished|.

[120] A. Khoda, I. T. Ozbolat, and B. Koc, "Engineered tissue scaffolds with variational porous architecture," *Journal of biomechanical engineering,* vol. 133, p. 011001, 2011.

[121] S. Arabnejad and D. Pasini, "Multiscale Design and Multiobjective Optimization of Orthopedic Hip Implants with Functionally Graded Cellular Material," *Journal of Biomechanical Engineering,* vol. 134, p. 031004, 2012.

[122] C. Zannoni, R. Mantovani, and M. Viceconti, "Material properties assignment to finite element models of bone structures: a new method," *Medical Engineering & Physics,* vol. 20, pp. 735-740, 1999.

[123] D. C. Wirtz, N. Schiffers, T. Pandorf, K. Radermacher, D. Weichert, and R. Forst, "Critical evaluation of known bone material properties to realize anisotropic FE-simulation of the proximal femur," *Journal of Biomechanics,* vol. 33, pp. 1325-1330, 2000.

[124] M. O. Heller, G. Bergmann, J. P. Kassi, L. Claes, N. P. Haas, and G. N. Duda, "Determination of muscle loading at the hip joint for use in pre-clinical testing," *Journal of Biomechanics,* vol. 38, pp. 1155-1163, 2005.

[125] J. D. BOBYN, E. S. MORTIMER, A. H. GLASSMAN, C. A. ENGH, J. E. MILLER, and C. E. BROOKS, "Producing and Avoiding Stress Shielding: Laboratory and Clinical Observations

of Noncemented Total Hip Arthroplasty," *Clinical orthopaedics and related research,* vol. 274, pp. 79-96, 1992.

[126] L. Cristofolini, "A critical analysis of stress shielding evaluation of hip prostheses," *Critical Reviews™ in Biomedical Engineering,* vol. 25, 1997.

[127] I. A. Kapandji, *The Physiology of the Joints: Lower limb*: Churchill Livingstone, 1987.

[128] A. D. Heiner, "Structural properties of fourth-generation composite femurs and tibias," *Journal of Biomechanics,* vol. 41, pp. 3282-3284, 2008.

[129] L. Cristofolini, M. Viceconti, A. Cappello, and A. Toni, "Mechanical validation of whole bone composite femur models," *Journal of biomechanics,* vol. 29, pp. 525-535, 1996.

[130] T. H. Mallory, W. C. Head, and A. V. Lombardi Jr, "Tapered design for the cementless total hip arthroplasty femoral component," *Clinical orthopaedics and related research,* vol. 344, p. 172, 1997.

[131] L. Cristofolini and M. Viceconti, "In vitro stress shielding measurements can be affected by large errors," *The Journal of arthroplasty,* vol. 14, pp. 215-219, 1999.

[132] G. Lecerf, M. H. Fessy, R. Philippot, P. Massin, F. Giraud, X. Flecher*, et al.*, "Femoral offset: Anatomical concept, definition, assessment, implications for preoperative templating and hip arthroplasty," *Orthopaedics & Traumatology: Surgery & Research,* vol. 95, pp. 210-219, 5// 2009.

[133] C. Engh and J. Bobyn, "The influence of stem size and extent of porous coating on femoral bone resorption after primary cementless hip arthroplasty," *Clinical Orthopaedics and Related Research,* vol. 231, pp. 7-28, 1988.

[134] S. J. MacDonald, S. Rosenzweig, J. S. Guerin, R. W. McCalden, E. R. Bohm, R. B. Bourne*, et al.*, "Proximally Versus Fully Porous-coated Femoral Stems: A Multicenter Randomized Trial," *Clinical Orthopaedics and Related Research,* vol. 468, pp. 424-432, 09/24 2010.

[135] M. A. Sutton, J. J. Orteu, and H. Schreier, *Image correlation for shape, motion and deformation measurements: basic concepts, theory and applications*: Springer Science & Business Media, 2009.

[136] H. M. Kjer and J. Wilm, "Evaluation of surface registration algorithms for PET motion correction," DTU Informatics, Technical University of Denmark, 2010.

[137] S. Gilchrist, P. Guy, and P. A. Cripton, "Development of an Inertia-Driven Model of Sideways Fall for Detailed Study of Femur Fracture Mechanics," *Journal of Biomechanical Engineering,* vol. 135, pp. 121001-121001, 2013.

[138] L. Grassi and H. Isaksson, "Extracting accurate strain measurements in bone mechanics: A critical review of current methods," *Journal of the Mechanical Behavior of Biomedical Materials,* vol. 50, pp. 43-54, 10// 2015.

[139] I. Oh and W. H. Harris, "Proximal strain distribution in the loaded femur. An in vitro comparison of the distributions in the intact femur and after insertion of different hip-replacement femoral components," *The Journal of Bone & Joint Surgery,* vol. 60, pp. 75-85, 1978.

[140] P. Østbyhaug, J. Klaksvik, P. Romundstad, and A. Aamodt, "An in vitro study of the strain distribution in human femora with anatomical and customised femoral stems," *Journal of Bone & Joint Surgery, British Volume,* vol. 91, pp. 676-682, 2009.

[141] E. Tayton, S. Evans, and D. O’doherty, "Mapping the strain distribution on the proximal femur with titanium and flexible-stemmed implants using digital image correlation," *Journal of Bone & Joint Surgery, British Volume,* vol. 92, pp. 1176-1181, 2010.

[142] H. Johansen-Berg, H. Dawes, C. Guy, S. M. Smith, D. T. Wade, and P. M. Matthews, "Correlation between motor improvements and altered fMRI activity after rehabilitative therapy," *Brain,* vol. 125, pp. 2731-2742, 2002.

[143] L. M. White and K. A. Buckwalter, "Technical considerations: CT and MR imaging in the postoperative orthopedic patient," in *Seminars in musculoskeletal radiology*, 2002, pp. 5-17.

[144] S. Leuders, M. Thöne, A. Riemer, T. Niendorf, T. Tröster, H. A. Richard*, et al.*, "On the mechanical behaviour of titanium alloy TiAl6V4 manufactured by selective laser melting: Fatigue resistance and crack growth performance," *International Journal of Fatigue,* vol. 48, pp. 300-307, 3// 2013.

[145] L. A. Hoff, B. Johnston, M. M. Rahman, S. Khanoki, D. Pasini, and R. Wutrich, "Electro-Polishing of Additive Manufactured Porous Titanium for Medical Implants," in *Electrochemical Society*, Chicago, 2015.

[146] A. Aamodt, J. Lund-Larsen, J. Eine, E. Andersen, P. Benum, and O. S. Husby, "Changes in proximal femoral strain after insertion of uncemented standard and customised femoral stems AN EXPERIMENTAL STUDY IN HUMAN FEMORA," *Journal of Bone & Joint Surgery, British Volume,* vol. 83, pp. 921-929, 2001.

[147] P. O. Østbyhaug, J. Klaksvik, P. Romundstad, and A. Aamodt, "Primary stability of custom and anatomical uncemented femoral stems: A method for three-dimensional in vitro measurement of implant stability," *Clinical Biomechanics,* vol. 25, pp. 318-324, 2010.

[148] J. Grant, N. Bishop, N. Götzen, C. Sprecher, M. Honl, and M. Morlock, "Artificial composite bone as a model of human trabecular bone: the implant–bone interface," *Journal of biomechanics,* vol. 40, pp. 1158-1164, 2007.

[149] ISO, "7206-4:2010 Part 4: Determination of endurance properties and performance of stemmed femoral components," in *Implants for surgery -- Partial and total hip joint prostheses* --, ed, 2010.

[150] ISO, "7206-6:2013 Part 6: Endurance properties testing and performance requirements of neck region of stemmed femoral components," ed, 2013.

[151] E. Masoumi Khalil Abad, S. Arabnejad Khanoki, and D. Pasini, "Fatigue design of lattice materials via computational mechanics: Application to lattices with smooth transitions in cell geometry," *International Journal of Fatigue,* vol. 47, pp. 126-136, 2013.